Universidade de Aveiro
2013

Departamento de Engenharia de Materiais e Cerâmica

Marco Sílvio Assamo Medeiros

Síntese e caracterização de cerâmicos magnetoelétricos/multiferróicos

Synthesis and characterization of Magnetoelectric/Multiferroic Ceramics

Universidade de Aveiro
2013

Departamento de Engenharia de Materiais e Cerâmica

Marco Sílvio Assamo Medeiros

Síntese e caracterização de cerâmicos magnetoelétricos/multiferróicos

Synthesis and characterization of Magnetoelectric/Multiferroic Ceramics

Dissertação apresentada à Universidade de Aveiro para cumprimento dos requisitos necessários à obtenção do grau de Mestre em Engenharia de Materiais – 2 ciclo, realizada sob a orientação científica do Doutor Andrei Kholkine, Equiparado a Investigador Coordenador do Laboratório Associado CICECO e Departamento de Engenharia de Materiais e Cerâmica da Universidade de Aveiro, e do Doutor Robert Pullar, Equiparado a Investigador Auxiliar do Departamento de Engenharia de Materiais e Cerâmica da Universidade de Aveiro.

Dedico este trabalho a minha família e aos amigos por todo o seu apoio.

o júri

presidente

Professor Doutor Joaquim Manual Vieira
Professor Catedrático do Departamento de Engenharia de Materiais e Cerâmica da Universidade de Aveiro

Professor Doutor Vítor Brás de Sequeira Amaral
Professor Catedrático do Departamento de Física da Universidade de Aveiro

Doutor Andrei Kholkine
Equiparado a Investigador Coordenador do Laboratório Associado CICECO e do Departamento de Engenharia Materiais e Cerâmica da Universidade de Aveiro

Doutor Robert Pullar
Equiparado a Investigador Auxiliar do Departamento de Engenharia de Materiais e Cerâmica da Universidade de Aveiro.

agradecimentos

Primeiramente, gostaria de agradecer ao meu orientador Doutor Andrei Kholkine pela orientação e coordenação da dissertação e pela sua disponibilidade; ao Doutor Robert Pullar um especial agradecimento pela co-orientação da tese, pela motivação e ensinamentos e também pela disponibilidade patenteada. Queria agradecer ao Doutor João Amaral, professor do departamento de Física da Universidade de Aveiro, pela disponibilidade e colaboração em realizar as medições no VSM; à Doutora Indrani Coondoo na preparação do KNN e pelas dicas fundamentais no trabalho prático, ao Doutor Dmitry Karpinsky agradeço a disponibilidade para a realização das medições da microscópia de força piezoelétrica e magnética e pelos conhecimentos transmitidos; aos meus colegas de laboratório, Aliaksandr Shaula, David e Vladislav agradeço o apoio moral e utilização de alguns dos seus equipamentos; aos auxiliares do departamento de Materiais e Cerâmica, Eng. Célia, Maria João Bastos, Ana Ribeiro, Jacinto Alves, Octávio Contente, a ajuda em manusear todos os equipamentos necessários à realização deste trabalho e pela motivação dada. Por fim agradeço aos meus familiares e colegas pelo apoio dado durante o percurso académico.

palavras-chave

Compósitos magnetoelectricos, multiferróicos, ferrites hexagonais, $BaFe_{12}O_{19}$, $SrFe_{12}O_{19}$, $Ba_3Co_2Fe_{24}O_{41}$, $Sr_3Co_2Fe_{24}O_{41}$, KNN, $BaTiO_3$.

resumo

Materiais magnetoelétricos e multiferróicos que exibem simultaneamente propriedades ferroelétricas e ferromagnéticas, têm suscitado um crescente interesse na comunidade científica para o desenvolvimento de materiais multifuncionais. Neste trabalho pretendeu-se fabricar materiais cerâmicos multiferroicos e realizar um estudo do acoplamento entre propriedades magnéticas e as propriedades piezoelétricas/ferroelétricas dos compósitos.

Assim, foram realizados estudos sobre a síntese das hexaferrites ($BaFe_{12}O_{19}$, $SrFe_{12}O_{19}$, $Ba_3Co_2Fe_{24}O_{41}$ e $Sr_3Co_2Fe_{24}O_{41}$), com diferentes temperaturas de reacção e diferentes métodos de preparação: reação de estado sólido, co-precipitação, sol-gel e combustão de citratos. De seguida, foram preparados compósitos de hexaferrites e piezoelétricos, nomeadamente $BaTiO_3$ e $K_{0.5}Na_{0.5}NbO_3$ (KNN), foram realizadas as prensagens: uniaxial e isostática a frio. A densidade relativa obtida após a sinterização foi 85% da densidade teórica nos compósitos com $BaTiO_3$ e 81% nos compósitos com KNN.

Foram efetuadas medições magnéticas, nomeadamente por microscópia de força magnética e magnetometria por vibração de amostra, e medições piezoelétricas, por microscópia de força piezoelétrica. Em alguns compósitos foi detetada a inter-difusão de átomos do bário e estrôncio produzindo várias fases secundárias diminuindo o efeito piezoelétrico. As medições magnéticas mostraram que os compósitos com ferrites duras ($BaFe_{12}O_{19}$ e $SrFe_{12}O_{19}$) formaram um ciclo de histerese com maior área do que os compósitos com ferrites macias ($Ba_3Co_2Fe_{24}O_{41}$ e $Sr_3Co_2Fe_{24}O_{41}$). Alguns compósitos demonstram acoplamento magnetoelétrico significativo.

keywords Magnetoelectric composites, multiferroics, hexagonal ferrites, $BaFe_{12}O_{19}$, $SrFe_{12}O_{19}$, $Ba_3Co_2Fe_{24}O_{41}$, $Sr_3Co_2Fe_{24}O_{41}$, KNN, $BaTiO_3$.

summary Magnetoelectric and multiferroic materials that exhibit both ferroelectric and ferromagnetic properties, have raised great interest in the scientific community for the development of multifunctional materials. In this work we intended to fabricate multiferroic ceramics and to study the coupling between magnetic properties and piezoeletric/ferroelectric properties of composite materials. Synthesis of hexaferrites ($BaFe_{12}O_{19}$, $SrFe_{12}O_{19}$, $Ba_3Co_2Fe_{24}O_{41}$ and $Sr_3Co_2Fe_{24}O_{41}$), was undertaken with different reacting temperatures and different preparation methods: solid state reaction, coprecipitation, sol-gel and citrate. Also we performed analysis by XRD and determined the phases of each material. We prepared composites of hexaferrites and piezoelectric phases (BaTiO3, KNN) with uniaxial pressing and cold isotactic pressing. $BaTiO_3$ composites have shown a relative density of 85% compared with the theoretical density and the KNN composites had a maximum density of 81%.

We performed magnetic (MFM and VSM), and piezoelectric (PFM) measurements, and it was verified that in some composites we observed diffusion of atoms between barium and strontium sources producing new phases lowering the piezoelectric effect. In the magnetic analysis it also was verified that the hard ferrites formed hysteresis loops with greater area than the soft ferrites. It was found that some composites demonstrate capable magnetoelectric coupling.

Index

List of Symbols

TMR – Tunnelling magnetoresistance

GHz – Giga Hertz Frequency

ME – Magnetoelectric effect

BT, $BaTiO_3$ – Barium titanate

KNN – Sodium potassium niobate

α-Fe_2O_3 - Hematite

δ – Inversion parameter of spinel

FCC – Face Centered-Cubic

Me – Divalent cation

H – Magnetic field strength / force

M – Magnetisation

B – Magnetic induction / Flux Density

μ_0 – Magnetic permeability in vacuum

σ - Magnetic moment per unit mass

MCA – Magnetocrystalline anisotropy

MLCs – Multilayer capacitors

PZT – Lead zirconate titanate

MW – Microwave

mT - Militesla

M_s – Saturation magnetisation

M_r – Remanet magnetisation

H_c – Coercive force, coercivity

PFM – Piezoresponse force microscopy

MFM – Magnetic force microscopy

VSM – Vibrating sample magnetometer

List of figures

List of Tables

1. Introduction

The development of new types of materials has been the key for the innovation of technology in the present day, such the development of required materials with high multifunctionality and low dimensions. The multiferroic magnetoelectric ceramics are considered by many researchers to be a good choice to produce a new kind of devices. They exhibit ferroelectric and magnetic properties, and some coupling between magnetic and dielectric/ferroelectric phases, the magnetoelectric effect (ME), where an induced electrical polarization and magnetization can be controlled by applying a magnetic and electric field, respectively. This would allow some kind of tuneability, switching or sensing to be achieved in these composites. This effect can potentially be exploited to allow the construction of novel spintronic devices such as tunnelling magnetoresistance (TMR), sensors, spin valves with functionality that is tuneable by an electric field [1] or responsive smart materials, especially at microwave (GHz) frequencies and multi-state memories in which data are written electrically and read magnetically [2]. However, in order to be useful for applications, the magnetoelectric coupling must be both large and active at room temperature.

There are several magnetoelectric materials, some of them are composites and others are single phase. The use of single phase materials is rare, and most of them have not been successful applied mainly due to one import reason, they have low Neel or Curie temperature (T_c), much lower than room temperature, and those materials exhibit ME effect at those temperatures only.

The intrinsic structural/electronic conditions which give rise to ferroelectricity are not conducive to ferromagnetism, and vice-versa, making the magnetoelectric coefficient decrease to zero as the temperature reaches the transition temperature, and at this temperature the single phase magnetoelectric materials shows low ME effect.

An alternative approach is to make a composite material, consisting of two complimentary magnetic and ferroelectric phases, which can have coupling between them, often strain-mediated in nature (i.e., piezoelectric/magnetostrictive coupling).

The experimental work was divided in two parts, the first was to produce hexaferrites by different synthesis methods, the second part was to prepare perovskite materials and to combine different materials to make composites.

In this first part we produced M and Z ferrites with hexagonal structure using wet chemical techniques such as: sol-gel, co-precipitation, citrate and solid state reaction. These methods were

also investigated as they allow a more intimate degree of mixing of the reactants this can result in nanosized precursors and materials.

In the second part two different approaches were involved:

1. Synthesis and mixing of the dielectric/ferroelectric ceramic to produce a magnetic ferrite ceramic ME composites. The magnetic ceramic was a hexagonal ferrite, while the dielectric ceramics were two perovskites: barium titanate (BT, $BaTiO_3$) and sodium potassium niobate ($K_{0.5}Na_{0.5}NbO_3$, KNN), both of which operate at microwave (GHz) frequencies. In his works Pullar et al.[2] already demonstrated that ceramic composites of $BaFe_{12}O_{19}$ (BaM, M-ferrite) and barium titanate co-sinter without reacting, to form a ceramic composite, and it was demonstrated that they maintain their magnetic and ferroelectric properties [1, 2]. We intended to investigate the effects of varying composition of the composite components, the optimisation of their density and properties through processing.

2. Although single phase MF ceramics are rare, some hexaferrites have been reported to be such materials. Of particular interest is strontium Z ferrite (SrZ, $Sr_3Co_2Fe_{24}O_{41}$). This ferrite was first reported and characterised magnetically by Dr Pullar [3], but recently it was found by other investigators to be a room temperature Multiferroic. However, the stability range and solid state chemistry of this ceramic are still poorly understood, and it is likely that other similar hexaferrites could have similar properties. In this work the synthesis of this ferrite and related compounds was studied in this work, to better understand the relationship between composition, structure, processing and MF and magnetic properties. Also ME composites of this ferrite with dielectric ceramics were investigated.

The second part of the project consisted of intensive characterization by vibrating sample magnetometry, and nanoscale characterization by AFM/PFM/MFM, to show the co-existance/coupling of ME phases.

1.1.State of Art – Magnetoelectric / multiferroic materials

Magnetoelectric coupling was first discovered at end of 19th century. It was demonstrated that the magnetisation of a dielectric material can change in the presence of electrical field and vice versa. The polarization of a dielectric under influence of a magnetic field was first postulated by Röntgen [4], and in 1894 Pierre Curie pointed out that it would be possible for an asymmetric molecular body to polarize directionally under the influence of a magnetic field [5].

The term "magnetoelectric" was attributed by Dybe [6] after the first unsuccessful attempt to demonstrate the static ME effect experimentally [7]. In 1948 Tellegen formulated the idea to fabricate a composite displaying ME effects [8], Tellegen suggested a suspension of microscopic particles that carry both electric and magnetic dipole moments, an idea, that, however, has not been realized. However, it was only in 1959 that Dzyaloshinskii predicted the ME effect in Cr_2O_3 based on symmetry considerations, and in 1960 Astrov confirmed this prediction experimentally by measuring electric field induced magnetisation [9-11].

The first attempt to combine two different proprieties, ferromagnetic and ferroelectric in the same system was in the 1960's by two groups in Soviet Union, the group of Smolenskii [12] and by Venevtsev [13]. Novel materials were developed with very promising applications in diverse fields and the name of multiferroic was coined this kind of material [14].

In composite materials, the ME effect was comprehended when Van Suchetelene introduced the concept of ''product properties'' in 1972. He used it to grow successfully the first magnetoelectric composite by unidirectional solidification of a $BaTiO_3$–$CoFe_2O_4$ eutectic liquid [15], but was just in 1978 Van den Boomgaard and Born [16] postulated that: (i) two individual phases should be in equilibrium, (ii) mismatching between grains should not be present, (iii) magnitude of the magnetostriction coefficient of piezomagnetic or magnetostrictive phase and magnitude of the piezoelectric coefficient of the piezoelectric phase must be greater, (iv) accumulated charge must not leak through the piezomagnetic or magnetostrictive phase and (v) a deterministic strategy for poling of the composites.

In the early 1990's, Newnham's group and Russian scientists prepared ceramic composites by conventional sintering method of ferrites, $BaTiO_3$ and $Pb(ZrTi)O_3$ (PZT) [17]. This method helped reduce the cost of production of sintered ceramic composites in comparison to eutectic composites. Some studies were made to predicted resultant ME tensor responses in bulk ceramic materials, and some micromechanical approaches were adopted such as Green's function approach to solve coupled magnetoelectricelastic problems [18]. The multiferroic ME composites didn't have

too much research development in this decade, but in the beginning of 2000 these materials started to gain importance and several investigations were made. In particular, ceramic composites with different connectivity

An upsurge in the multiferroic ME composite research appeared in the early 2000s. Some ceramic composites with different connectivity schemes were reported the 0–3–type and 2-2– type laminate composites [17]. These were the first types of connectivity studied in composite materials, and at present there are 10 different connectivity types, the easiest composite to synthesis is the particulate composite due the advances in those techniques [19].

A revolutionary breakthrough on the ME bulk composites was made in 2001, a ferroic composite with giant magnetostrictive a rare-earth-iron alloy, $Tb_{1-x}Dy_xFe_2$ (Terfenol-D) and a ferroelectric polymer such as the poly(vinylidene fluoride)-trifluorethylene copolymer [P(VDF-TrFE)], in which they are respectively, the best known and most widely used magnetostrictive alloy and ferroelectric polymer. Those materials are mechanically flexible and much easy to fabricate than the brittle ferroelectric/piezoelectric ceramic composites [20, 21]. In 2003 Dong et al., reported various types of laminate composites of Terfenol-D and piezoelectric ceramics with giant ME response (GME), and such materials have a ME coefficient superior to 1 V/cm [22-24].

More recently, in order to overcome brittleness and high eddy current loss of the Terfenol-D/piezoceramic composites, three-phase ME bulk composites of Terfenol-D/piezoceramics/polymer have been made, including composites with different connectivity schemes (quasi-0-3, 1-3, and 2-2). A maximum ME coefficient of 0.1 V/cm was reported in these three-phase composites. Also nanostructured composite thin films of magnetic and ferroelectric oxides have been developed.

In 2004 Zheng et al. reported the first experimental nanostructured films with connectivity schemes 1-3 and 2-2 [25]. Until the present day the research in the multiferroic nanostructured films of ferroelectric and magnetic oxides have been developed, such as multiferroic nanostructures, and are a hot topic in the multiferroic composites field with very promising potential applications in microelectronic devices [26-28].

1.2.Motivation

The composite materials study in this area is of great interest for the development of new kinds of multiferroic magnetoelectric devices, and these materials were produced with different ways of synthesis and sintering.

To make the composites, materials that were chosen were the M ferrites (BaM, $BaFe_{12}O_{19}$, and SrM, $SrFe_{12}O_{19}$) and Z ferrites (BaZ, $Ba_3Co_2Fe_{24}O_{41}$, and SrZ, $Sr_3Co_2Fe_{24}O_{41}$), due to the necessity of producing new composite materials with low cost and minimising the sintering time and/or temperature.

Some aspects while synthesising composite materials should be taken in mind such as the connectivity between the multiferroic and the piezoelectric material, individual properties of the components and the so-called sum property. The proprieties of the individuals components are important, as is the sintering of the compounds to achieve better proprieties of the composites.

In this work we used M ferrites (barium and strontium) that are widely used as permanent magnets and the Z ferrites (also barium and strontium) that are known to work at GHz frequencies in communications devices. The piezoelectric materials used to make the composites were $BaTiO_3$ and KNN ($K_{0.5}Na_{0.5}NbO_3$). Both materials are lead-free piezoelectric materials, $BaTiO_3$ is a very attractive material because of high dielectric constant and low loss characteristics. It is known to be chemically compatible with the hexaferrites, so is a good candidate to be used as a composite. KNN has the maximum piezoelectric properties known similar to $BaTiO_3$ but has higher T_c. It's a very promising candidate for making composites for the development of new applications.

This work was attractive for research purposes, because different chemical wet techniques and different measurements techniques were used, to produce and study ferroelectric and magnetic phases in the composites, creating also an opportunity to operate different equipment, and also was a good opportunity to work in the scientific environment.

1.3.Literature Review

1.3.1. Multiferroics and magnetoelectric materials

Multifunctional or smart materials combining several properties in the same structure in order to produce new or enhanced phenomena have stimulated much scientific and technological

interest within the scientific community in the last years, among them, the multiferroics, combining at least two ferroic orders: ferroelectric, ferromagnetic, or ferroelastic in the same temperature range. These materials can be single-phase, which are rare but do exist, or composites [29]. The ferroic systems possess a parameter order that is switchable by an adequate driving force or field, phenomena normally accompanied by hysteresis.

In the multiferroic materials, the coupling interaction between the different order parameters could produce new effects, such as magnetoelectric ME effect, that is, magnetic field affects the electrical polarization, and an electrical fields affects the magnetisation, producing a coupling between magnetic and electrical proprieties on magnetoelectric materials [30]. These effects can also been seen in non-ferroic proprieties such as permeability, permittivity or resonant frequencies, and be done by direct stimulus due to an applied field, or an indirect stimulus through the application of voltage or stress.

The multiferroic and magnetoelectric materials are related to each other as shown in figure 1. Ferromagnets (ferroelectrics) form a subset of magnetically (electrically) polarizable materials such as paramagnets and antiferromagnets (paraelectrics and antiferroelectrics). The intersection (red hatching) represents materials that are multiferroic. Magnetoelectric coupling (blue hatching) is an independent phenomenon that can, but need not, arise in any of the materials that are both magnetically and electrically polarizable. In practice, it is likely to arise in all such materials, either directly or via strain [31].

ME and MF properties many times overlap, but not all ME materials are necessarily MF [32].

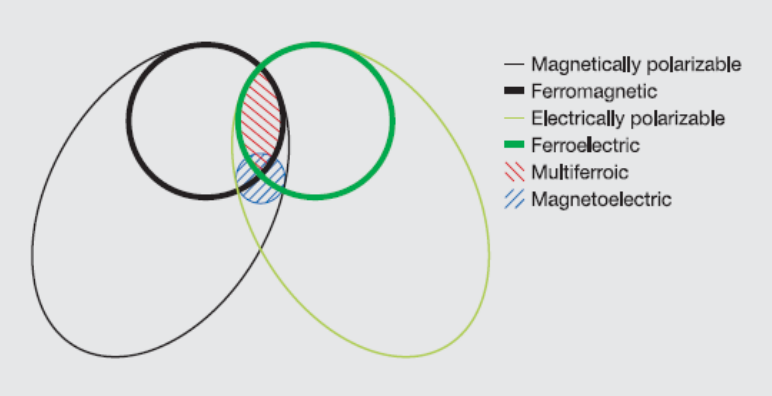

Figure 1: The relationship between multiferroic and magnetoelectric materials [31].

1.3.2. Composite ME materials

As an alternative to overcoming the problems of the single-phase magnetoelectric materials and with greater design flexibility, multiferroic ME composites made by combining piezoelectric and magnetic materials together have become much more attractive and gained significant interest in the last few years due to their multifunctionality, because the coupling interaction between piezoelectric and magnetic materials can produce a large magnetoelectric response [33]. This response is potentially several orders of magnitude higher than that in current single-phase magnetoelectric materials at room temperature.

A new class of multifunctional devices could be built from ME composites such as magneticelectric transducers, actuators and sensors. The ME effect in composite materials is known as a product tensor property resulting from the cross interaction between different orderings of the phases in the composite. The individual phases don't have ME effects, but in composites the two phases (piezoelectric and magnetic) can have a remarkable ME effect [17].

1.3.3. Proprieties of ME Composites

ME composites can exhibit magnetoelectric effects over a wide temperature range [34],. This effect can be archived by different paths, using the resulting propriety of the piezoelectric and magnetostrictive effects [35, 36], or using the product propriety of the pyroelectric and magnetostrictive effects [19]. The composite materials properties of magnetostrictive and piezoelectric materials can be explained by the following mechanism: when a magnetic field is applied to the composite the magnetostrictive material is mediated strained, and this will induce a stress on the piezoelectric component and generate electric field. The inverse of this effect is possible - applying an electrical field to the piezoelectric material will produce strain, which will be transferred as stress to the magnetostrictive material. These causes will produce a change in magnetic permeability of the material. In both cases the product property resulting in such composites is described as the magnetoelectric effect (ME), in which a magnetic applied field induces a change in electric polarisation, and an applied electric field induces changes in magnetic permeability in the composite. Therefor the ME effect is the result of the product of the magnetostrictive effect (magnetic/mechanical) in the magnetic phase and piezoelectric effect (mechanical/electrical) in piezoelectric phase. This effect is quantified in two ways:

$$ME\ effect = \frac{electrical}{mechanical} * \frac{mechanical}{magnetic} \ units\ of\ \alpha = s\,m^{-1}$$

$$ME_{II}\ effect = \frac{magnetic}{mechanical} * \frac{mechanical}{electrical} \ units\ of\ \alpha_{II} = s\,m^{-1}$$

The ME effect is when an electric field is applied, and ME_{II} is when a magnetic field is applied [3].

1.3.4. Magnetoelectric coupling

There are various ways in which the components can connected in a ME material such as the bulk ceramic ME composites of piezoelectric ceramics and ferrites [17, 30], two-phase ME composites of magnetic alloys and piezoelectric materials, three phase ME composites, and thin films of ferroelectric and magnetic oxides.

In 1978 Newnham *et al*. introduced the concept of phase connectivity [19]. With this concept is possible to describe the structure of two phase composites, where each phase in a composite may be self-connected by different dimensions zero, one, two and three dimensions.

In the case of two-phase composites, there are ten different connectivities: 0-0 (zero connectivity between either of the phases present), through to 3-3 (both phases interpenetrating in all three dimensions). The different changes in connectivity between phases can result in substantially different proprieties, and figure 2 illustrates the different connectivities. Most of the attention in this work goes to 3-3 type bulk ceramic phase connectivity.

The 3-3 phase connectivity is the most complicated to obtain and the most interesting one, the two phases of the composite form interpenetrating three-dimensional networks. One way to achieve tailorable 3–3 composites is infiltration of a second phase into porous materials that display complete pore connectivity and percolation. Provided the structure of the initial porous material can be precisely controlled in terms of the degree of porosity, the size and shape of the pores, and the nature of the struts separating them, then there is the opportunity to design and fabricate interpenetrating composites with customized structures. Hence, the infiltration of cellular ceramics offers the potential for producing tailored ceramic-based interpenetrating composites with 3–3 interconnectivity. Patterns of this phase connectivity occur in some living systems such as corals where organic tissue and an inorganic skeleton interpenetrate one into another.

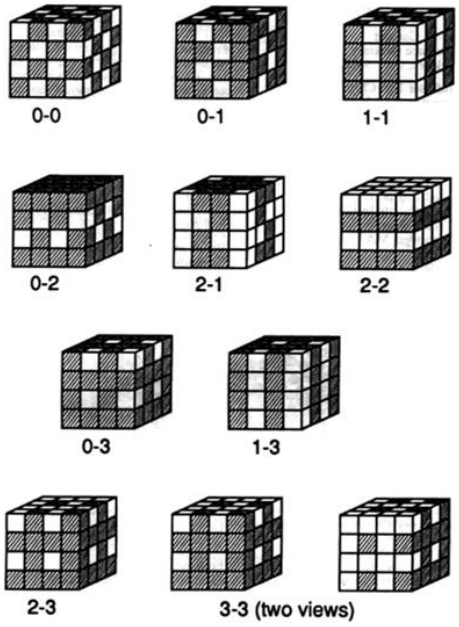

Figure 2: The ten different levels of connectivity that can exist in composites, as defined by Newnham [37]

Since the commercial introduction of soft ferrites by Philips in 1948, they have become one of the materials most used in electronic devices as inductor or transformer cores, because of their high resistivity in comparison to metallic soft-magnetic materials. This makes the ferrites to be considered better suited for frequencies of 10 kHz and above [38].

1.4.Ferrites

Usually the ferrites are primarily classified into three types: garnets, spinels and hexagonal ferrites, according to their primary crystal lattice. Generally, ferrimagnetism arises from the antiparallel alignment of the magnetic moments on transition metal ions, present on different magnetic sublattices. The origin of the antiparallel coupling can be explained by the super-exchange of valence electrons between the filled p-orbitals of O^{2-} and unfilled d-orbitals of the transition metal cations. In ferrites, the oppositely directed magnetic moments do not exactly cancel, thus a net magnetic moment results [39, 40]. This is known as ferrimagnetism.

1.4.1. Invert Spinel

Spinels have the general formula $MeO{\cdot}Fe_2O_3$, where *Me* usually represents a divalent ion or a combination of ions with an average valence of two such as manganese (Mn^{2+}), nickel (Ni^{2+}), cobalt

(Co^{2+}), zinc (Zn^{2+}), copper (Cu^{2+}), or magnesium (Mg^{2+}) [39]. In some cases *Me* can also represent the monovalent lithium cation (Li^{+}) or even vacancies, as long as these absences of positive charge are compensated for by additional trivalent iron cations (Fe^{3+}). The ionic distribution in this kind of structure may be represented by $[Me_{\delta}Fe_{1-\delta}]^{A}[Me_{1-\delta}Fe_{1+\delta}]^{B}O_4$, where δ is the inversion parameter and δ = 0 and 1 stand for the inverse and normal cases respectively. The spinel ferrite crystallizes in the cubic structure but there are some exceptions like $CuFe_2O_4$ that can have tetragonal structure if cooled slowly from high temperatures, causing massive interaction exchange between the cations occupied in different interstitial sites through oxygen anions [41].

The spinel lattice is composed of a close-packed oxygen anions arrangement in which 32 oxygen ions form the unit cell (the smallest repeating unit in the crystal network). These anions are packed in a centred cubic face (FCC) arrangement leaving two kinds of spaces between anions: tetrahedrally coordinated sites (A), surrounded by four nearest oxygen atoms, and octahedrally coordinated sites (B), surrounded by six nearest neighbour oxygen atoms, figure 3. There are a total 64 tetrahedral sites and 32 octahedral sites in the unit cell, of which only 8 tetrahedral sites and 16 octahedral sites are occupied, resulting in a structure that is electrically neutral [42].

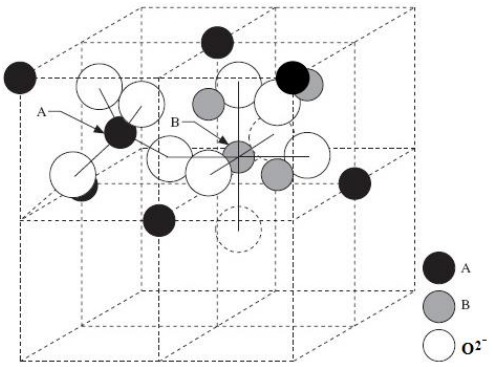

Figure 3: Two octants of the spinel unit cell. A and B represent tetrahedrally and octahedrally coordinated sites respectively [43].

1.4.2. Hexaferrites

There are a group of ferrites with hexagonal structure, and they have an important role in the field of the electronic industry due to their magneto-electrical proprieties that produce extensive applications in magneto-optical, microwave and GHz devices [44, 45]. The high electrical resistivity and low magnetic losses of hexaferrites minimize the insertion loss in microwave devices and allow their applications in circulators, filters, isolators, inductors and phase shifters.

The hexagonal ferrites are all ferrimagnetic materials, and their magnetic properties are intrinsically linked to their crystalline structures. The hexaferrites have directional preference of magnetisation called magnetic anisotropy. There are several types of anisotropy possible, namely shape anisotropy, stress anisotropy, and magnetocrystalline anisotropy [32].

The hexaferrites have a major axis called the 'c' axis, it is perpendicular to the hexagonal plane in which can rotate 180 ° this is reason why Z-ferrites are soft, at room temperature they have magnetisation in plane. Also the hexaferrites have a minor axis called the 'a' axis located in the hexagonal plane, in the M ferrites the c axis is the preferred direction within the axis of crystal structure, making them magnetically hard, used to good advantage as a permanent magnet material. In the hexaferrites the oxygen ions are as closely packed as they are in the spinel structure, with the exception that the oxygen layers include Ba^{2+}, Sr^{2+} or Pb^{2+} ions, which have similar ionic radii to the oxygen ions, and so can replace those in the lattice.

The hexaferrites are classified in 6 types depending on their chemical and crystalline structure: M, W, Y, X, U and Z, and the related cubic S (spinel) structure, given in table 1 [41].

The M phase is made of a combination of the S (two spinels, Fe_6O_8) and R ($BaFe_6O_{11}$) blocks, and the Y phase is made of a combination of the S and T ($Ba_2Fe_8O_{14}$) blocks. To produce W and Z hexaferrites, the phases M, Y and S are used with the following combinations of blocks: W=M +S (= R + S + S), and Z=M+Y (= R + S + T + S). This demonstrates the similarity of the structures that all the hexaferrites have.

Table 1: Hexaferrites types with their chemical formula, composition and stacking order [41].

Hexaferrite Type	Composition	Stacking order*
S-Spinel	2 MeO·2 Fe_2O_3	S
M	BaO·6 Fe_2O_3	RSR*S*
Y	2 BaO·2 MeO·6 Fe_2O_3	STSTST
W	BaO·2 MeO·8 Fe_2O_3	RSSR*S*S*
Z	3 BaO·2 MeO·12 Fe_2O_3	RSTSR*S*T*S*
X	2 BaO·2 MeO·14 Fe_2O_3	RSR*S*S*
U	4 BaO·2 MeO·18 Fe_2O_3	RSR*S*T*S*

Notes: Sub-units for stacking order, using, S = Fe_6O_8 (spinel), R = $BaFe_6O_{11}$ (hexagonal), and T = $Ba_2Fe_8O_{14}$ (hexagonal). The asterix (*) indicates that the corresponding sub-unit is rotated 180° around the hexagonal axis.

1.4.3. History of hexagonal ferrites

The magnetic mineral magnetoplumbite was first characterised in 1925 [46], but only in 1938 was it possible to deduce the crystal structural as hexagonal with the composition $PbFe_{7.5}Mn_{3.5}Al_{0.5}Ti_{0.5}O_{19}$ [47]. The synthetic form of magnetoplumbite was found to be $PbFe_{12}O_{19}$, or pure PbM, and a number of isomorphous compounds were suggested including $BaFe_{12}O_{19}$. However, it was only after the Second World War that this material was structurally investigated by Philips Laboratories, and then under the direction of Snoek in the 1950's the development of the hexaferrites started. Went et al. studied and report to the scientific community that BaM has a hexagonal structure [48].

After this, hard magnets such as $BaFe_{12}O_{19}$ and $SrFe_{12}O_{19}$ experienced considerable development, and some studies made by then showed that Sr ferrite was slightly superior in magnetic proprieties [49].

Further investigations by Wijn and Braun of $BaO–Fe_2O_3$ systems contributed to produce more complex hexagonal compounds with the presence of divalent and trivalent iron species ($BaFe_{18}O_{27}$) [50, 51], and also investigations by Jonker, Wijn and Braun lead to the discovery of new compounds with ternary systems $BaO–Fe_2O_3–MeO$, where Me is a small divalent cation, resulting in the Y and Z ferrites, and further to W, U and X.

1.4.4. M ferrites

The most common M ferrites are BaM and SrM both of them are used on a very large scale as permanent magnets [52] .

The compound BaM, was known to exist for many years, with a melting point of 1390°C confirmed in 1936 by *Arkel et al.* [53], but only in 1950s was confirmed that the structure was isomorphous with hexagonal magnetoplumbite, and it was first called ferroxdure to distinguish it from the spinel ferrite.

BaM is hard magnet with coercivity of 503.9 mT, saturated magnetisation 58.4 emu/g and high electrical resistivity of $10^8\Omega$ cm. In comparison with some magnetic alloys, BaM has a lower saturation magnetisation and has high magnetic uniaxial anisotropy along the c-axis [54].

The molecular mass of BaM is 1112g and the theoretical density is 5.295 g cm^{-3} [55] (some authors refer to this as maximum density), although the material often has lower density 90% of

the theoretical density. The hardness of BaM in the c-axis has been calculated to be 5.9 GPa [30], and measured as 6.0 Gpa [56].

Barium atoms can be replaced with others atoms according with substitutional solid solution rules:

- Host and dopant sizes should not exceed about 15%;
- Isovalent ions are preferred;
- Solid solution is unlikely if both species are likely to react and form new compounds;
- Host and dopant with identical structures are preferred.

Therefor the barium is normally replaced with strontium atom, producing the SrM compound that has less density and molecular mass, respectively: 5.101 g cm^{-3} and 1062g [55]. SrM resembles BaM in most other physical properties [57].

The strontium hexaferrite was first prepared by AdelskÖld in 1938 [58]. SrM powder can exhibit a high coercivity (552.9 mT) and saturated magnetisation of 65 emu/g [59], due to the relatively high magnetocrystalline anisotropy field, making it an attractive material for use in permanent magnet applications [60].

1.4.5. Z Ferrites

Hexagonal Ferrites with Z-type structures are soft magnetic materials, discovered in 1950's at the same time as the ferroxplana Y-type ferrites [30]. The mostly common Z-type ferrites are the BaZ and SrZ, and many of them have planar anisotropy parallel to the c-axis. Co_2Z is planar at room temperature, but has a complex magnetic anisotropy, with at least four different anisotropic states.

The Z-type ferrites (Me_2Z) are formed by the sum of M and Y (figure 5) compounds in stacks, and often have anisotropy at an angle to the c-axis, in particular, Co_2Z ferrites such as $Ba_3Co_2Fe_{24}O_{41}$, which is a member of the planar hexaferrite family called *ferroxplana*, in which the easy magnetisation direction lies in the basal plane (a-axis or *c*-plane) of the hexagonal structure at room temperature.

SrZ ferrite is one of the only hexaferrites that exhibits a low-field ME effect at room temperature and is a single phase ferrite, the substitution of Ba^{2+} for Sr^{2+} reduce the sintering temperature from 1250 °C to 1200 °C, improving of the frequency characteristic of the permeability, and reducing the cost in manufacturing. SrZ ferrite has molecular mass of 2376.99 g/mol and it shows an H_c of 6.72 mT and a density of 5.12 g cm^{-3}. On the other hand, BaZ ferrite has a higher molecular mass than SrZ, 2552 g, and superior density, 5.35 g cm^{-3}, and it shows different values

of H_c depending of the sintering temperature and the *Ms* typically it is between 48.62 emu/g [30], much lower than M ferrites.

1.5.Magnetism in ferrite materials

The magnetic materials play a very important role in the history of civilization, all the substances: solid, liquid or gaseous, shows some magnetic proprieties almost at all temperatures, making magnetism a basic property of any material [61].

Magnetism is a property that materials have in response to an applied magnetic field. Its origin is related to electrons and their motion and spin, so the magnetic proprieties have their origins in the electronic structure of the atoms. From a classic point of view there are two movements associated with the electrons that could explain the origin of magnetic moments: the orbital angular motion around the nucleus and the electrons intrinsic magnetic moment (or just spin)[62].

Every electron in an atom has an orbital dipole moment and a spin magnetic dipole moment which combine vectorially, and the result of these two vector quantities combines vectorially with similar resultants for all the other electrons in the atom, and the resultant for each atom combines with those for all the other atoms in a sample of a material.

When all of the magnetic dipole moments are aligning, this produces a magnetic field, and therefore the material will become magnetic [52, 63].

1.5.1. Magnetic fields vector

When some materials are susceptible to an external magnetic field **H**, the individual atomic magnetic moments contributing to their magnetization **M**, producing magnetic induction B, describe above:

$$\mathbf{B} = \mu_0(\mathbf{H}+\mathbf{M})$$

Where μ_0 is the magnetic permeability in the vacuum, the external magnetic field tends to line the magnetic dipoles moment (the induced and the permanents) inside of the material, in this situation it is said that the material is magnetized [64].

A magnetized material is normally described by they own magnetisation **M**, defined by the sum of all elementary magnetic moments, by unit of volume. For paramagnetic and ferromagnetic

materials, **M** has the same direction as **H,** for diamagnetic materials M is opposite to H. In most situations the magnetisation is proportional to the magnetic field applied for paramagnetic and diamagnetic materials [64, 65].

The magnetisation can be representing by:

$$M = \sum_{i}^{n} \frac{m_i}{V}$$

Where n correspond to the total number of magnetic moments m, and V is the total volume witch them occupied. In practice the more appropriate to define magnetisation is to divide for the mass m instead of volume giving the magnetic moment per unit mass σ [66].

$$\sigma = \frac{nm}{m}$$

1.5.2. Magnetic susceptibility

The response of the material to an applied field is characterized by the behaviour of the magnetisation, which is represented by magnetic susceptibility (χ), where $\chi = M/H$ [49, 66].

With the magnetic susceptibility it is possible to observe different types of behaviour of the magnetic field applied to the atoms, in which is represented by different types of magnetism [39].

Diamagnetic Materials (Zn, Cd, Cu, Ag, Sn) – Under the presence of external magnetic field, the atoms of a material are susceptible to low perturbations on the electrons in orbit that originate small magnetic dipoles in the atoms, in which they are opposed to the applied field. This interaction gives a negative magnetic effect known as diamagnetism [37, 39].

Paramagnetic materials (Al, Ca, Pt, Ti) – Paramagnetism results of the alignment of the magnetic dipoles on the individual atoms in an applied field. The materials have low positive values of χ the magnetisation field disappears when the external applied field is removed. [37, 39].

Ferromagnetic materials (Fe, Ni, Co) – In the ferromagnetism when the applied field is removed, the material retains most of the magnetisation some metallic materials possess permanent magnetic moment in absence of an external field showing high permanent magnetisation. In the ferromagnetic materials, the unpaired dipoles easy align with the applied

magnetic field, and therefore high magnetisations are obtain even for weak magnetic fields [39, 65].

Antiferromagnetic materials (Mn, Cr) – In antiferromagnetic materials the magnetic dipoles of the atoms align equally in opposite directions, cancelling each other out and making the global magnetisation null [65, 67].

Ferrimagnetic materials (Fe_2O_3, magnetites, other metallic oxides in general) – This is a type of magnetism present in ceramic materials, where the ions have magnetic dipoles with different intensity. The dipoles are aligned in differing directions but are not equal, and do not cancel each other out totally, leaving a net magnetic moment. This net moment may be small, but when aligned by a magnetic field the moments can align, and therefore this kind of material can provide high magnetisation on imposition of a field [68].

1.5.3. Concept of domains

In magnetic materials such as iron and steel, the magnetic fields of the electrons become aligned forming regions where they show spontaneous magnetism, these regions are call domains. In a non-magnetized sample of a magnetic material the domains are randomly distributed and the total magnetic field at any direction is zero, as shown in figure 4 [69].

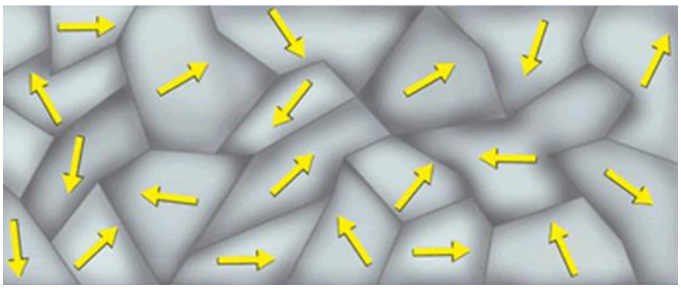

Figure 4: Magnetic Domains misaligned [70]

When an external magnetic field is applied to magnetic materials, the aligned domains grow at the expense of the others unaligned domains. If a strong –enough external field is applied, all of the domains will change to the direction of the external field (figure 5Figure 5), and after the domains have realigned along the field direction, the magnetisation of the material will not increase. In this case it is said that the material reaches magnetic saturation [54].

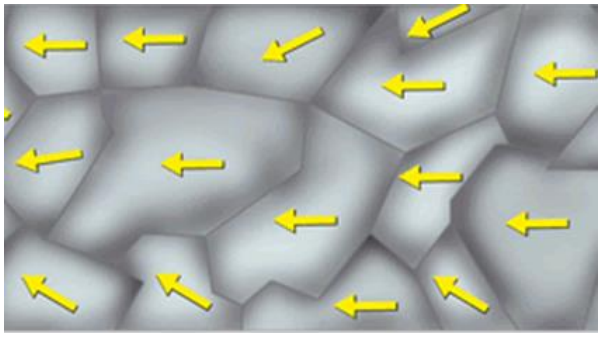

Figure 5: magnetic domain aligned [70].

When the external magnetic field is removed, the alignment of the domains will decrease and the magnetisation inside the material decreases to an inferior value, not necessary equal to that it had previously, as only some of the domains will return as they were [54]. This is how a material can become magnetised, and keep a net magnetisation after the field is removed, the figure shows a typical magnetisation in grains of a material, other else will be only visible one large domain.

1.5.4. Magnetostriction

There are some materials that can change shape when in presence of an external magnetic field, this effect is called magnetostriction. Magnetostrictive materials are able to convert magnetic energy in to mechanical energy, or in reverse, and this effect occurs in most ferrimagnetic materials. This phenomenon is attributed to the rotations of small magnetic domains in the material, which are randomly oriented when the material is not exposed to a magnetic field as in figure 6. The orientation of these small domains by the imposition of the magnetic field creates a strain field and produces a physical length change in the material. As the intensity of the magnetic field is increased, more and more magnetic domains orientate themselves so that their principal axes of anisotropy are collinear with the magnetic field in each region and finally saturation is achieved

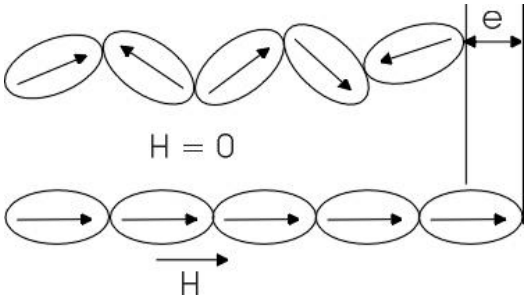

Figure 6: Dipole rotation under the presence of an external magnetic field

The best known pure element with highest magnetostriction at room temperature is cobalt, which saturates at 60 x 10^{-6} strain [71]. There are other materials with high magnetostriction, for example the amorphous alloy $Fe_{81}Si_{3.5}B_{13.5}C_2$ with its trade name Metglas 2605SC has a magnetostriction constant about 20 x 10^{-6} strains in a presence of low magnetic anisotropy field less than 1 kA/m [72], but the highest known magnetostriction is exhibited by Terfenol-D ($Tb_xDy_{1-x}Fe_2$) it shows about 2 x 10^{-3} strains in a field of 160kA/m (2 KOe) at room temperature. Terfenol-D is the most commonly used engineering magnetostrictive material [73].

1.5.5. Magnetisation Curves and Hysteresis Loops

It is possible to retrieve large information about the magnetic properties of a material by studying its hysteresis loop, figure 7. The hysteresis loop shows how to make a relationship between the induced magnetic flux density (B) and the magnetising force (H).

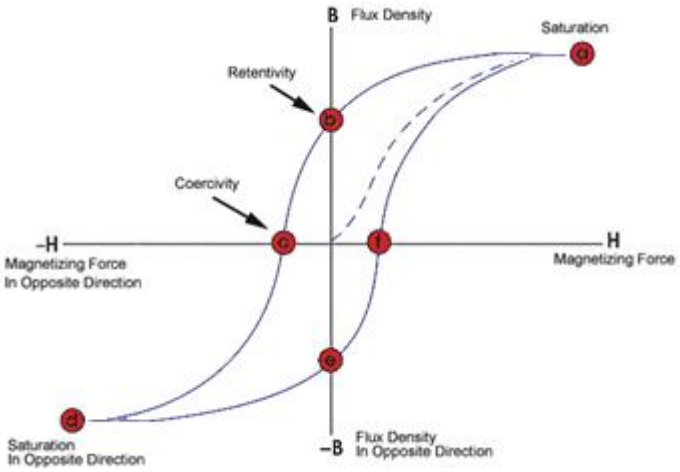

Figure 7 : Hysteresis loop induced magnetic flux density (B) and magnetizing force (H) relationship [74].

The hysteresis loop gives information about the magnetisation and demagnetisation of a material. Soft magnetic materials show a typical intrinsic coercivity lower than 1000 Am^{-1} and a reduced remanent magnetisation. Therefore, this materials show a hysteresis curve with small area [30, 41, 64].

The Hard magnetics, or permanent magnets, are hard to magnetise and demagnetise. They are characterised by having a high coercivity, high remanent magnetisation, the hysteresis loop produced by this type of material have a large area. The hard magnetic materials such as M ferrites are good for storing stronger magnetic fields [41, 64, 75].

1.5.6. Magnetic Anisotropy

Ferromagnetic materials exhibit intrinsic `easy' and `hard' directions of the magnetisation. Magnetic anisotropy is the most important property of magnetic materials, from both technological and fundamental point of view. It is a dependence of internal energy in relation to the direction of spontaneous magnetisation and this dependence is given through magnetic energy of anisotropy [76].

There are several types of anisotropy:

1. Magnetocrystalline – crystal structure (ferromagnetic – materials)
2. Shape – grain shape
3. Stress – applied or residual stresses

Magnetic anisotropy strongly affects the shape of hysteresis loops and controls the coercivity and remanent magnetisation [77].

1.5.7. Magnetocrytalline anisotropy

In the ferromagnetic crystals there is an energy that tends to preferably rearrange the vector of magnetisation according to a given direction, depending on the resulting magnetisation from the external applied magnetic field, from the strength of field and crystallographic direction [69].

The dependence of the magnetic properties with the crystallographic directions is known as magnetocrystalline anisotropy (MCA), and the energy that is linked or associated is known as magnetocrystalline anisotropy energy or anisotropy energy This energy has a higher value when the magnetic moments are oriented along the preferential magnetisation axis, this axis are known as easy magnetisation axis [30].

In the figure 8, is possible to see the magnetisation curves (magnetic moment vs applied magnetic field) of the crystalline cubic structure of magnetite, the magnetisation saturates easily in the direction <111>, or so called easy axis of magnetisation. In the axis <100>, hard axis of magnetisation is more difficult for the magnetisation to saturate; therefor the magnetocrystalline energy will be much higher than in easy axis [30, 77].

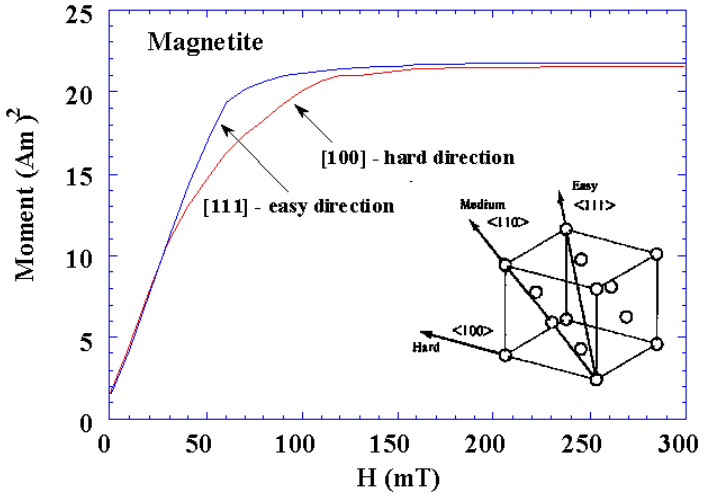

Figure 8: Magnetisation curves for magnetite [77]

1.5.8. Magnetic properties of hexagonal ferrites

All the hexagonal ferrites contain at least one large metal ion (usually Ba^{2+} or Sr^{2+}), this produces a small distortion in the lattice due to different sizes of the ions, the distortion is responsible for the magnetocrystalline anisotropy in the hexaferrites.

Most of the hexagonal ferrites have a preferred axis of magnetisation along the c-axis, the loose crystals in an applied field will align themselves with the c-axis parallel to the field. Applying a magnetic field in different directions produces different magnetic proprieties, if a field is parallel

to c-axis the H_c is larger and M_s saturates at a lower applied field compared to an applied field perpendicular to the easy axis[30].

However, all the Co_2 hexaferrites, and almost Y ferrites, are ferroxplana with a preferred direction of magnetisation either in the hexagonal basal plane or in a cone at an angle to the c-axis. In the ferroxplana ferrites the magnetisation can rotate within the plane or cone, opposite than in uniaxial ferrites that the magnetisation is locked in the same orientation, to displace the magnetisation out of the plane or cone is necessary anisotropy energy, this energy oppose to the rotation within the plane, This is a weak energy compared to the crystalline anisotropy which is high in all hexagonal ferrites. Therefore, the magnetisation will be free to rotate within the plane.

1.5.9. Barium Titanate

Since it was discovered Barium titanate ($BaTiO_3$), has been object of a vast studies made by researchers due its attractive proprieties. $BaTiO_3$ is a ferroelectric material with good electrical proprieties at room temperature, and is very stable chemically and mechanically. It can be easily prepared and used in the form of ceramic polycrystalline samples. $BaTiO_3$ shows high dielectric constant and low loss characteristics, and these proprieties are useful to make devices such capacitors and multilayer capacitors (MLCs), and when doped with other elements such Strontium or Lanthanum, $BaTiO_3$ can be used in a more wide application - semiconductors, PTC thermistors, dielectric bolometer, infrared sensors and others [78].

$BaTiO_3$ belongs to the large family of compounds called perovskites, ceramic materials with a perovskite structure. It has a molecular mass of 223.192 g mol^{-1} and a density of 6.02 g cm^{-3}.

The perovskite structure was named from the mineral perovskite, $CaTiO_3$, discovered by Gustav Rose in 1839 [79]. The stoichiometry of the perovskite structure is ABO_3, the ideal perovskite structure adopts the cubic space group Pm3m, where the metallic oxides possess face-centered cubic (fcc) structure, defined by the cations A and B, where A is a large divalent cation situated in the corner of the cube, B is a smaller tetravalent cation in the middle of the cube and O is an anion commonly oxygen, in the centre of the face edges as described in figure 9. When the cation A possess a large ionic radius, as is the case of Pb, Ba or Sr, the structure becomes distorted in which results polarisation [80].

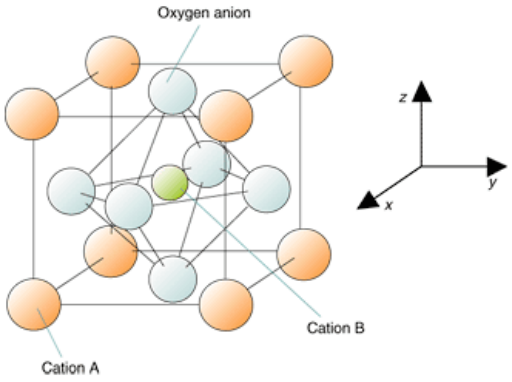

Figure 9: Crystallographic structure of ABO_3 perovskite [81].

The $BaTiO_3$ have different crystal structures depending of the temperature as shown in the diagram below [82].

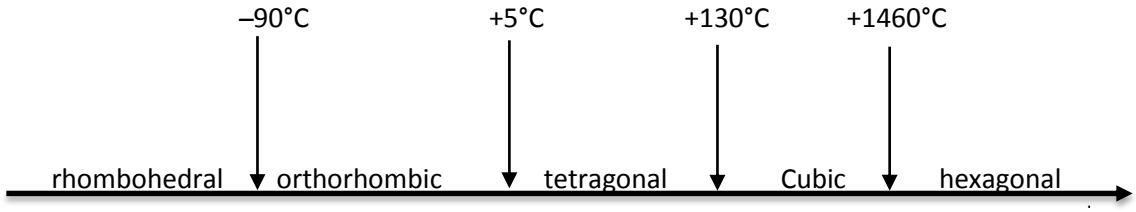

From high temperatures of 1460 °C down to the T_c (~120 °C for classical ferroelectric materials and ~130 for polycrystalline $BaTiO_3$), the barium titanate crystal structure is cubic, with the central titanium ion are surrounded by oxygen's ions (O^{2-}), each on one of the cube faces, and completing the structure there is one Barium ion in each corner of the cell as shown in figure 10-A In this cubic crystal structure there is not a dipole moment or piezoelectric properties [79, 80].

Below T_c the crystal structure of barium titanate adopts a tetragonal structure (figure 10-B), the atoms of titanium and barium are dislocated resulting in slight distortion of the structure. At this temperature the crystallographic structure passes from cubic paraelectric phase to the first ferroelectric tetragonal structure.

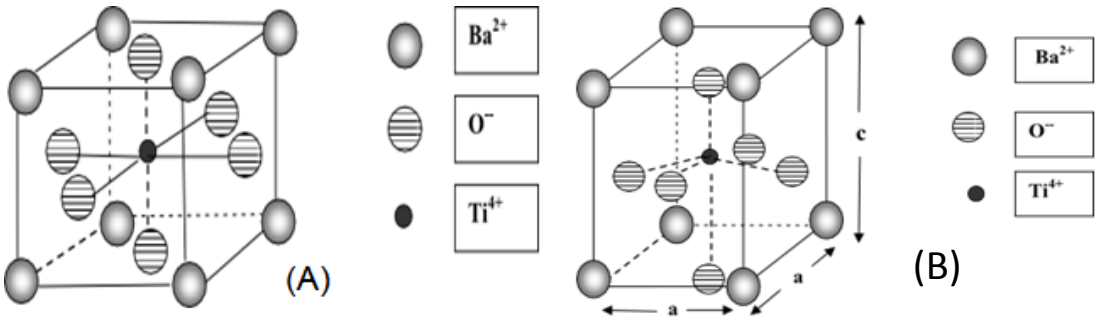

Figure 10: Cubic (m3m) crystal structure of $BaTiO_3$ above T_c - A, Tetragonal crystal structure of $BaTiO_3$ at room temperature [78, 82].

The titanate ions and the octahedral arrangement of the oxygen ions dislocate asymmetrically causing a permanent electric dipole moment on the unit cell. At this temperature range the crystal structure is stable and shows ferroelectric proprieties along the direction <001> and high a dielectric constant ideal for capacitors [82].

For temperatures below 5 °C the ferroelectric proprieties are maintained by changing the direction of the polarization to firstly the <110> orthorhombic crystal structure, and then to the direction <111> in the rhombohedral structure [83].

1.5.10. KNN

Alternatives to lead-free piezoelectric materials have been studied for some long time due to possible environmental and biological contamination from the lead in lead zirconate titanate (PZT) materials. The ceramic material $(K_{0.5}Na_{0.5})NbO_3$ (KNN) has the structure of perovskite as shown in figure 11, and has excellent piezoelectric proprieties, considered by many researchers to be a promising candidate to replace PZT due the similar electrical properties of both ceramic materials, and the piezoelectric properties have the same order of magnitude, and it has a large electromechanical coupling factor [84, 85].

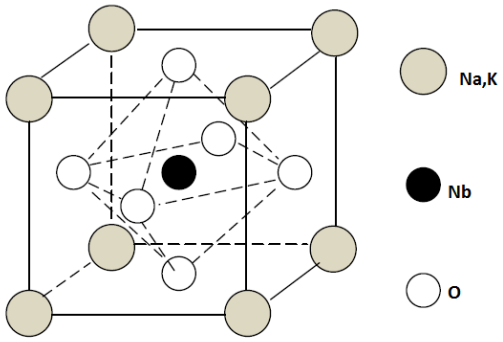

Figure 11: Schematic representation of perovskite structure of sodium potassium niobate [86].

KNN is a solid solution of sodium niobate and potassium niobate ($KNbO_3$-$NaNbO_3$). The Potassium niobate (KN) that constitutes the KNN system is a ferroelectric material with orthorhombic symmetry at room temperature. The phase transitions are similar to $BaTiO_3$ but with a higher T_c of about 420 ºC. On the other hand, $NaNbO_3$ (NN) is an anti-ferroelectric material with orthorhombic structure, at room temperature it has a T_c lower than KN at about 355 ºC. Combining these two materials results in a ferroelectric material with high T_c of 400 ºC. The critical electric

field decreases when both materials are combined inducing a ferroelectric phase transition. To make KNN a minimum amount of 0.6 atomic percent K^+ is needed to induce a ferroelectric phase in the NN host.

Unmodified KNN ceramics are difficult to obtain due the reactivity of Potassium, the Potassium should be handle above temperatures of 18 °C, in an atmosphere with low humidity to reduce the risk of reaction with water. The KNN exhibits poor aging in air, the samples have better piezoelectric properties if they are obtained by hot pressing or hot forging [85, 87]. The KNN has a molecular mass of 171.948 g mol^{-1}, and a density of 4.50 g cm^{-3} [88].

2. Characterization techniques

To characterize a sample´s properties some knowledge is required of a wide range of experimental techniques to obtain the desired information. To obtain certain degree of accuracy it is necessary to use various analysis techniques to obtain qualitative or quantitative data to fulfil the research objectives.

2.1.Scanning Electron Microscope - SEM

The scanning electron microscope (SEM) is known to be a very powerful instrument for scientific research, his high proposes is to help in the development and control of quality of materials. This technique is used to characterize the microstructure of the samples and ponders, surface topography and composition.

The images from SEM has a characteristic tri-dimensional appearance they are useful to evaluate the superficial structure of a given sample. The surface to analyse is systematic scanned with an electron beam and secondary electrons the reflected beam (or back-scattered) of electrons is collected by appropriate detectors, then displayed at the same scanning rate on a cathode ray tube. The image on the screen represents the surface features of the sample and it can be photographed. Because of the use of electrons the image resolution obtain is far superior then the optical microscopes, achieving great depths-of-field it can reveal details with sizes less than 1 nm [89].

Due the variety of the interactions between electrons and matter, is possible to obtain specific information, depending of the detected signal. The signal's normally used in material science are: secondary electrons (SE), back-scattered electrons (BSE) and characteristic X-rays. The SE have very little energy (0 to 50 eV), the signals result from interactions of the electron beam with atoms at or near the surface of the sample giving information about the topography of the surface.

In this work we used the SEM from Hitachi, model SU-4100, that has high resolution and it is capable of detecting features of 2 nm at 15 kV. The characterization techniques and their properties used in this work are shown in a in annex b.

2.2.X-Ray diffraction - XRD

The X-Ray technique is a rapid analytical technique primarily used for phase identification of a crystalline material and can provide information on unit cell dimensions, using the XRD diffactogram it is obtained a fingerprint of the substance,the mix of the crystalline phases can be easy distinguished and be compared with the reference diffractograms giving information about the crystalline composition and purity of the phase. The XRD beam is characterized by electromagnetic waves of high energy (3 KeV to 8 KeV), with a wave length lower than visible light (0.01 – 10 nm), comparable with the interatomic distance of the crystals (0.5 – 2.5 Å) [90].

When a crystalline substance is hit by a beam of X-Rays the electrons around the atoms start to oscillate with the same frequency as the incoming beam, reflecting the incident radiation (diffracted rays), revealing the differing planes or atomic layers of the crystal. To maximize the intensity of the diffracted ray it is necessary to have a relationship between several elements: the wave length of the incident radiation, the distance between the crystals planes (interplanar distance) and the angle of incidence, or in other words, this must obey Bragg's law, which is defined by the following equation:

$$n\,\lambda = 2\,d_{hlk}\,sen\,\theta \qquad \text{Eq: 1}$$

Where n is the order of diffraction, λ is the wavelength of incident wave, d is the spacing between the planes in the atomic lattice, and θ is the angle between the incident ray and the scattering planes as shown in figure 12 [91, 92].

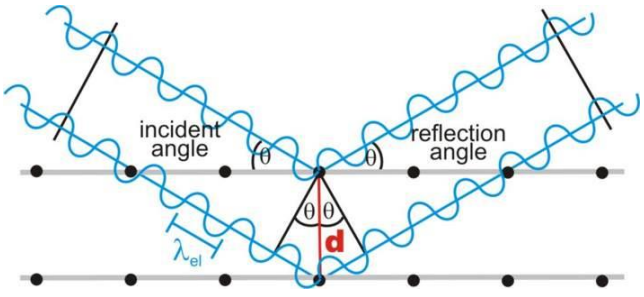

Figure 12: Bragg diffraction constructive interferences[93].

When the beams of X-rays (λ) is diffracted from a crystal, they can produce two types of interference, destructive and constructive. If the waves are out phase then destructive interference occurs, and the opposite when the waves are moving in phase with each other in constructive interference. Through the constructive interference the diffractions maximums are built as a series of peaks, and the interplanar distance between the atoms obtained showing the characteristics of the crystal.

To calculate the dimension of the unit cell it is necessary to use a form of notation system for the planes in crystal (Bravais) lattices. Such notation is known as the Miller index (hkl), and each the index denotes a plane orthogonal to a direction on the basis of the reciprocal lattice vectors.

2.3.Piezoresponse force microscopy - PFM

Piezoresponse force microscopy, PFM, is a variant of atomic force microscopy that belongs to the family of Scanning probe microscopy, SPM, in which is grouped all technique's based on scanning the surface of samples with probes.

The PFM measurements are made through the inverse piezoelectric effect, the piezoelectric material having a mechanical deformation, contraction or expansion under the influence of an applied electric field. With this technique it is possible to observe and modify the local domains of the ferroelectric structures, the ferroelectric domains respond to an electrical field with a characteristic deformation in a characteristic magnitude and sign.

To obtain the piezoresponse the microscope is operated in a contact mode, applying an AC voltage to a conductive tip, acting like a movable top electrode coupled to the ferroelectric (piezoelectric) surface in a sample that is connected to the ground (bottom electrode,) represented in figure 13. The movement of the tip produces a vertical displacement on the cantilever (z-direction): this means that the domains are electrically polarized and perpendicular to the sample surface. If they are parallel to the electrical field, the domains would experience a vertical expansion. If the domains are anti-parallel to the applied field, this will decrease the cantilever deflection, figure 14. The displacements produce oscillations of the cantilever giving information about the amplitude and phase through a lock-in, and the surface strain is amplified and recorded obtaining the topography of the sample [94-96].

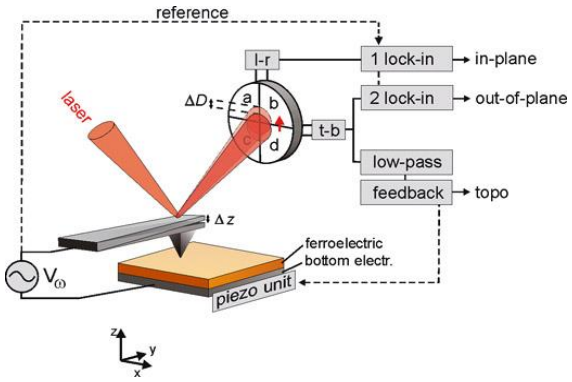

Figure 13: PFM setup to simultaneously acquire the topography and the in- and out-of-plane component of the polarization. A function generator is used to apply an alternating voltage Vw between the tip and the bottom electrode of the ferroelectric. The voltage induced cantilever deflection is detected by a reflected laser beam on a four sector photodiode [97].

Most PFMs use the Lock-in technique, this technique consisting of a Lock-in amplifier that uses the signal recovery approach, capable of recovering signals smaller than the mixed noise. The Lock-In technique, also known as a phase-sensitive detector, gives single components of a signal at a specific reference frequency and volume of phase. The Lock-in technique uses a reference frequency to detect the response from the experiment, the reference signal is a square wave at frequency ω_r and the response signal is $V_{sig}\sin(\omega_r t + \theta_{sig})$, where V_{sig} is the signal amplitude, ω_r is the signal frequency and θ_{sig} is the signal's phase [98].

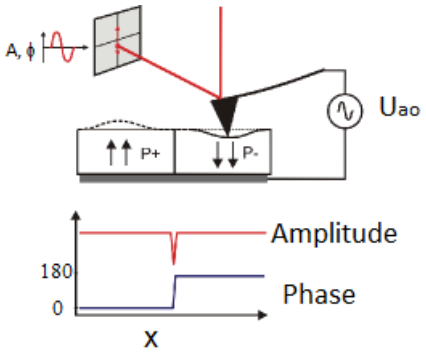

Figure 14: Cantilever deflection produce by the polarization of the domains, An a AC voltage is applied between sample and tip, making the piezoelectric domains expands or contracts depending of the bias-sign and the orientation of the domains will give an in-phase response for P+ or out-of phase response for P- domains. The amplitude response is independent from the direction of domain polarization [99].

The response signal gives the piezoelectric response, through the first harmonic of the signal frequency produced by the tip of the cantilever. The amplitudes of the oscillations out of plane are related to the piezoelectric coefficient d_{33} (change in volume) of the material and the phase is related to the orientation of the polarization. When the amplitudes are in plane they are

proportional to the piezoelectric coefficient d_{31} (change in length). From these values the piezoelectric hysteresis loop is obtained [100].

Before making measurements of PFM (NT-MDT Co., model NTEGRA Aura), the samples were polished with sand papers with different granulometry (800, 1000, 1200 and 2500), and then the samples were cleaned ultrasonically with isopropanol for 10 min, and left to dry, after which they were polished with different grades of diamond paste to obtain a very smooth mirror-like surface.

2.4.Magnetic Force Microscopy – MFM

In Magnetic Force Microscopy, MFM, the cantilever is equipped with a magnetic tip which interacts with the magnetic fields near the surface of the samples. With this technique the magnetic domains of the structure are revealed. MFM is used for the study of magnetic data storage devices properties, magnetic structure of magnetics with sub-micron resolution, busbars magnetic fields etc.

The main advantage of MFM is that it has high resolution [101]. The MFM operates on the same principles as the AFM, both use two different detection modes, static and dynamic, but MFM is more often used in the dynamic mode, because it has better sensitivity. In a static mode the cantilever has contact with the sample and the contours of the surface, and the measurements are made directly using the deflection of the cantilever. The speed of analysis is higher than in dynamic mode, and the topography obtained has higher resolution. In the dynamic mode, the tip is not in contact with the sample (or has semi-contact), and the cantilever oscillates at a frequency slightly above the resonance frequency, or in some cases the tip intermittently touches or “taps” the surface. The advantage of tapping the surface is to gain better lateral resolution on soft samples [102].

To better understand MFM we need to know which forces act on the tip of the cantilever. There are two main forces in magnetic materials: The magnetic force and the inter-atomic force, in this case Van der Walls. The magnetic force gives information about the surface magnetic property and the Van der Waals gives information about the surface topography (Topo signal).
To make topography measurements or obtain information about magnetic properties the LiftMode technique was used [101, 103].

In the LiftMode, as shown in figure 15, the tip is raised just above the sample surface. First

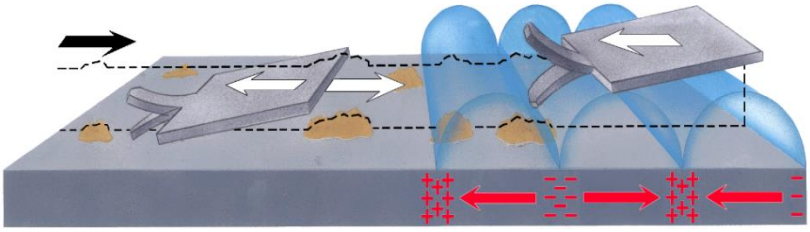

Figure 15: LiftMode Technique [102].

the surface is scanned for topography, and the influence of magnetic forces monitored. Then they are measured using the principle of force gradient detection - in absence of magnetic forces the cantilever has a resonant frequency f_0. This frequency is shifted by an amount Δf, proportional to vertical gradients in the magnetic forces on the tip.

To make the measurements the samples were polished, although some had shown some roughness above 1 µm, and the same equipment was used as for PFM (NT-MTD). To make the measurements we used special cantilevers; a soft magnetic cantilever PPP-LC-MFMR with a remanence magnetization of approximately 225 emu cm^{-3} and coercivity of 0.75 Oe manufactured by Nanosensors.

2.5.Vibrating sample magnetometer - VSM

The vibrating sample magnetometer, VSM, is one of various techniques that measures the magnetic properties as a function of field, temperature and time. With VSM measurements it is possible to determine an aptness of a magnetic material for a specific application. It allows us to study the magnetic properties such as the hysteresis loop, magnetic susceptibility or the saturation magnetization.

The working principle of VSM is based on Faraday's law of electromagnetic induction, in which states that an electromotive force (*e.m.f.*) will be generated in a coil when there is a change in flux linking the coil.

$$Emf = -\frac{d\Phi}{dt}$$

Where $d\Phi/dt$ is the rate of change of the magnetic flux. Note: the negative sign is because of Lenz's Law, it states that the induced *e.m.f.* (and current) will be in a direction such that the induced magnetic field opposes the original magnetic flux change[104].

In VSM, a sample is placed inside a uniform magnetic field. If the sample is magnetic, this constant magnetic field will magnetize the sample by aligning the magnetic domains, or the individual magnetic spins.

The magnetized sample produces a magnetic field called the magnetic stray field, as the sample moves up and down this magnetic stray field changes as a function of time and will be sensed by the pick-up coils [105, 106]. The alternating magnetic field will cause an electric current in the pick-up coils according to Faraday's Law of induction, the electric current will be proportional to the magnetization of the sample, and the greater the magnetization the greater the induced current.

The induced current is measured through a Lock-in amplifier in which amplifies the signal, in this case the induced current [107].

The measurements of magnetisation as a function of the applied magnetic field were performed in a VSM equipment of CRYOGENIC Limited, with a resolution of $5x10^{-5}$ emu. The measurement ranges of the equipment are 1.5 to 320 K and -10 to +10 T, for temperature and magnetic field, respectively, in this work was made was used 3 T field at room temperature.

A summary of the basic functions of the measurements system used in this work can be consulted in annex b.

3. Procedure

The chemicals used in this work to synthesis the samples in the different techniques had high purity and were bought form well known suppliers. The list of the chemicals used is listed in table 2.

3.1.Solid state reaction route

3.1.1. Hexaferrites

To obtain the M-ferrites we made a mixture of carbonates $BaCO_3$, $SrCO_3$ and oxides Fe_2O_3 described in table 2, in the stoichiometric ratio of Ba or Sr to Fe_2O_3 is 1:6. After properly mixing with mechanical stirring for 10 min with isopropanol, the powders were put in a pot with zirconia balls, then placed on a mechanical ball mill, and left to mixing fo 12hours. After mixing, the pot was dried for 48h. The powder was then manually mixed in a mortar until the mixture was homogenous, and was then calcined at different temperatures of 1000 °C, 1050 °C, 1100 °C, 1150 °C, 1200 °C for 2 hours at 5 °C/min in air (figure 16).

The Z-ferrites were produced by the same method as the M-ferrites, but the oxides used were $BaCO_3$, $SrCO_3$, Co_3O_4 and Fe_2O_3 according to table 2. The stoichiometry ratio of Ba or Sr to Co to Fe_2O_3 used were 3:0.67:12. The calcination temperatures were the same as for M-ferrites, except for BaZ where the maximum was increased to the temperature 1250 °C.

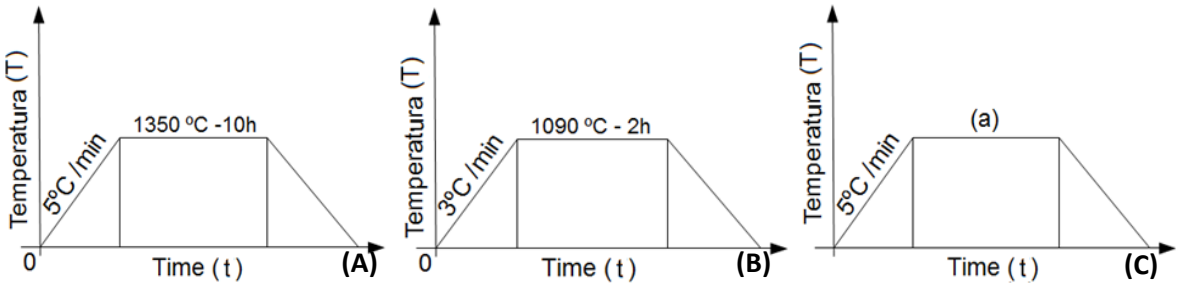

Figure 16: calcination diagrams: A - Hexaferrites of BaM, SrM, SrZ and BaZ in where "a" is a different calcination temperatures 1000 °C, 1050 °C, 1100 °C, 1150 °C, 1200 °C, and 1250 °C for the case of BaZ, B – Barium titanate, C - KNN .

3.1.2. $BaTiO_3$

Barium titanate was prepared by firing a mixture of barium carbonate ($BaCo_3$) and titanium (IV) oxide (TiO_2), table 2. The compounds were weighed and then mixed in a mortar until well mixed, put on a ball mill with zirconia balls for wet millinging with isopropanol, and left to mill for 12 hours. After this a fine mixture of the powder was dried in an oven until the complete evaporation of isopropanol had occurred, and the mixture was then calcined in a furnace at the temperature of 1350 °C for 10h as shown in figure 16-B.

Table 2: compounds for Hexaferrites of solid state reaction (BaM, SrM, BaZ SrZ) and KNN powder.

Compound	Chemical Formula	Molar Mass	Purity %	Supplier
Iron III - A.C.S reagent	Fe_2O_3	159,69	99	BDH Prolabo
Barium carbonate	$BaCO_3$	197,32	99+	Sigma-Aldrich
Strontium carbonate	$SrCO_3$	147,63	98+	Sigma –Aldrich
Cobalt (II,III) Oxide	Co_3O_4	240,80	99.9	Panreac Montplet and. Esteban S.A.
Titanium (IV) oxide – Reagent plus	TiO_2	79,87	99+	Sigma-Aldrich
Potassium Carbonate	K_2CO_3	138,21	99+	Sigma-Aldrich
Sodium carbonate	Na_2CO_3	105,99	99+	Sigma-Aldrich
Niobium (V) oxide	Nb_2O_5	265,81	99,99	Sigma –Aldrich

3.1.3. KNN

Potassium sodium niobate (KNN), was prepared from carbonates and oxides: K_2CO_3, Na_2CO_3 and Nb_2O_5 details in table 2. The powders were weighed according to the stoichiometric proportion (0.5:0.5:1), for the required compositions, and mixed for 24h in a ball mill, then dried for 24hours at 80 °C. The powder was calcined at 1090 °C for 2h as shown in figure 16-C.

3.2.Coprecipitation

The chemical method of Coprecipitation of salts with a base results in the formation of an insoluble precipitate (usually a hydroxide) from aqueous solutions of nitrates, chlorides or sulphates of Fe^{3+}, and of divalent cations such as Ba, Sr, Co, etc…, resulting in a precipitate containing all the components mixed at an atomic level. The wet chemical process improves homogeneity. In this process a strong base such as sodium hydroxide (NaOH) or ammonia (NH_3) is added to precipitate the solution. To avoid problems when precipitating it is needed to achieve a pH higher then 10, because of the different solubility dependences of some metal hydroxides, and because the cation ratios can be different in the solution [30, 75].

All of the hexaferrites made by this process had the same procedure: we calculated and measured the quantities of nitrates - for M-ferrites $Ba(NO_3)_2$, $Sr(NO_3)_2$ and $Fe(NO_3)_3 \cdot 9H_2O$ were used, and for SrZ and BaZ the same nitrates were used as in M-Ferrites, with the addiction of $Co(NO_3)_2 \cdot 6H_2O$ (table 3, in chapter 3.3). Each of the compositions was mixed by mechanical stirring (Stirrer ES VELP scientifica) in a 1000 ml beaker with distilled water.

The nitrates were dissolved in the water after 30 min. Then a total of 300 mL of ammonia solution with 5% concentration was added dropwise with constant mechanical stirring, causing a precipitate to form.

A pH of 9.3 was obtained in the solutions, and then the suspension was filtered to leave the solid part, which was washed with distilled water to remove most of the remaining nitrate and ammonium ions. The solid cake obtained was dried in an oven for 24h, then was calcined at different temperatures as in the Solid State Reaction route, diagram in figure 16-A.

This Process was repeated for all four compositions of hexaferrites.

3.3.Sol-gel

The sol-gel is a wet-chemical technique widely used in materials science to obtain ceramic materials, typically metal oxides. The chemical process of sol-gel is based in reactions of inorganic polymerization or metallo-organics on the colloidal scale. In general, the sol-gel process involves the transition of a solution system from a liquid "sol" (mostly colloidal) into a solid "gel" phase. Utilizing the sol-gel process, it is possible to fabricate advanced materials in a wide variety of forms:

ultrafine or spherical shaped powders, thin film coatings, fibbers, porous or dense materials, and extremely porous aerogel materials.

A Sol is a colloidal suspension of solid particles in a liquid were the gravity forces are cancelled by short range forces such as Van der Walls, surfaces charges and Brownian motion, and the particles within the sol typically have a diameter of 1 to 1000 nm. Sols are formed through a hydrolysis/ condensation reaction of colloidally-sized particles [30]. The hydrolysis happens when the metallic precursor is dissolved by water, then the metallic cations are hydrolysed by the water molecules and forms metal hydroxides, as shown in the equation:

$$M - X + H_2O \rightarrow M - OH + HX$$

Were the M is a metal and X is a reactive species such as nitrates. The reaction starts when the OH group is added, that reacts with the metal ion in solution. Condensation occurs by the linking together of hydrolysed molecules to form M-O-M connections, with the loss of a molecule of water:

$$M - OH + HO - M \rightarrow M - O - M + H_2O$$

There are many factors that influence the reactions in hydrolysis and condensation, such as pH, temperature, metal ions concentration [109].

When the sol starts to concentrate or condensation occurs, it forms a continuous amorphous connected structure knows as a gel.

To produce ferrites by aqueous sol-gel synthesis, an aqueous solution of metal is coprecipitated by a base, then instead of drying and firing the precipitates, they are treated to form a colloidal sol, which can then be concentrated to a gel and then can be dry to make powder or fired to give the ferrite.

In this work the sol-gel method was made through the coprecipitation method, but instead of drying and firing the precipitate, 3.5ml of nitric acid with 5% concentration (table 3) in 20mL of distilled water was added to it in an evaporating flask of 500mL volume. This was attached to a rotary evaporator (Rotavapor® R-210/R-215, Buchi) for 24h at a temperature of 60 °C. This enabled the hydroxides to peptise, and a colloidal suspension (sol) of hydroxides was obtained, and after this was dried in an oven for 48h to dry completely at the temperature of 85 °C, the gel obtained was calcined at different temperatures as in the solid state reaction route.

The process was repeated for all the M-Ferrites and Z-ferrites.

Table 3: Coprecipitation and sol-gel compounds BaM, SrM, BaZ, SrZ.

Compound	Chemical Formula	Molar Mass	Purity %	Supplier
Iron III nitrate nonahydrate – A.C.S reagent	$Fe(NO_3)_3 \cdot 9H_2O$	404	98+	Sigma-Aldrich
Barium nitrate – A.C.S reagent	$Ba(NO_3)_2$	261.34	99	Sigma-Aldrich
Strontium nitrate – A.C.S reagent	$Sr(NO_3)_2$	211	99	Sigma-Aldrich
Cobalt (II) nitrate hexahydrate – A.C.S reagent	$Co(NO_3)_2 \cdot 6H_2O$	291.03	98+	Sigma-Aldrich
Citric Acid monohydrate – A.C.S reagent	$C_6H_8O_7.H_2O$	210.14	99.5 - 102	Sigma-Aldrich
Ammonia solution	NH_3	35,05	25	MERC

3.4.Citrates synthesis

The citrate method constitutes a polymeric approach, in which different metals are confined in a gelified citric acid network. In this method ultrafine particles can be synthesised at low temperatures, through a violent exothermic reaction from the decomposition of the citrates, in which CO_2 is generated producing a very porous product with a high surface area.

In this process the acid citric acts as a complexing agent forming metal-citrato complexes, the metal precursors used are normally the nitrates with water as solvent.

To Make BaM and SrM a stoichiometric solution of nitrates ($Ba(NO_3)_2$, $Sr(NO_3)_2$, 12 $Fe(NO_3)_3 \cdot 9H_2O$) described in table 3 was mixed with a magnetic stirrer with distilled water until it became homogeneous, after which was added acid citric in a ratio of cation : citrate =1. The solution was heated to 80 °C, and ammonia was added until the pH reached 7.0 to form a homogenous solution. The solution was taken to the rotary evaporator (Rotavapor® R-210/R-215, Buchi) to evaporate most of the water, and the rest of the water was removed by drying in an oven for 72 hours. After complete drying, it was heated to a temperature of 200 °C, and a mixture of oxide compounds was formed in the subsequent exothermic reaction, which may contain some ready-formed hexaferrites. These powders were then calcined as before.

The BaZ and SrZ was made by the same process with a stoichiometric solution of $Ba(NO_3)_2$, $Sr(NO_3)_2$, 12 $Fe(NO_3)_3$, $Co(NO_3)_2 \cdot 6H_2O$) as describe in table 3, and also was calcined at the same temperature as the others methods already referred.

3.5.Composites

The ceramic composites were made by mixing each of the hexaferrites (BaZ, SrZ, BaM, SrM) from each process described above with the different piezoelectric ceramics, in the following ratios in weight percent:

Hexaferrites 90% - $BaTiO_3$ 10%	Hexaferrites 90% - KNN 10%
Hexaferrites 80% - $BaTiO_3$ 20%	Hexaferrites 80% - KNN 20%
Hexaferrites 70% - $BaTiO_3$ 30%	Hexaferrites 70% - KNN 30%

After a proper mix in the mortar, pellets were prepared in a uniaxial press with a dye diameter of 10mm and a pressure of 100 MPa. For each composition of different ratio 3 samples were made. For the solid state route this made a total of 64 samples, 32 samples with $BaTiO_3$ and 32 samples with KNN, and the process was repeated for the others methods (coprecipitation, sol-gel and citrates synthesis), totalling 288 samples.

Some of the samples were given further cold isotactic pressing (cip) under the pressure of 200 Mpa for 5 minutes. After pressing the pellets were weighed, and sintered at different temperatures. The composites of $BaTiO_3$ were sintered at 1200 °C for 2 hours and the composites of KNN were sintered at 1090 °C. The sintering time and temperatures were the same used to make the KNN and BaM, SrM and SrZ Hexaferrites, as indicated in figure 16. After the sintering the density of the pellets was obtain thought the measured of the weight, diameter and height. Some of the pellets were polished with sand paper (800, 1000, 1200 and 2500), and diamond paste (15 µm, 9 µm, 6 µm, 3 µm and 1 µm) to obtain a fine shinny surface for PFM and MFM measurements. Others samples were taken for XRD, VSM and SEM analysis.

4. Results and Discussion

4.1.Density

The geometric density of the pellets were calculated using a calliper, precision balance and through the equation below:

$$\rho = \frac{m}{V}$$

Where ρ is density of the material, *m* the mass (g) and *V* is the volume (cm^3).

Through the tables below is possible to compare the density of the processes and compositions of the composites using uniaxial pressure and cold isotactic pressure.

To compare with the experimental values, the theoretical values of density were calculated for the composite mixtures as shown in table 4, using published data for the pure compounds from XRD pattern files and some bibliography. In the theoretical density was not taken in consideration the secondary phases formed, just the phases that we pretend to obtain, it was done to simplify the results.

Table 4: Theoretical density of the composites hexaferrites with the ferroelectrics (BT, KNN).

	BT			KNN		
	90 - 10	80 - 10	70 - 30	90 - 10	80 - 10	70 - 30
BaZ	5.43	5.52	5.60	5.28	5.20	5.12
SrZ	5.23	5.34	5.45	5.06	5.01	5.00
BaM	5.44	5.52	5.60	5.29	5.21	5.13
SrM	5.22	5.33	5.44	5.05	4.99	4.93

4.1.1. Composites of hexaferrites with $BaTiO_3$

The results of density are important to determine the structure of the material, to see if it contains too many porosity or is a dense structure.

The density obtained on the uniaxial press (table 5) is lower than the theoretical density (table 6), being about 56% to 75% of maximum theoretical density (tables in appendix a).

Table 5: Density of BT composites, uniaxial press

Hexaferrites + $BaTiO^3$					
Uniaxial Press (g/cm^3)					
	%	Solid state reaction	Sol-Gel	Coprecipitation	Citrates
BaZ -BT	90 - 10	3.72	3.59	3.60	3.47
	80- 20	3.69	3.44	3.52	3.64
	70 -30	3.81	3.50	3.50	3.80
SrZ - BT	90 - 10	2.89	3.48	2.93	3.28
	80- 20	3.09	3.40	3.12	3.56
	70 -30	3.31	3.40	3.16	3.89
BaM -BT	90 - 10	3.53	3.73	4.06	3.89
	80- 20	3.62	3.99	4.09	3.99
	70 -30	3.65	4.08	4.20	4.02
SrM -BT	90 - 10	3.05	3.77	4.00	3.53
	80- 20	3.39	3.64	4.13	3.71
	70 -30	3.52	3.89	4.09	3.69

With the density chart in figure 17, is possible to visualise the difference of density between the used methods and the different composites. In the BaZ compositions it is noticed that the method of solid state reaction has higher density, but even then the difference is not much compared with the other methods. In the SrZ compositions, the citrates have higher density in compositions with 20% and 30% of BT, but only in composites with 10 % BT is the density better with the sol-gel method. The density of SrZ composites are lower than BaZ composites in most of the cases, due the different weight of barium and strontium.

In the M-ferrites the method of coprecipitation gave a higher density. Also, M-ferrites have higher density than Z-ferrites, which may happen due to the size of the grains, as in the Z-ferrites the grains are much bigger, and contain more porosity between the grains.

The composition showing highest density in the uniaxial press is BaM comparing with the other results, and SrZ compositions have the lowest density. Comparing the best results obtained in the uniaxial press (BaM, coprecipitation) with the theoretical density, the experimental density was 75% of the theoretical density and the lowest experimental density is 56%, for solid state reaction of SrZ with 10 % of BT.

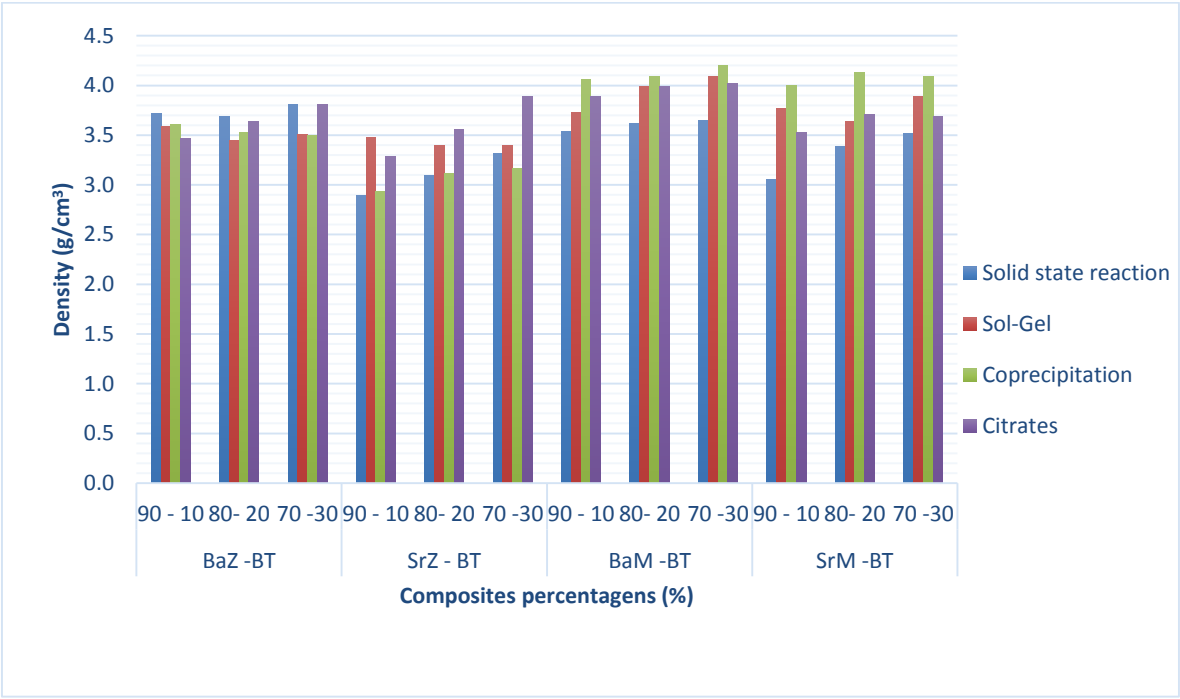

Figure 17: Density chart of BT composites from uniaxial press.

Cold isotactic Press

With cold isotactic press the densities of the composites in general have increased (table 6), compared with the results of the uniaxial press. Some of the composites have increased as much as 10 %. However, in the BaZ composites of solid state reaction it is noticed that the density is lower than with the uniaxial press, although this may be due to experimental problems, as this happens when the sample breaks.

Comparing the density of table 6, with the maximum theoretical density it is verified that it is approximately 63% to 81% of the theoretical values.

The best density achieved was in SrM 80 – 20 BT with the method of coprecipitation, at 81%, and the highest density in the cold isotactic pressing of BT composites was 4.3 g cm^{-3}.

Table 6: Density of BT composites through cold isotactic pressure process

Hexaferrites + $BaTiO^3$					
Cold isotactic press (g/cm^3)					
	%	Solid state Reaction	Sol-Gel	Coprecipitation	Citrates
BaZ - BT	90 - 10	3.45	3.45	3.64	3.68
	80- 20	3.53	3.74	3.70	3.83
	70 -30	3.77	3.75	3.73	3.89
SrZ - BT	90 - 10	4.03	3.51	3.28	3.35
	80- 20	3.83	3.64	3.36	3.74
	70 -30	4.15	3.73	3.41	3.94
BaM -BT	90 - 10	3.94	3.63	4.20	3.63
	80- 20	3.97	4.10	4.31	4.10
	70 -30	3.98	4.06	4.31	4.06
SrM -BT	90 - 10	3.56	3.80	4.22	3.80
	80- 20	3.83	3.96	4.33	3.96
	70 -30	3.97	4.03	4.34	4.03

With the chart in figure 18, it is possible to see the different geometric densities of each method and composites. Of the Z-ferrites, the SrZ ferrite has the lowest density in most of the methods, with the exception of the solid state reaction in which it is higher. For BaZ composites the method that gave more density was the citrate route.

In the M-ferrites the method of coprecipitation shows high density compared with the others, and in general the BaM composites have higher density, the SrM in particularly for 80 - 20 composites, showed the highest density of 81 % compared with the theoretical density. Almost reaching the maximum density expected in ceramic composites about 90%.

The M-ferrites show a higher density then the Z ferrites, in both pressure methods, and this can mean that the M-ferrites are more compact than the Z-ferrites, in other words they have less porosity.

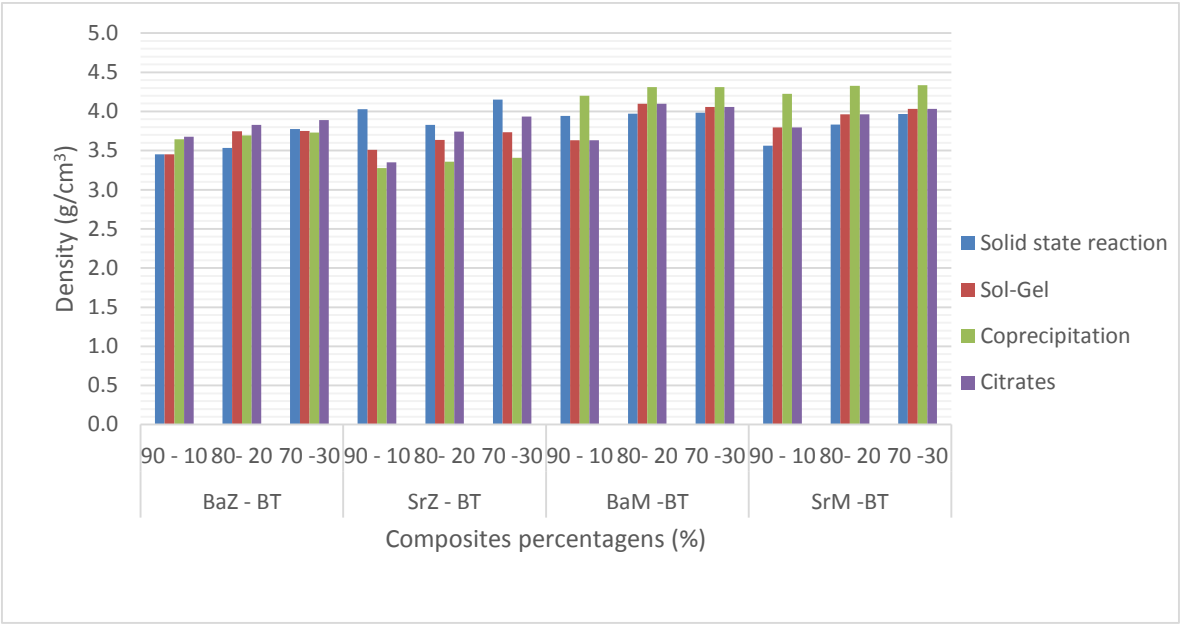

Figure 18: Density chart of BT composites from cold isotactic press.

4.1.2. Composites of hexaferrites with KNN

As expected the composites with KNN have lower densities than the composites with BT, due to the lower density of KNN.

Comparing the results of density in table 7, with the maximum theoretical density (table 4), it is verified that the density of the KNN composites are inferior, the lowest density being only 2.4 g cm^{-3} and the highest is 4.3 g cm^{-3}. The composites of KNN have a large range of density values compared with the density of BT composites made by uniaxial pressure, and comparing with the theoretical density the KNN composites have a density of only 45% to 81%.

In the chart on figure 19, it is possible to visualize the large difference of density between the compositions prepared by different methods used in this work.

The best method for the Baz composites was the coprecipitation showing high values of density compared with the other methods. In SrZ composites the density obtained was lower than BaZ composites. The higher density for SrZ with 10 % KNN was the method of sol gel, and with 20% and 30 % KNN the best method was Solid state reaction. For the M-ferrites, BaM shows higher density compared with SrM and the Z-ferrites, and the method that had the highest density was coprecipitation with 10 % of KNN. In the SrM composites the method of coprecipitation was higher with 10% and 20 % KNN, and with 30% KNN the best density achieved was with the sol-gel method.

Table 7: Density of KNN composites, uniaxial press.

Hexaferrites + KNN					
Uniaxial press (g/cm^3)					
	%	Solid state Reaction	Sol-Gel	Coprecipitation	Citrates
BaZ - KNN	90 - 10	2.4	3.1	3.6	2.4
	80- 20	2.4	3.2	4.0	2.4
	70 -30	2.5	3.1	3.6	2.5
SrZ - KNN	90 - 10	3.2	3.3	3.2	2.9
	80- 20	3.3	3.2	3.1	3.0
	70 -30	3.4	3.1	3.0	3.1
BaM - KNN	90 - 10	3.1	3.0	4.3	3.0
	80- 20	3.1	3.3	4.1	3.2
	70 -30	3.1	3.4	4.1	3.1
SrM -KNN	90 - 10	2.5	3.1	3.3	2.6
	80- 20	2.5	3.3	3.3	2.6
	70 -30	2.4	3.3	3.2	2.6

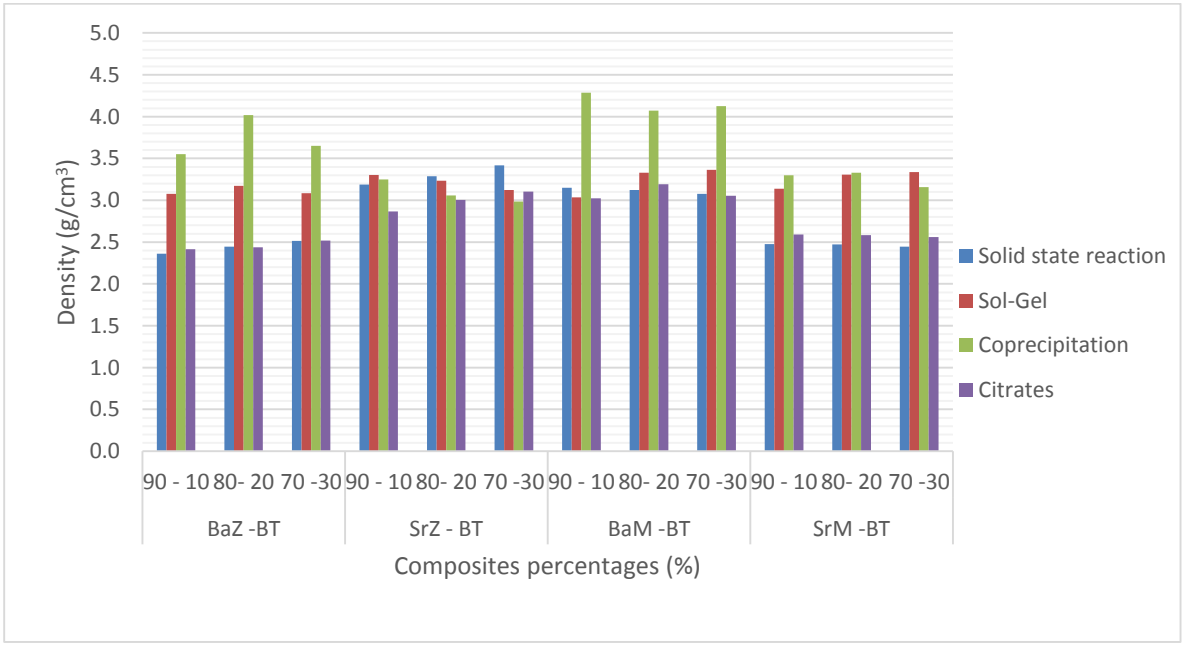

Figure 19: Density chart of KNN composites from uniaxial press.

Cold isotactic Press

In cold isotactic press, the density of the composites of KNN, table 8, is higher than uniaxial pressure. The lowest density is 2.6 g cm^{-3} and the highest is 4.4 g cm^{-3}. Comparing with the maximum theoretical density the KNN composites made by cold isotactic press have a density of 50% to 85%, lower than the BT composites with cold isotactic press.

Table 8: Density of KNN composites, cold isotactic press.

Hexaferrites + KNN					
Cold isotactic press (g/cm^3)					
	%	Solid state reaction	Sol-Gel	Coprecipitation	Citrates
BaZ - KNN	90 - 10	2.9	3.3	3.8	2.7
	80- 20	2.9	3.4	4.1	2.6
	70 -30	2.9	3.4	3.9	2.8
SrZ - KNN	90 - 10	3.5	3.5	3.4	3.1
	80- 20	3.3	3.6	3.6	3.3
	70 -30	3.5	3.4	3.3	3.2
BaM -KNN	90 - 10	3.5	3.5	4.3	3.6
	80- 20	3.4	3.6	4.4	3.5
	70 -30	3.4	3.6	4.2	3.5
SrM - KNN	90 - 10	3.0	3.4	3.2	2.9
	80- 20	3.0	3.4	3.5	2.9
	70 -30	3.0	3.2	3.2	2.8

The density of KNN composites with cold isotactic pressure have different densities with the different methods, and this can be visualized in the chart in figure 20.

The BaZ and the BaM composites have better density with the method of coprecipitation. In SrZ composites it is noticed that with different percentages of KNN the density changes from method to method - with 10% the better method is solid state reaction, for 20% the best method is sol-gel even though the difference to coprecipitation is not much, and with 30% the best result is from solid state reaction. In the SrM composites the best density was achieved with 20% with the method of coprecipitation.

The best result achieved in this procedure of pressing was BaM with 20% KNN, 4.4 g cm^{-3}.

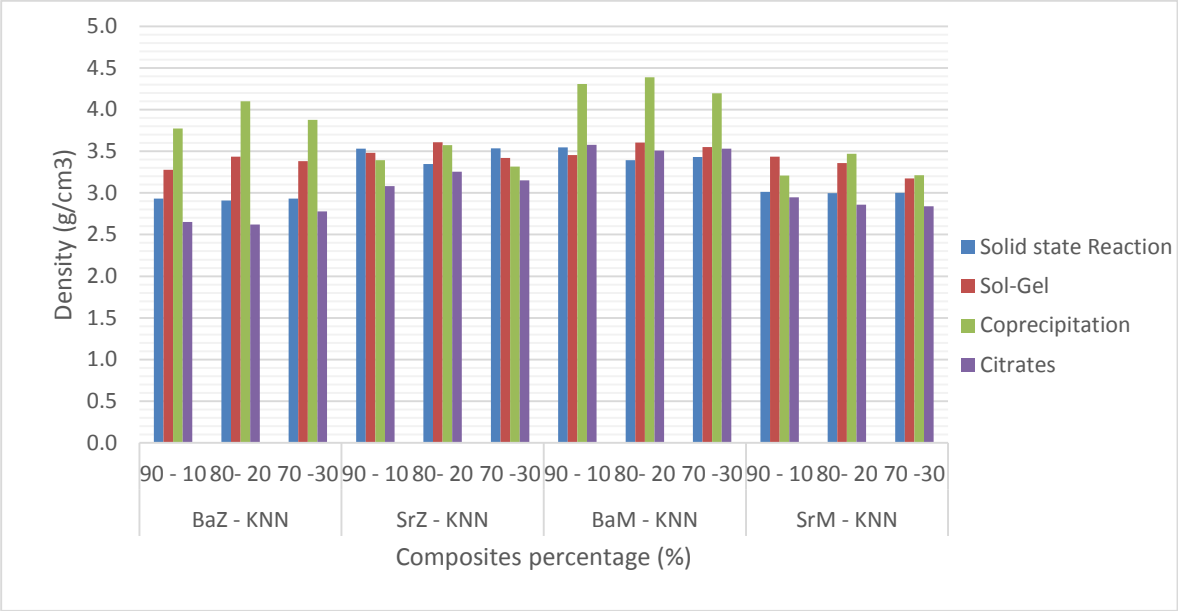

Figure 20: Density chart of KNN composites from isotactic press.

The results of the density of the sintered composites are below the theoretical density values as expected. In the literature some authors refer to the maximum practical density for such composites to be 90% of the maximum theoretical density [30], it is also important to keep in mind that these values were obtained using the geometric density, the materials could have some cracks of macroporosity, and only with the SEM images will be possible to see if the composites are compact. In this work, it is possible to say that cold isotactic press did improve the density of the materials, and different methods can provide different densities, the coprecipitation method in general did produce higher results due to the fine mixing of the compounds.

4.2.XRD

In the XRD measurements is only sowed the obtained phases from the hexaferrites and composites. Most of the measurements had showed the hematite phase, the hematite was not taken in consideration in the others previous results, it was intended to compared with the optimal theoretical results for this study, the phase of hematite formed.

4.2.1. Hexaferrites

The following figures below show the calcination of the different hexaferrites powders at different temperatures, and also the composites made by all the methods with different weight percentages. We used the Jade 9.0 software program from MDI to compare the standard patterns with the measured XRD patterns. No standard pattern has yet been published for SrZ, so it was necessary to calculate the pattern file [110].

In this analytical technique we used XRD equipment from Rigaku model DMax III/C with a radiation Cu K-alpha and wavelength 0.15418 nm. The scan velocity was 3°/min between the angles of 20° to 70°.

4.2.1.1. Solid state Reaction

The result obtained through XRD reveals a good formation of M-ferrites, although there is always the presence of some $\alpha-Fe_2O_3$, (hematite). One XRD was taken for each temperature of calcination for BaM and SrM, and for composites with $BaTiO_3$ the temperatures had a difference of 50°C between them. The first temperature of calcination was 1000 °C, the lowest temperature is not indicated in the XRD plots in the graphics in figures 21 and 22 because they didn't contain relevant data there was no formation of ferrites.

Analysing the graphics bellow, it can be seen that the formation of BaM starts at 1100 °C and with the increase of the temperature the iron oxide (III) (hematite) decreases. It was not necessary to increase the temperature because the BaM phases dominating, at ~ 90%, the phase formation of the SrM ferrite started at 1050 °C there was presence of $\alpha-Fe_2O_3$ in all calcinations temperature, whit the increase of the calcination temperature, the traces of hematite decreases, at 1200 °C there is mostly SrM ferrite.

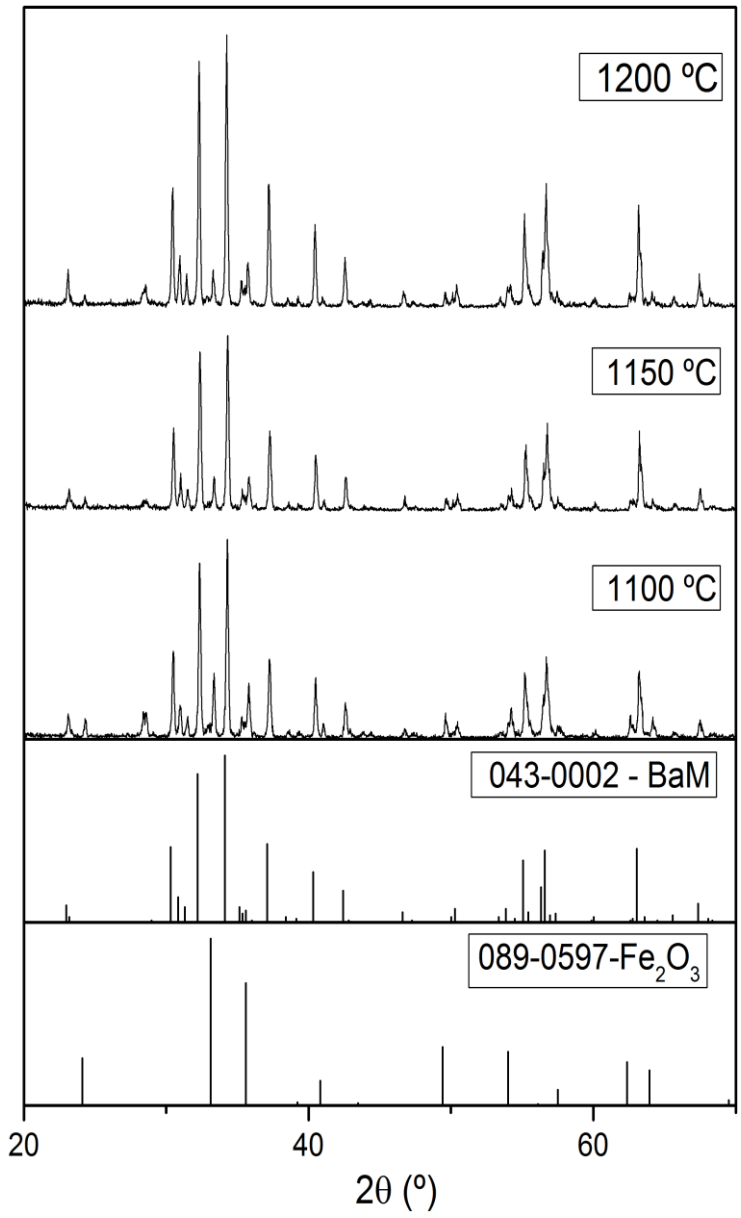

Figure 21: BaM hexaferrites, method of solid state reaction with different calcination temperatures.

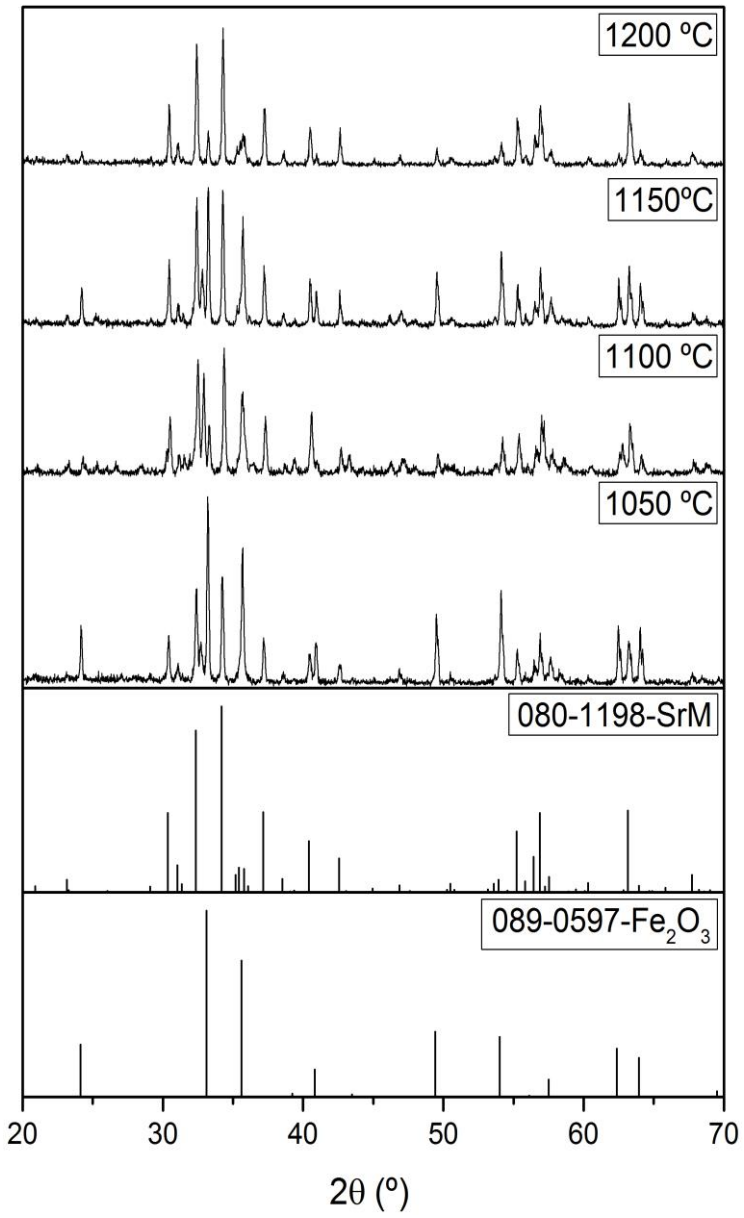

Figure 22: SrM hexaferrites, method of solid state reaction with different calcination temperatures.

In the Z-Ferrites the pure phases exists at higher temperatures but contains traces of other phases, the Y and M Ferrites. The BaZ ferrite, figure 23, decomposed to W type ferrite above 1250 °C, as is according to the literature, the phase of BaZ only appear in the temperature of 1250 °C, and contained the precursors phases, the peak of intensity of BaZ were low.

For SrZ ferrite, figure 24, the BaZ pattern was used due to the fact that the BaZ phase is very similar to the SrZ phase. The difference is a shift in the angles due to the difference of atomic radii of barium and strontium. A calculated pattern of SrZ was also used to calculate and confirm the diffraction angles, and is shown in fig. 25. In the Z-ferrites, the BaZ and SrZ phases were not

obtained as pure phases, but very strong peaks of Z-ferrites were detected, especially above 1150 °C.

The solid state reaction is a very good and simple method, and did produce good results in our experiments.

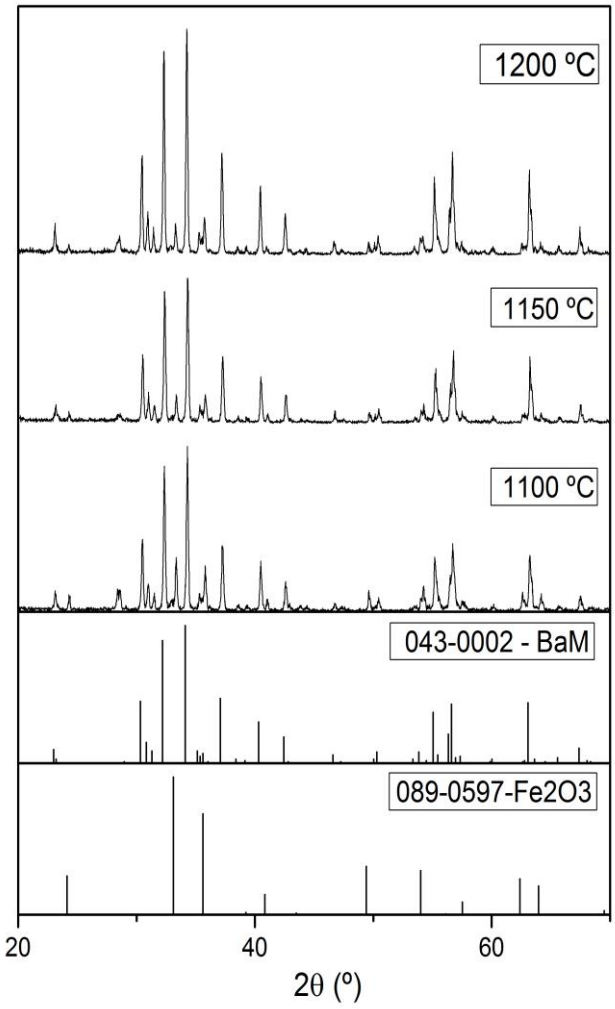

Figure 23: BaZ hexaferrites, method of solid state reaction with different calcination temperatures.

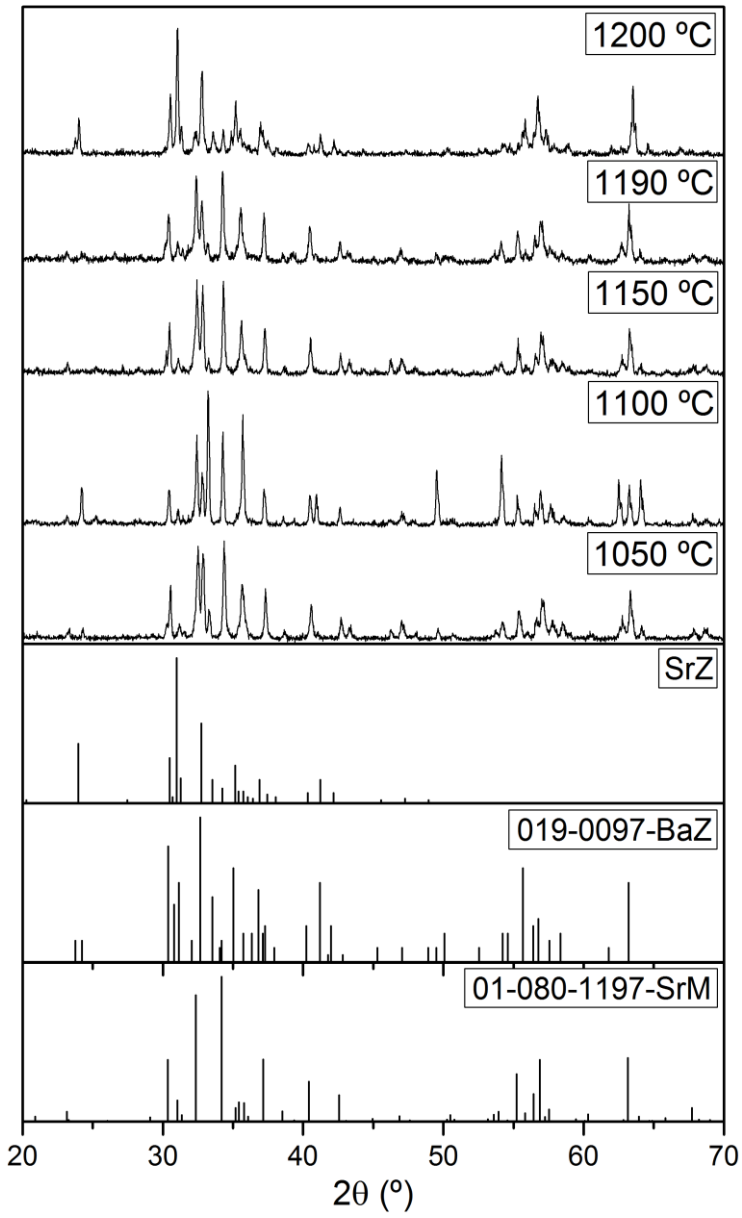

Figure 24: SrZ hexaferrites, method of solid state reaction with different calcination temperatures.

4.2.1.2. Coprecipitation

The calcination of M-ferrites by the method of coprecipitation resulted in a much greater amount of secondary phase, hematite (iron oxide (III)). Calcination temperatures were 1050 °C to 1200°C, in 50°C steps. Analysing the graphics in figure 25 and figure 26, there is high intensity peaks of hematite at all calcination temperatures, the highest was at the diffraction angle 33°.

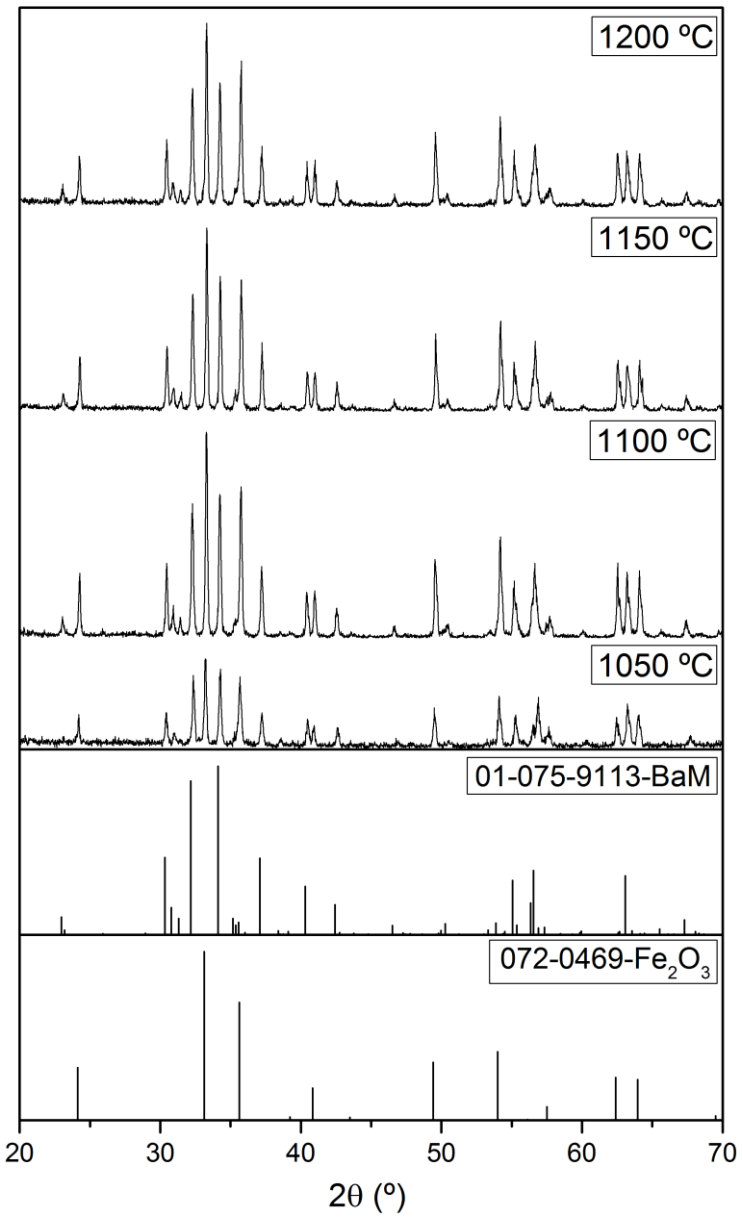

Figure 25: BaM hexaferrites, method of coprecipitation with different calcination temperatures.

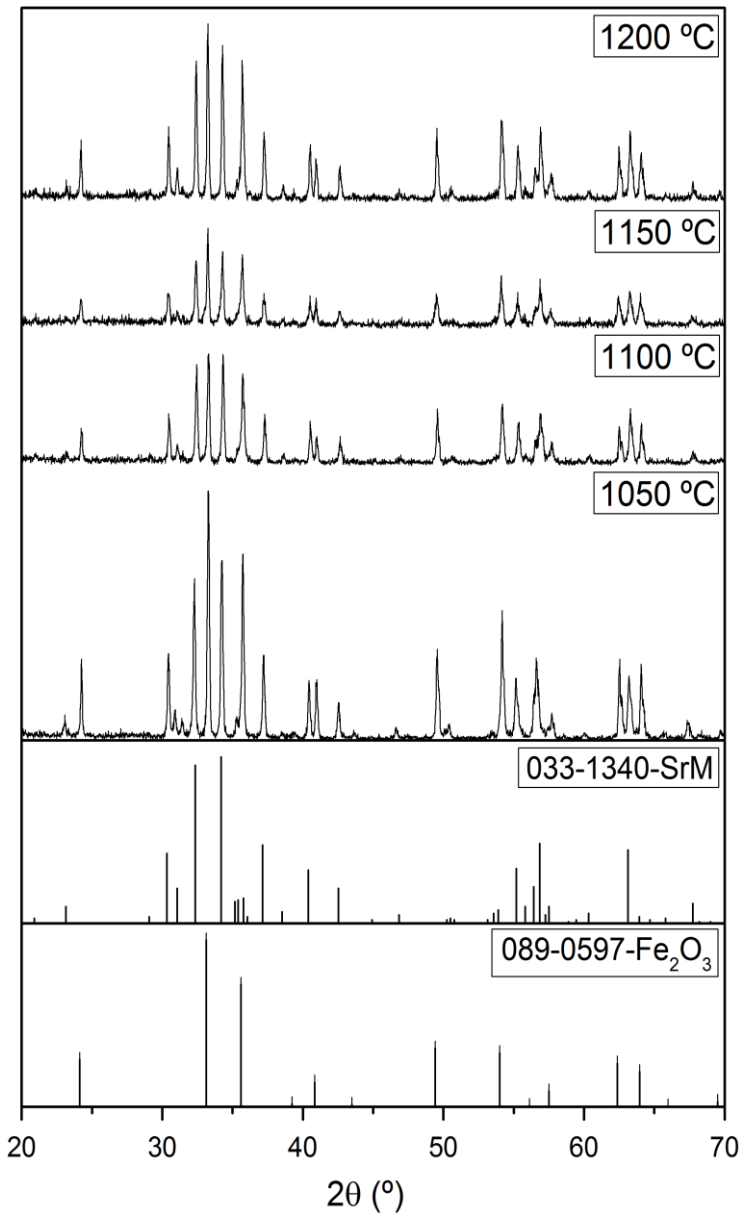

Figure 26: SrM hexaferrites, method of coprecipitation with different calcination temperatures.

In the Z-ferrites the XRD in figure 27 and figure 28, shows traces of M-phase and cobalt iron oxide, and hematite which many researchers claim to be a precursor to the formation of Z-Ferrite. There appears to be little change with temperature, and it is not clear from the XRD data that a Z phase is actually formed. In the XRD of SrZ is visible different amplitudes in the peaks at different

temperatures, at 1175 and 1190 °C is visible a very distinct phase of SrZ with high intensity peaks. The BaZ pattern 019-0097 and a calculated SrZ pattern were used to observe the SrZ phase.

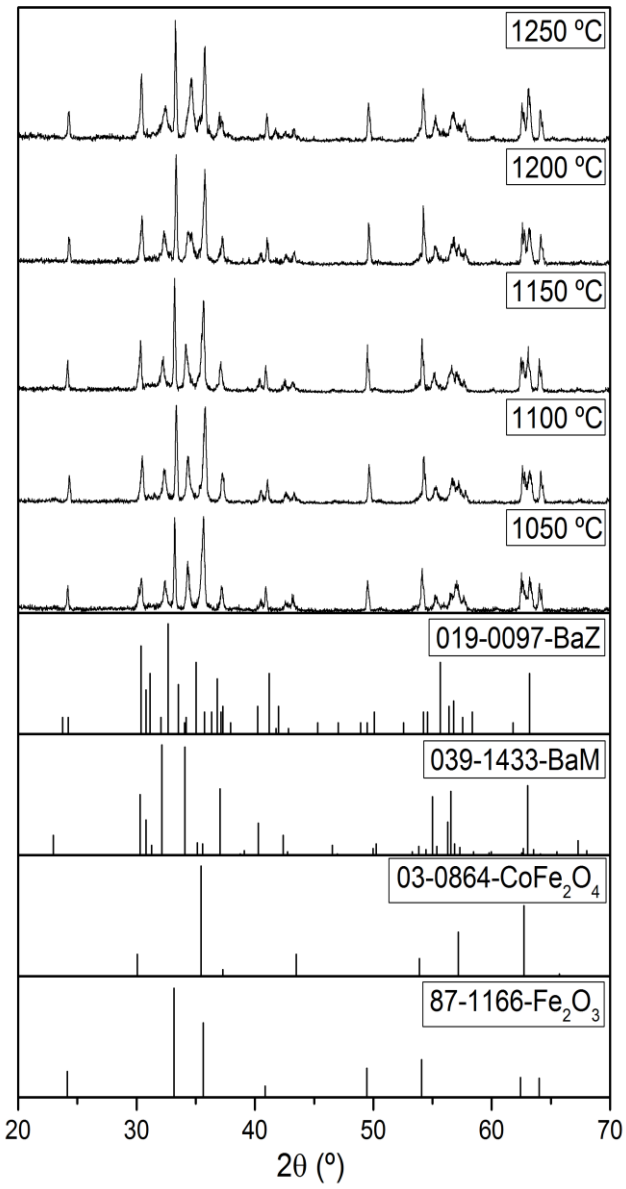

Figure 27: BaZ hexaferrites, method of coprecipitation with different calcination temperatures.

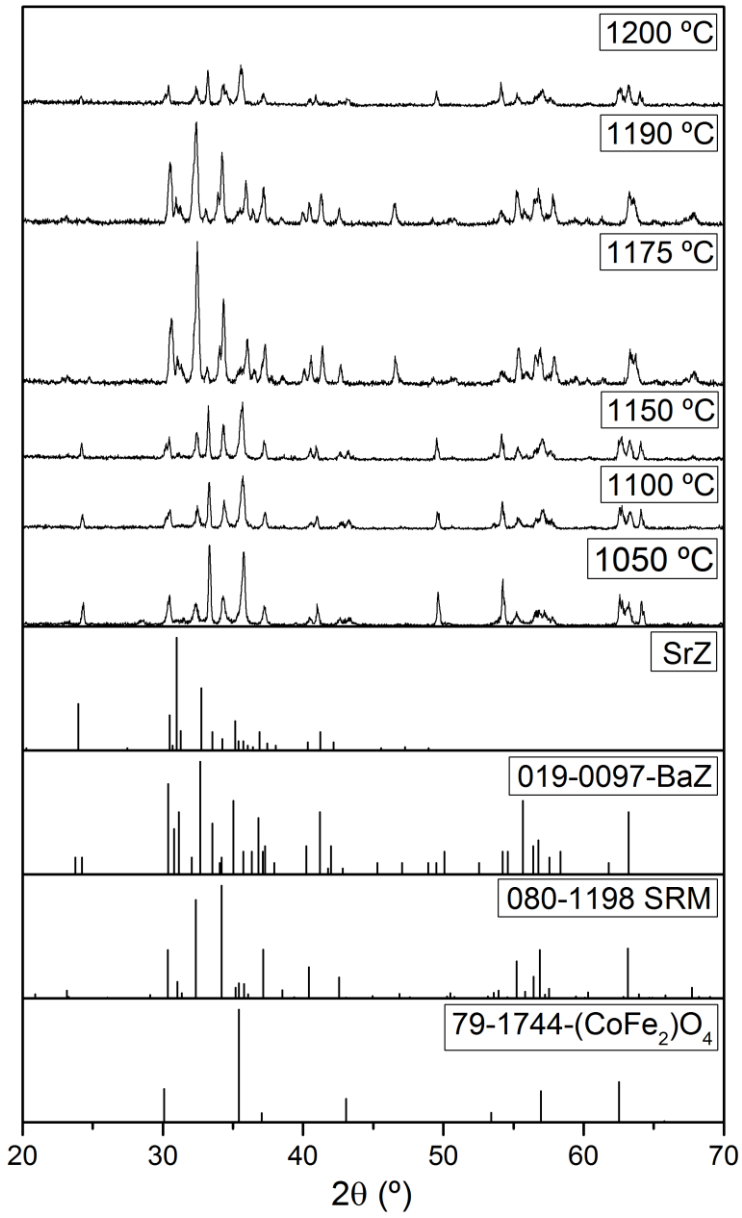

Figure 28: SrZ hexaferrites, method of coprecipitation with different calcination temperatures.

4.2.1.3. Citrates Synthesis

In the citrates synthesis methods we achieved the best results for M-Ferrite, figure 29 and figure 30, in the different calcinations temperatures we obtained pure single phases of M-Ferrites. The phases had the intensity peaks well defined at all temperatures.

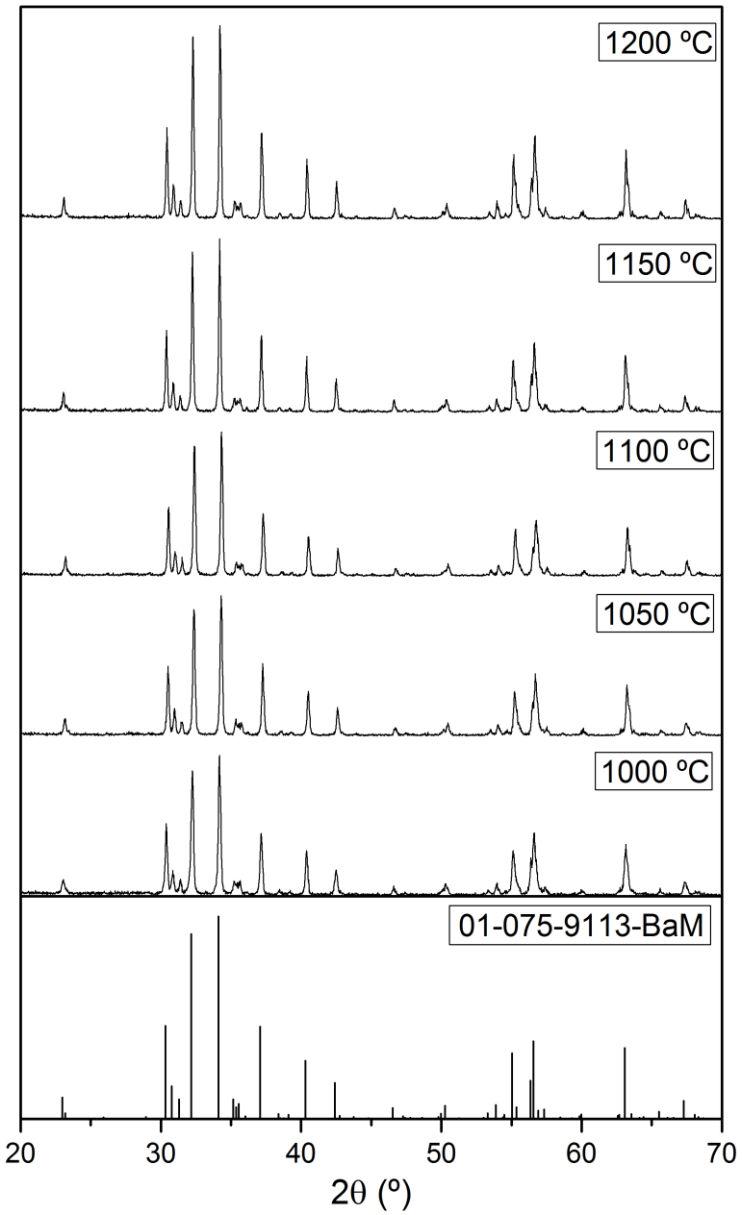

Figure 29: BaM hexaferrites, method of citrate synthesis with different calcination temperatures.

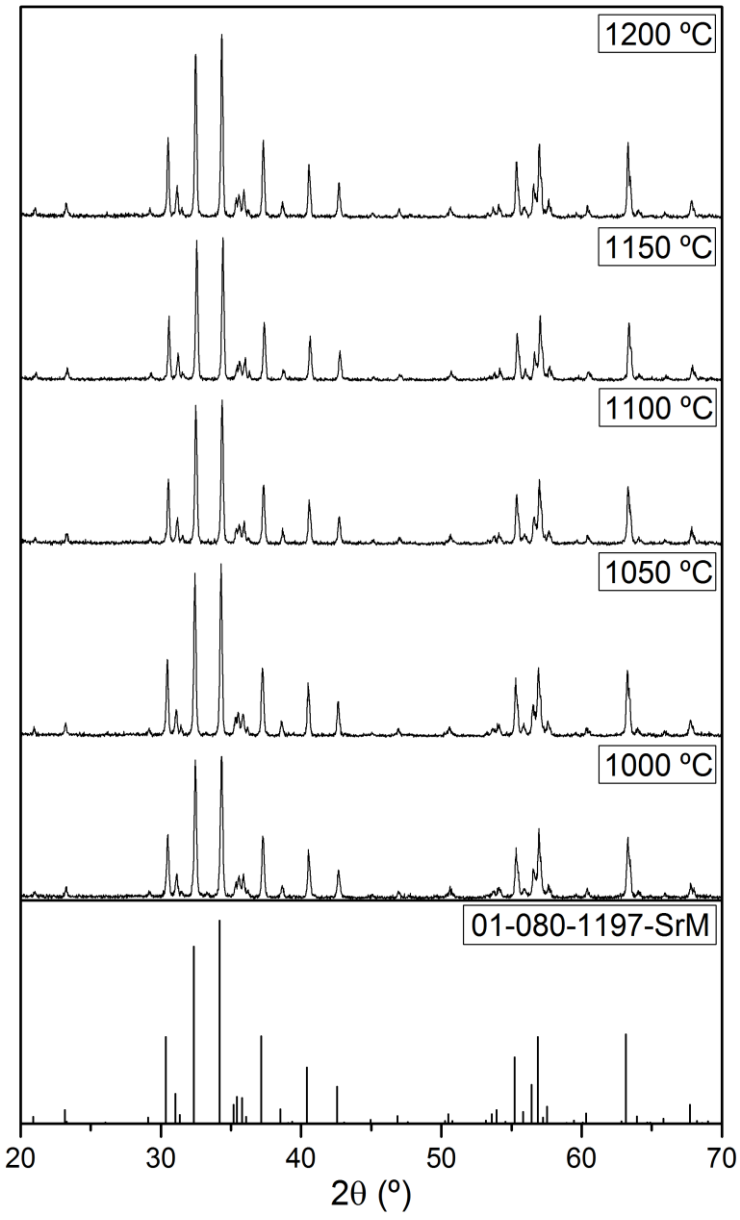

Figure 30: SrM hexaferrites, method of citrates synthesis with different calcination temperatures.

It was observed that in the XRD of Z-ferrites (figure 31 and figure 32), secondary phases occur in the BaZ-ferrite (figure 31), and there is presence of Co_2Y ferrite ($Ba_2Co_2Fe_{12}O_{22}$), and with the increase of the temperature the secondary phase decreases but doesn't disappear. In the SrZ ferrite figure 32, there is no presence of Y type ferrite, and is still unknown if the Co_2Y phase is required as a precursor of the SrZ ferrite, but a secondary phase is also present of M-ferrite phase,

SrM. Comparing with the BaZ pattern, it is noticed that at the temperature of 1190 °C the peaks of SrZ ferrite are more detailed, and there is clearly formation of SrZ ferrite.

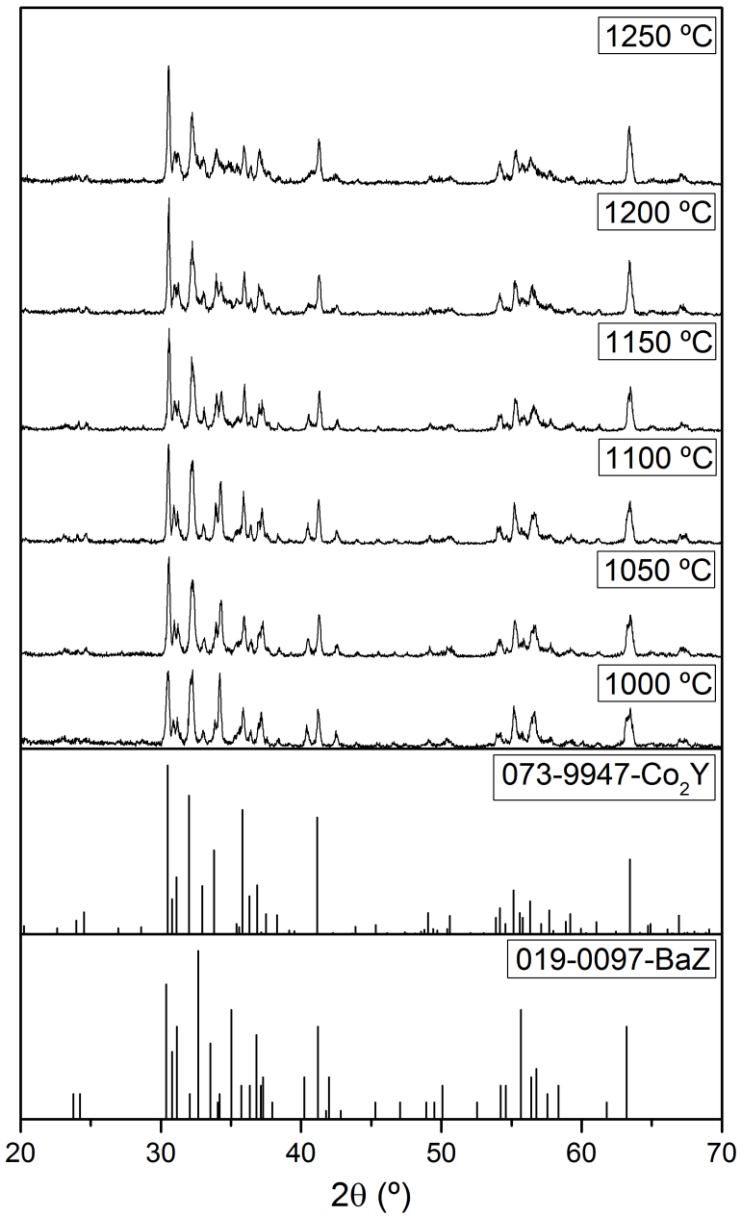

Figure 31: BaZ hexaferrites, method of citrates synthesis with different calcination temperatures.

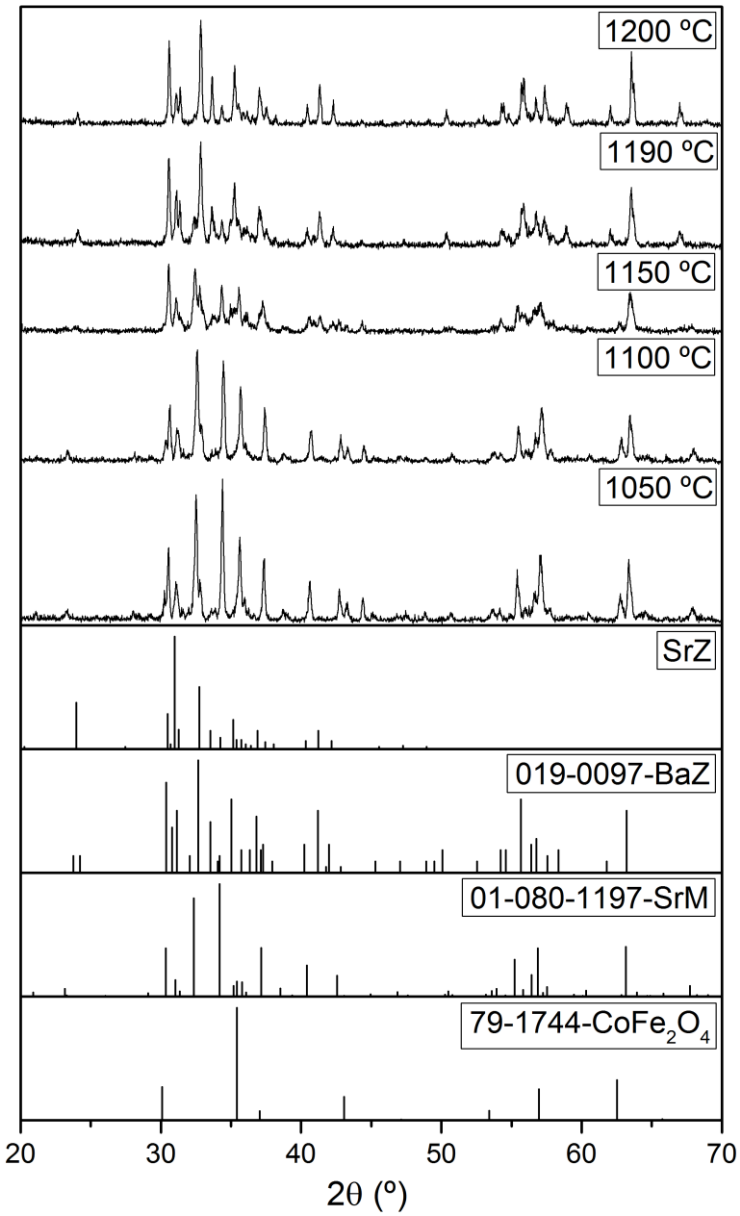

Figure 32: SrZ hexaferrites, method of citrates with different calcination temperatures.

4.2.1.4. Sol-gel

The XRD of sol-gel shows that the M-ferrites (figure 33 and figure 34) contain two phases, the principal phases BaM or SrM, and a secondary phase in both M-ferrites of hematite. In this case the peak of the secondary phase is more intense than the principal phase at all calcination temperatures.

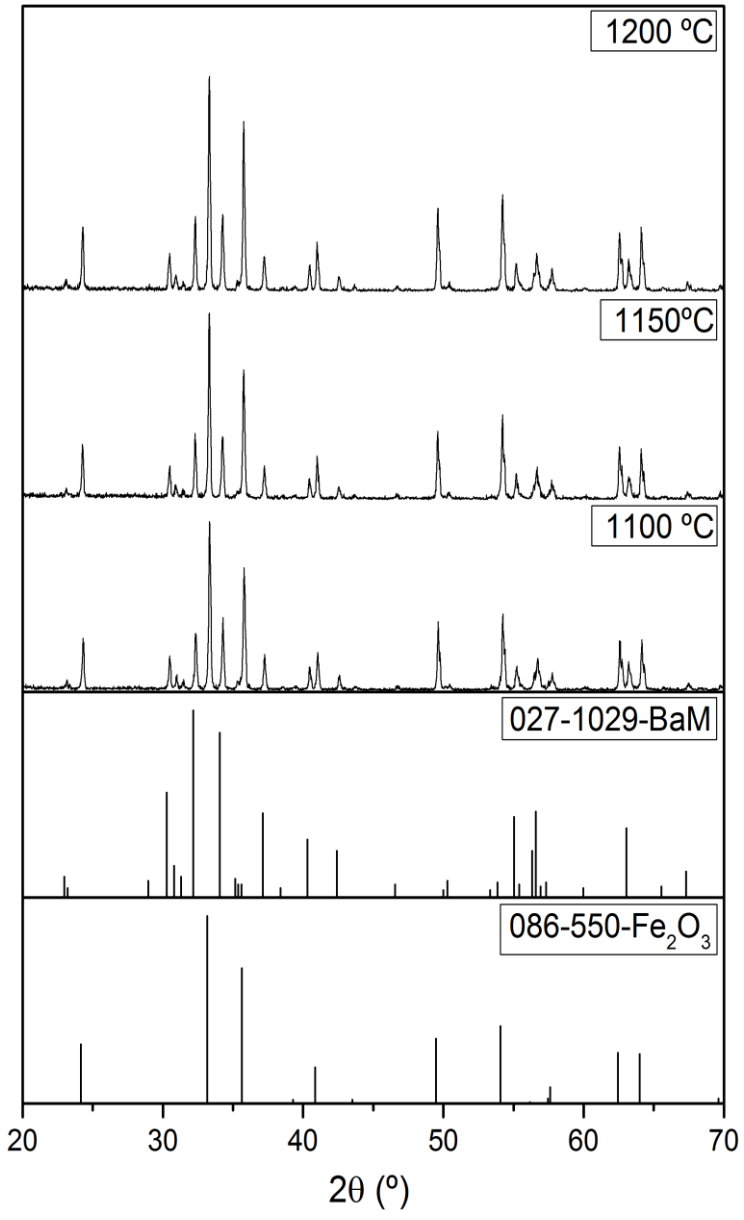

Figure 33: BaM hexaferrites, method of sol-gel with different calcination temperatures.

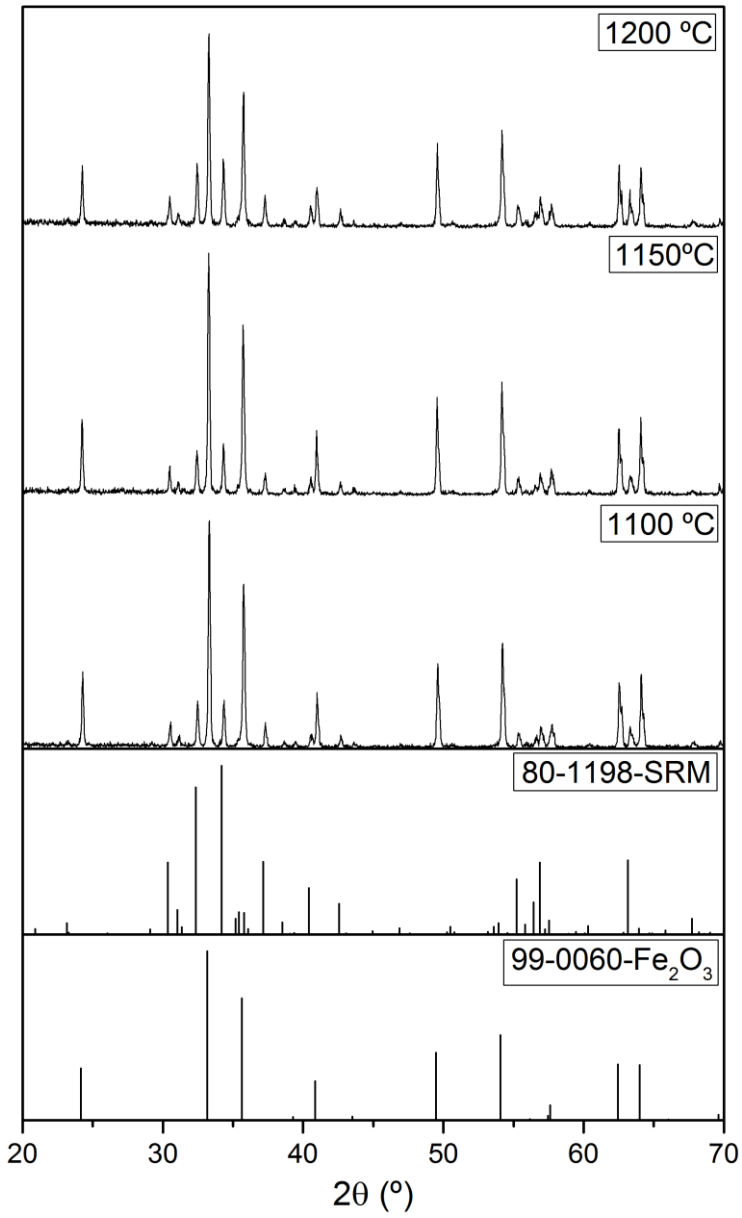

Figure 34: SrM hexaferrites, method of sol-gel with different calcination temperatures.

In the Z-Ferrites (figure 35 and figure 36) more secondary phases other than M-Ferrites were visible in the case of BaZ, and the formation of the phase only occurs at 1250 °C. The cobalt ferrite phase ($CoFe_2O_4$) is considered to be a precursor of the BaZ ferrite, and also the Co_2Y already mentioned above, yet still there are traces of both phases at 1250 °C.

The SrZ ferrite phase had formed at the temperatures of 1190 °C and 1200 °C, and with the XRD is possible to visualize that it contains secondary phases such as hematite and also contains the M-ferrite and the cobalt ferrite phase. This method was not the most effective to get good results.

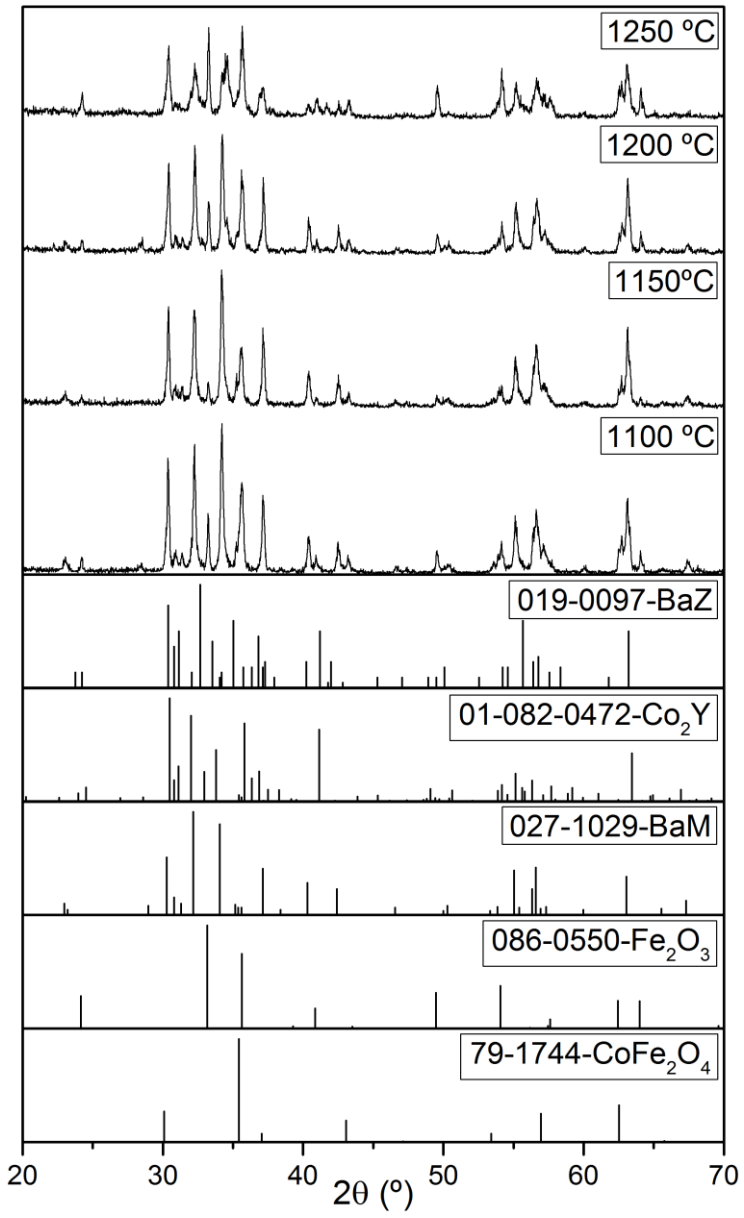

Figure 35: BaZ hexaferrites, method of sol-gel with different calcination temperatures.

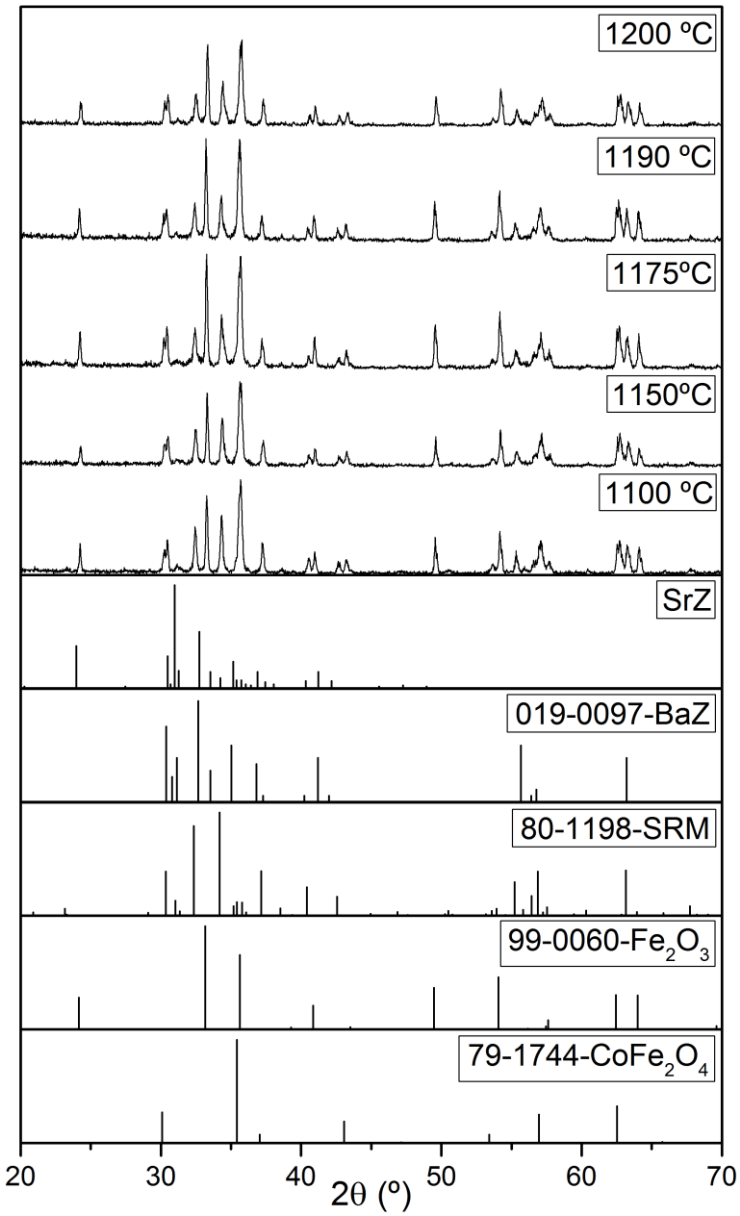

Figure 36: SrZ hexaferrites, method of sol-gel with different calcination temperatures.

In the table 9, is summarized the phases present in the hexaferrites, the phases in bold are the primary phases with high insensitive peaks and the phases underline are the precursor phases.

Table 9: summary of the phases present in the hexaferrites.

		Synthesis methods				
		Soli state reaction	Coprecipitation	Sol-gel	Citrates	
Powder	BaM	**BaM**, Hematite	**BaM**, Hematite	**BaM**, Hematite	BaM	Phases
	SrM	**SrM**, Hematite	**SrM**, Hematite	**SrM**, Hematite	SrM	
	BaZ	$\underline{Co_2Y}$ (Y- Ferrite), BAM, BaZ	Hematite, $\underline{CoFe_2O_4}$, BaM, BaZ	$\underline{Co_2Y}$, BaM, Hematite, $\underline{CoFe_2O_4}$	$\underline{Co_2Y}$, BaZ	
	SrZ	SrM, SrZ	$\underline{CoFe_2O_4}$, SrM, SrZ	SrZ, SrM, Hematite, $\underline{CoFe_2O_4}$	$\underline{CoFe_2O_4}$, SrM, SrZ	

4.2.2. Composites of hexaferrites and $BaTiO_3$

We made XRD of the pellets of the composites of hexaferrites and barium titanate to confirm the presence of both phases in all weight percentage and the different methods.

4.2.2.1. Solid state reaction

The XRD of the composite of BaM and barium titanate, figure 37, shows the presence of both phases and some secondary phases, there was a diffusion of atoms between the two phases originating a formation of $BaFeO_3$ and $BaFeO_{2.9}$, with the decrease of the phase of barium titanate.

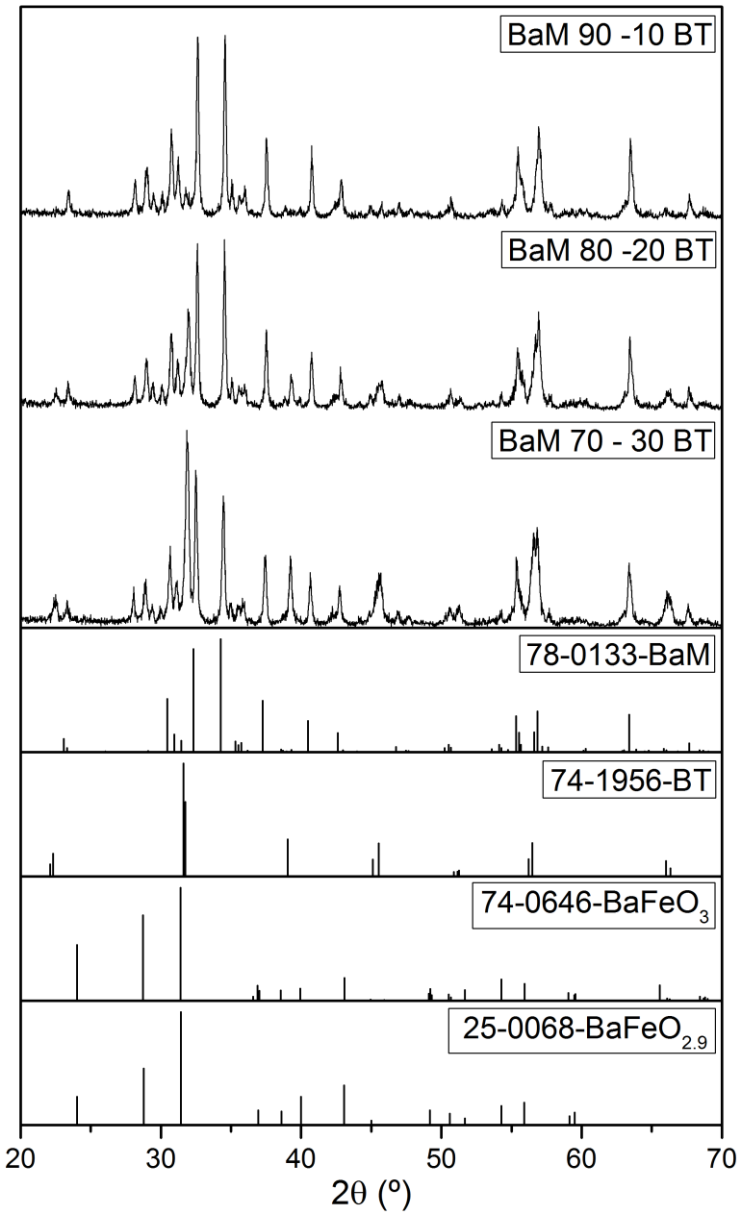

Figure 37: Sintered BaM-BT composites with different weight percentage, produced by solid state reaction method.

In the composites of SrM-BT, figure 38, a formation of a secondary phase did occur, $SrTiO_3$ phase. This phase had very high intensity peaks, a possible explication for the formation of this phase is that $BaTiO_3$ and SrM exchange atoms, the BT phase had decreased in the composites. $SrTiO_3$ is a paraelectric material that exhibits piezoelectric characteristics only at a very low temperatures, and it shows a very low piezoelectricity at room temperature.

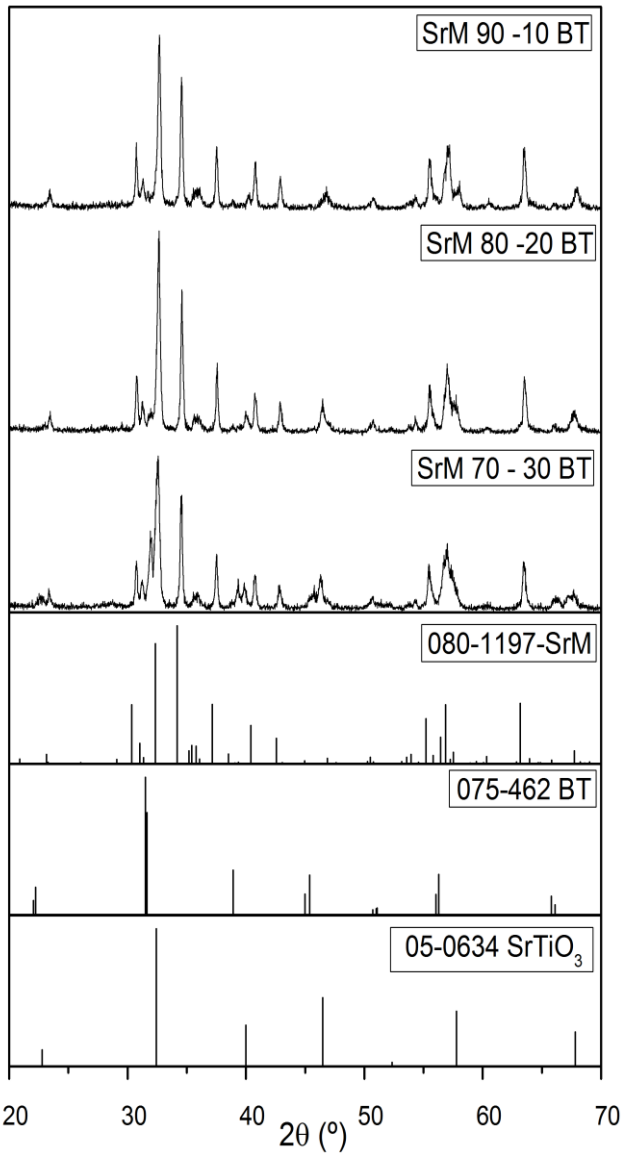

Figure 38: Sintered SrM-BT composites with different weight percentage produced by solid state reaction method.

The XRD of the composites of BaZ-BT in figure 39, shows that both phases, BaZ and BT, are distinct and with high intensity in all composites with different weight percentages, but it also shows a remaining phase of BaM in all weight percentages.

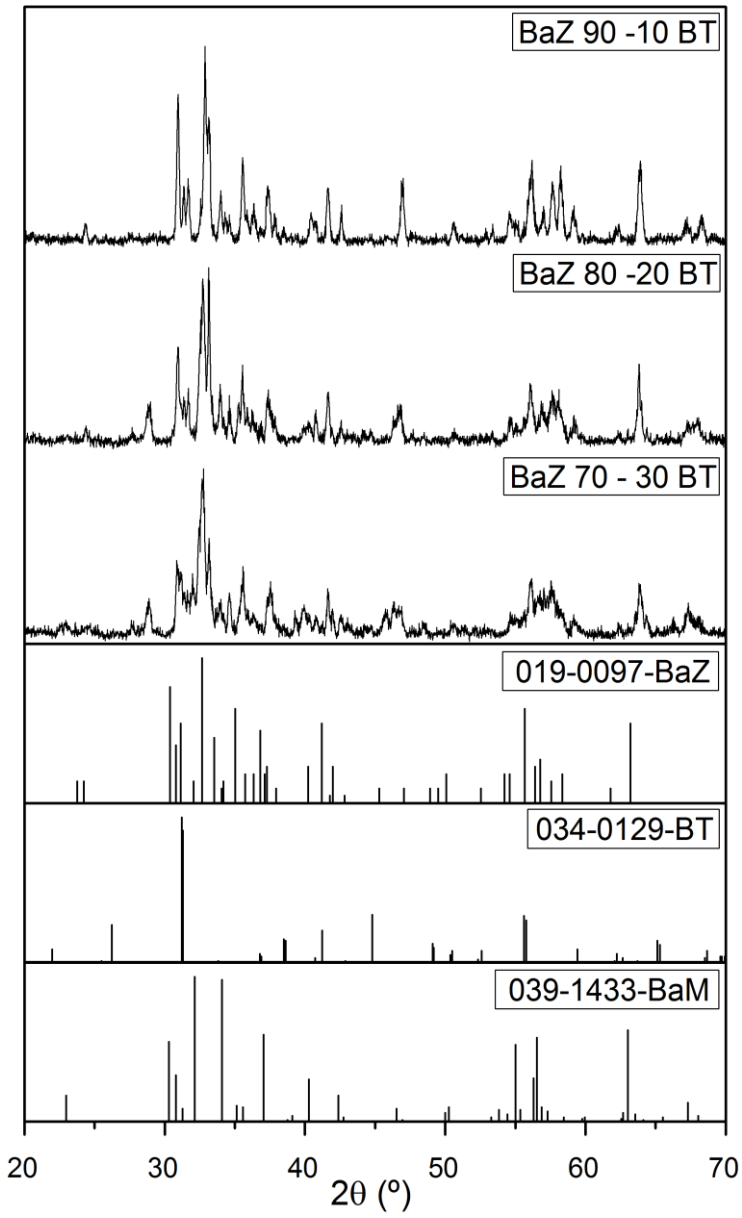

Figure 39: Sintered BaZ-BT composites with different weight percentage produced by solid state reaction method.

The XRD of the composite of SrZ-BT, figure 40, had similar results to the BaZ-BT composites in this case the SrM phase did remain, and the other secondary phases present in SrZ powder seem to disappear.

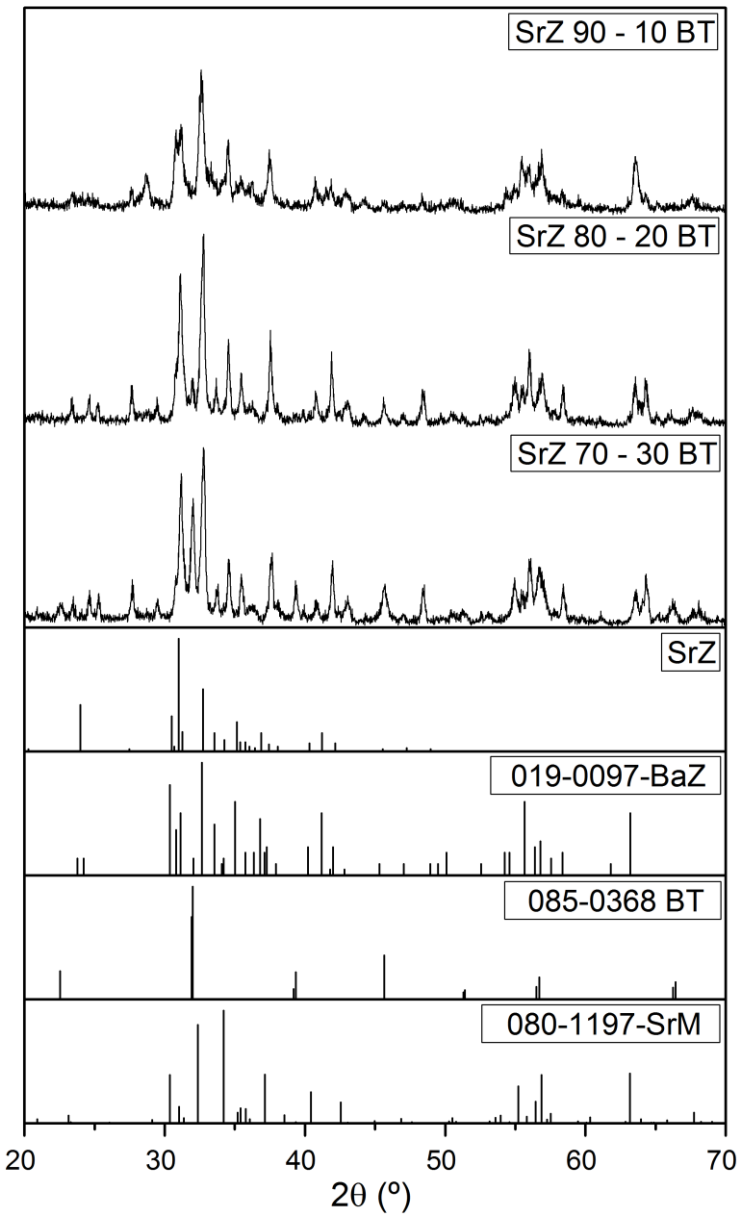

Figure 40: Sintered SrZ-BT composites with different weight percentage produced by solid state reaction method.

4.2.2.2. Coprecipitation

In figure 41, the XRD analysis shows that in the composites of BaM-BT with different weight percentage, has only present the two main phases BaM and BT, the peaks are very distinct, and there was not a shift in the angle of diffraction.

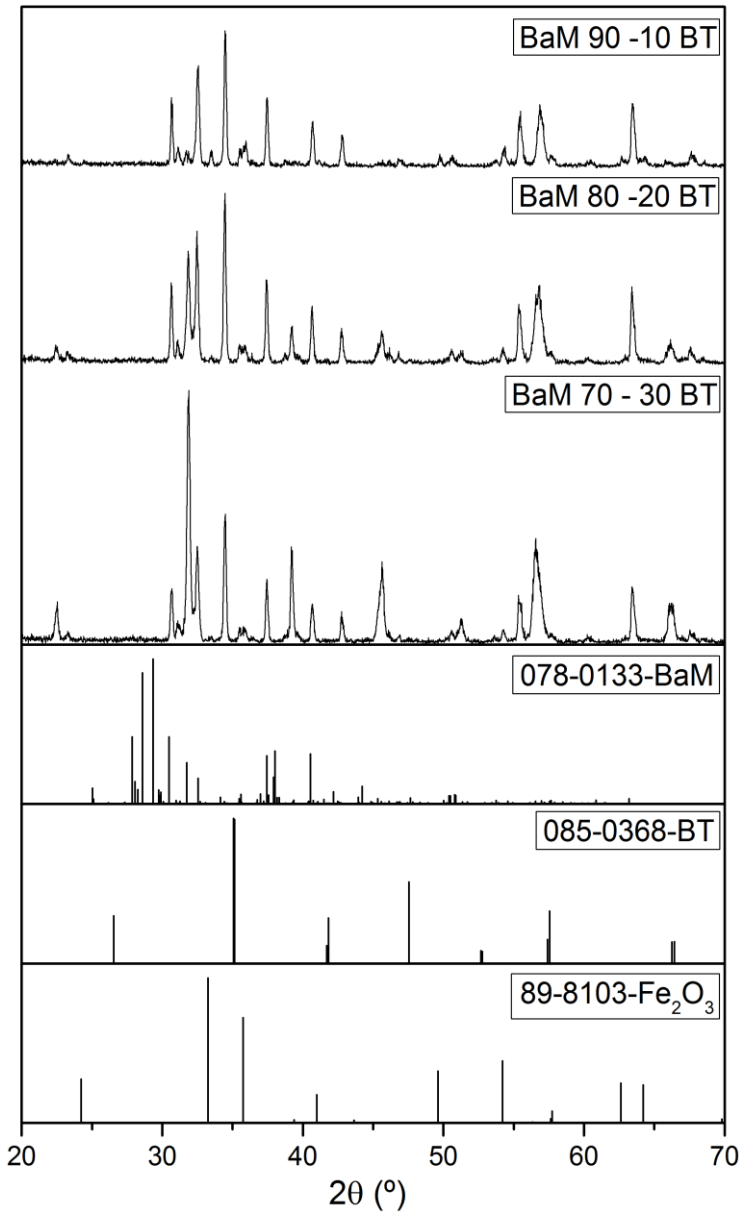

Figure 41: Sintered BaM-BT composites with different weight percentage, produced by coprecipitation method.

In the XRD of SrM composites there is a presence of a low secondary phase of hematite, with SrM peaks of high intensity (figure 42). The $BaTiO_3$ peak around 31° has dislocated to the right by about 1°, indicating the probably diffusion of Sr^{2+} into the $BaTiO_3$ lattice.

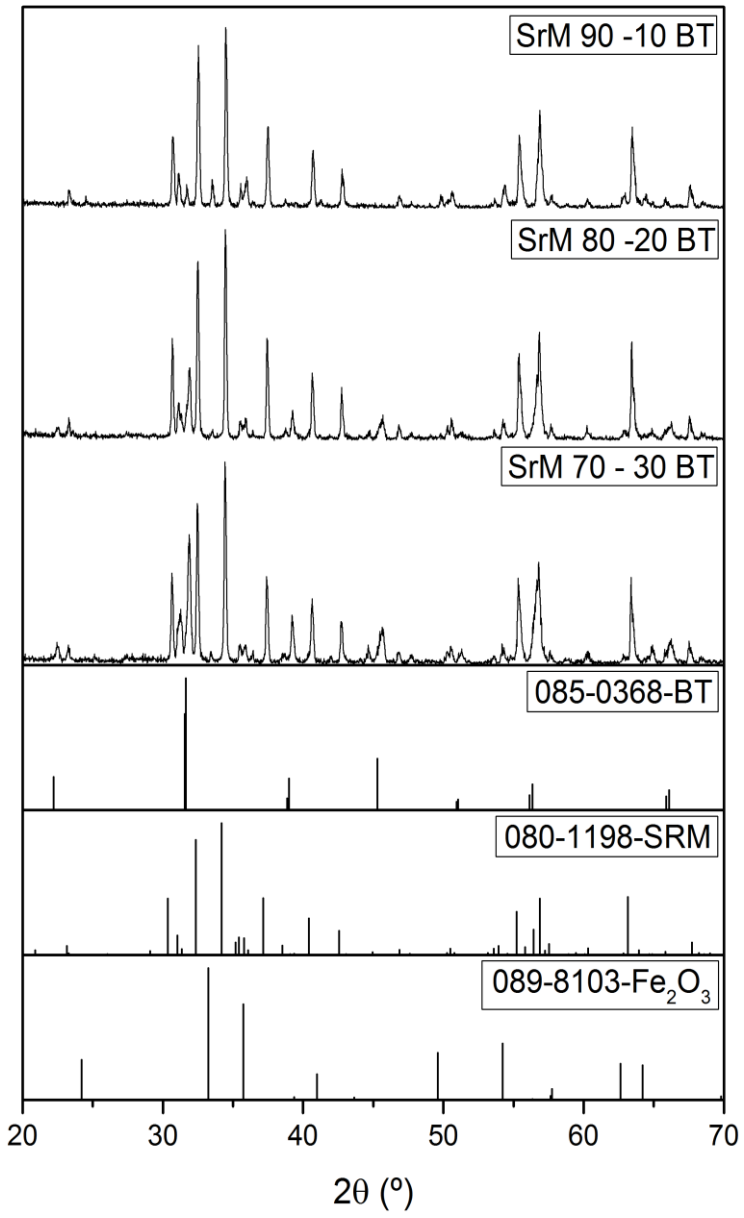

Figure 42: Sintered SrM-BT composites with different weight percentage, produced by coprecipitation method.

The XRD of BaZ composites shows there is small quantity of BaZ phase, the M and Y phases have greater intensities, and also there is some trace of hematite (figure 43). The coprecipitation method didn't produce a well formed phase of $BaTiO_3$ and BaZ. The composite with 80% of BaZ and 20% of BT only shows an M-ferrite phase and $BaTiO_3$.

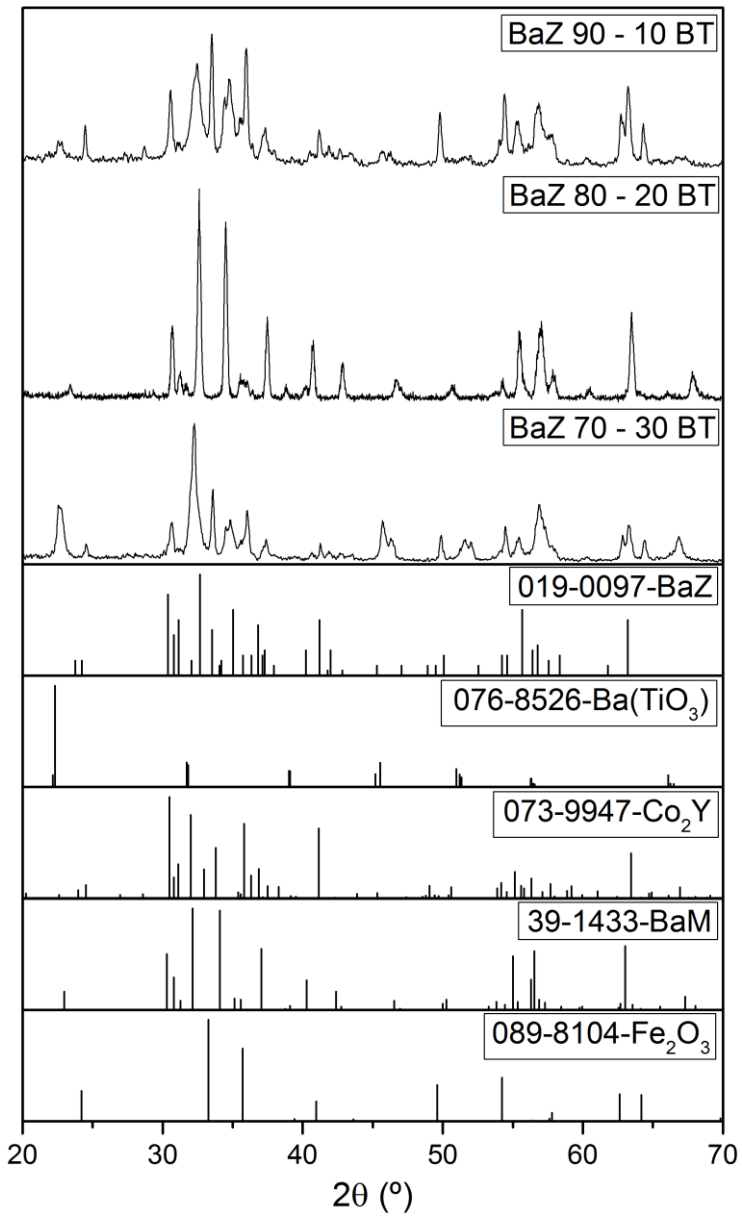

Figure 43: Sintered BaZ-BT composites with different weight percentage, produced by coprecipitation method.

The XRD of SrZ also shows a formation of secondary phases (figure 44), there was a diffusion between atoms of Cobalt, Barium and Strontium forming a new phase $Ba(Fe_{10.3}Co_{0.85}Ti_{0.95}O_{19})$ that is also an hexaferrite, but still there is some SrZ phase and $BaTiO_3$ phase without diffusion between then.

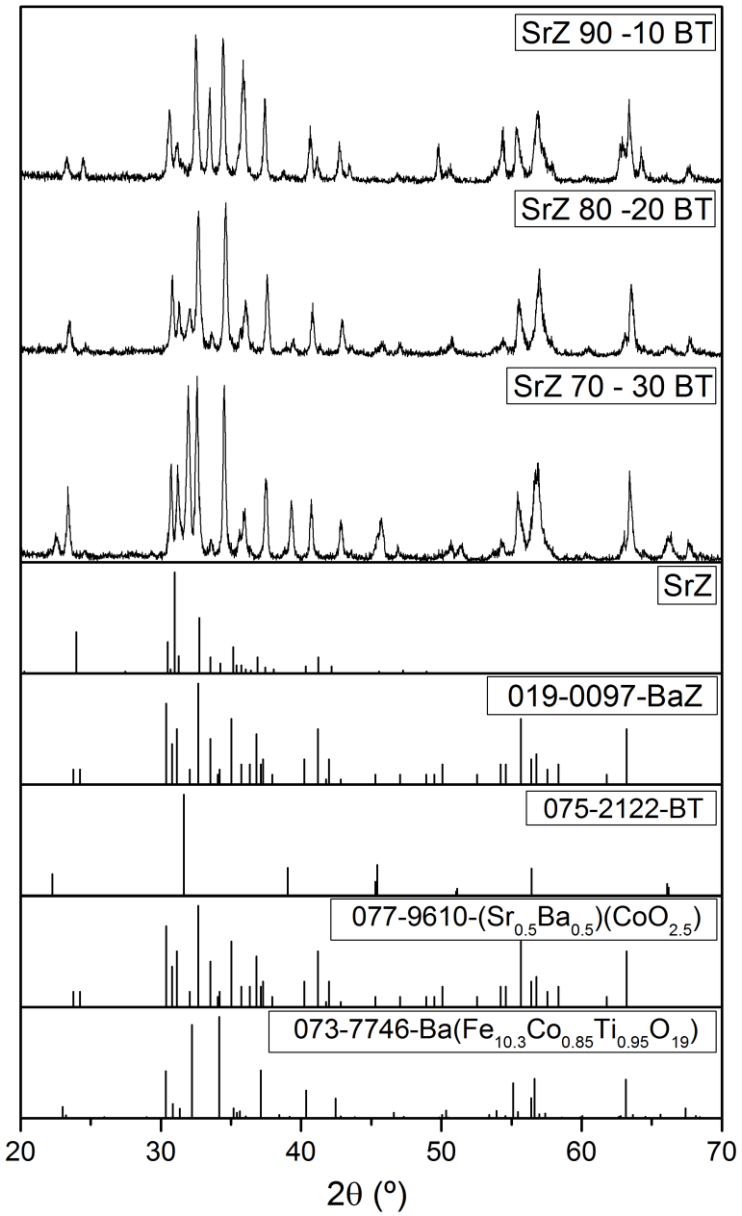

Figure 44: Sintered SrZ-BT composites with different weight percentage, produced by coprecipitation method.

This method didn't produce a pure phases in most of the composites, and only the BaM composites didn't show secondary phases.

4.2.2.3. Citrates

The XRD of BaM composites from the citrates synthesis method shows only two phases, BaM and $BaTiO_3$ (figure 45), the peaks of phases are distinct and no secondary phases present, at all weight percentages.

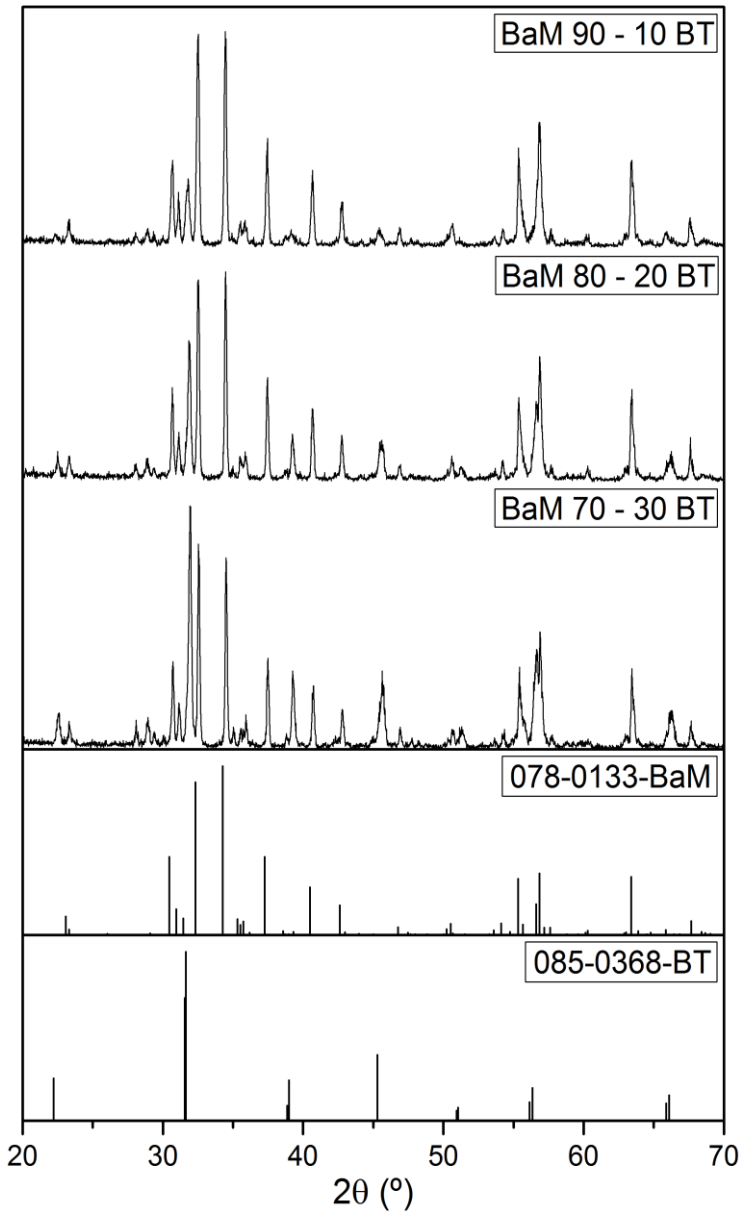

Figure 45: Sintered BaM-BT composites with different weight percentage, produced by citrates synthesis method.

In the XRD of SrM composites, shows that during the sintering a phase of $SrTiO_3$ was formed. This phase has a greater intensity than $BaTiO_3$ (figure 46). $SrTiO_3$ is a material that has very poor piezoelectric measurements, and this phase also appears in SrZ composites with $BaTiO_3$ (figure 48). Although there is still visible a small phase of $BaTiO_3$ on the composite, the $SrTiO_3$ seems to occur more easily, suggestion that the formation of $SrTiO_3$ is preferred to that of $BaTiO_3$ in these composites.

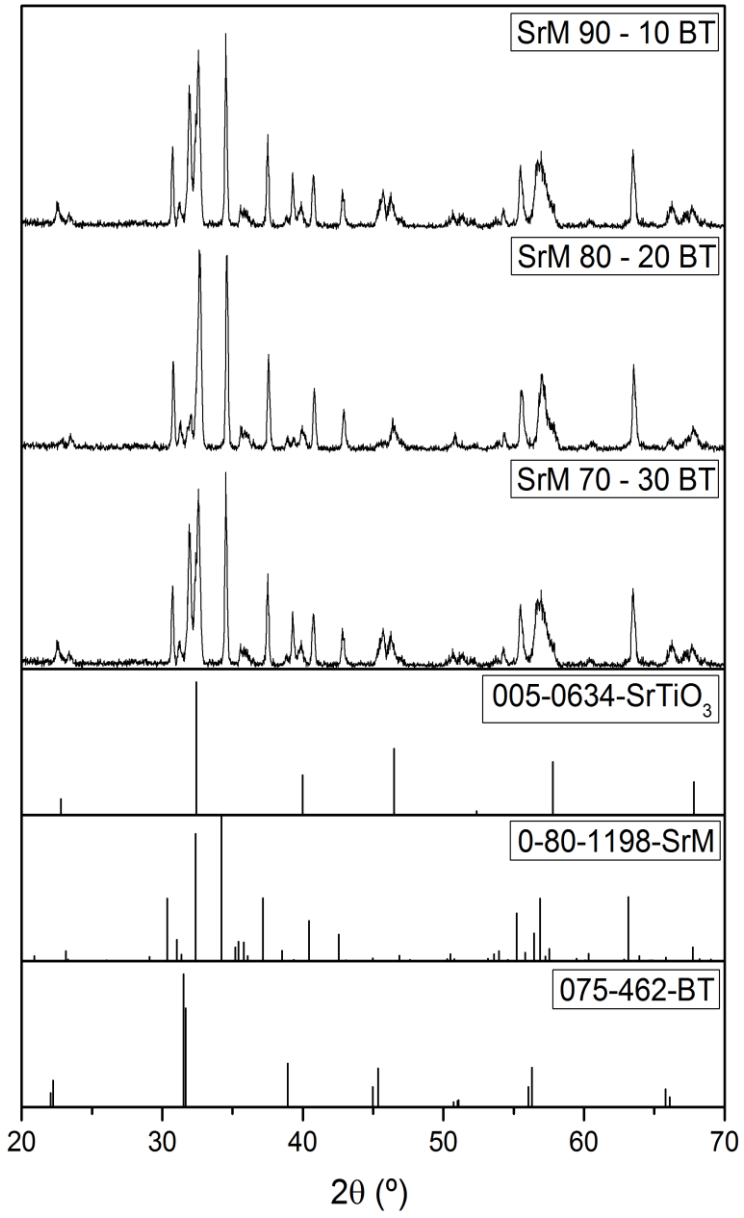

Figure 46: Sintered SrM-BT composites with different weight percentage, produced by citrates synthesis method.

In the XRD of BaZ, there a remains trace of Co_2Y and the phases BaZ and $BaTiO_3$ (figure 47), and the phase of Co_2Y decreases with the increasing of the $BaTiO_3$ phase.

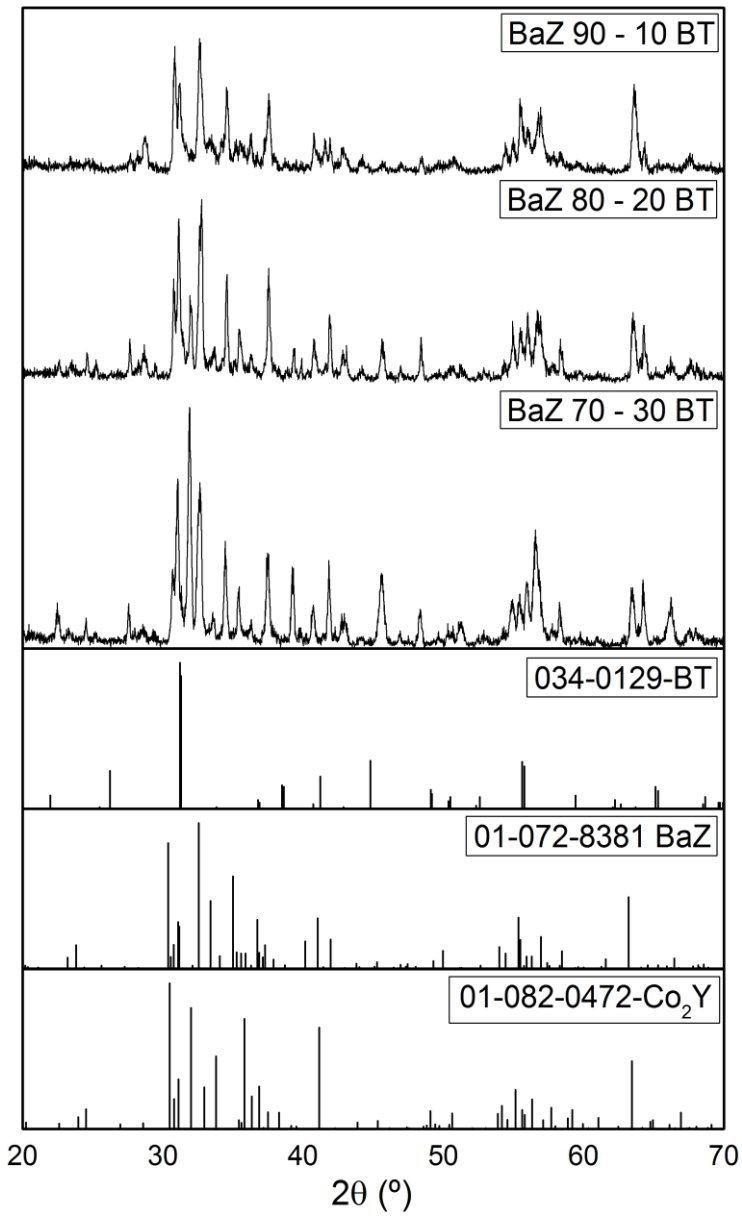

Figure 47: Sintered BaZ-BT composites with different weight percentage, produced by citrates synthesis method.

As already describe above for SrM in figure 46, the sintering of the SrZ composites with $BaTiO_3$ produced a secondary phase of $SrTiO_3$ with insensitive peaks, the BT phase is notice with low intensities peaks, SrZ phase did form and increased intensity with the decrease of ferroelectric phase, BT.

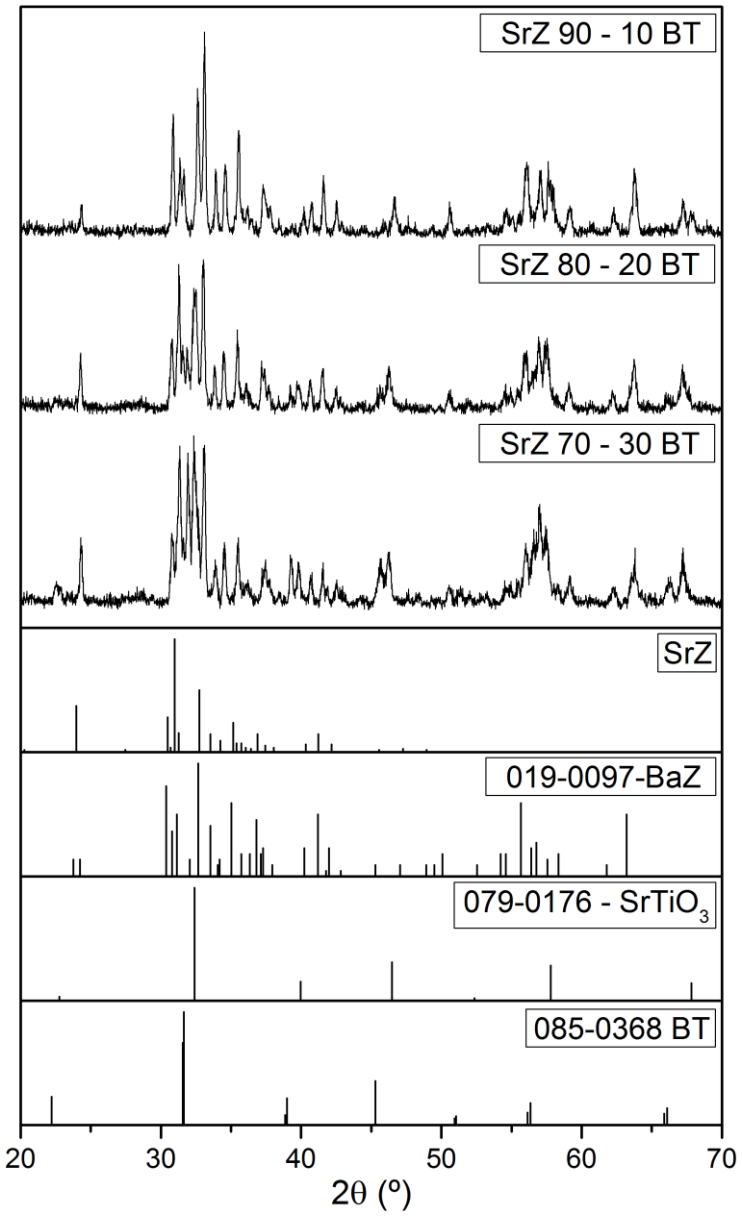

Figure 48: Sintered SrZ-BT composites with different weight percentage, produced by citrates synthesis method.

4.2.2.4. Sol-Gel

The sintering of the composites with BT made by the sol-gel method. In the case of M-ferrites (figure 49 and 50). The result shows the phases of BaM and BT with intensive peaks, but there is still the presence of hematite in the composites. However, in the case of BaM 90 – 10 BT its shows that the trace of hematite, less than the other composites made by the same method, and a massive peaks of BT, the sample contained more BT than expected, this explains the low phase of hematite is possible should be expected 90% of ferrite, to best clarify magnetic measurements will be done.

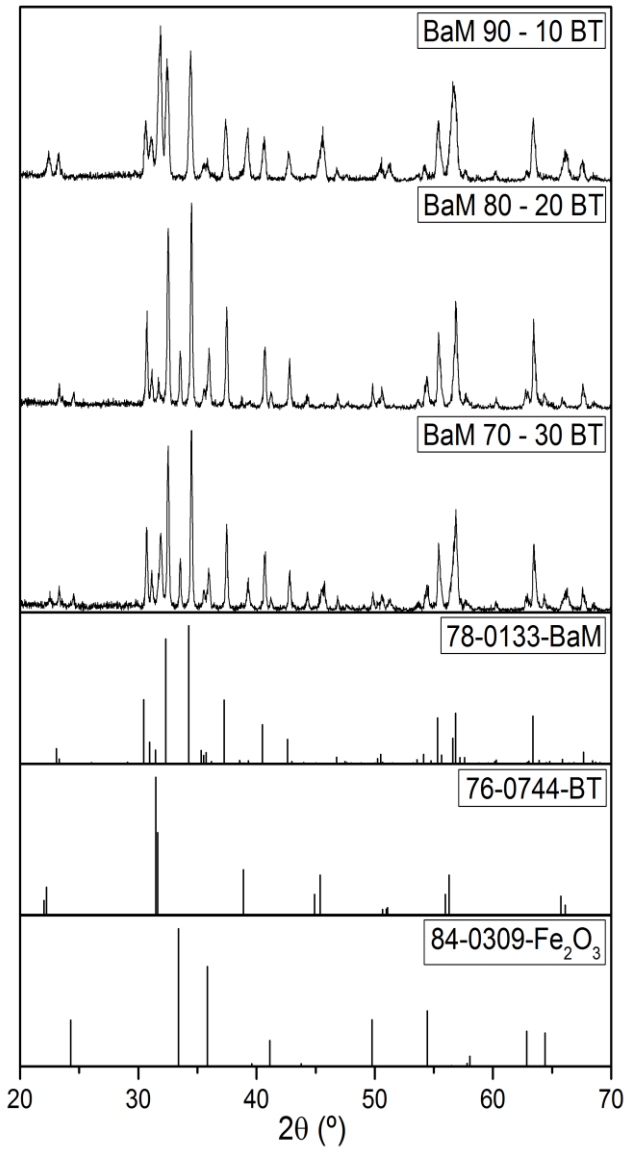

Figure 49: Sintered BaM-BT composites with different weight percentage, produced by sol-gel method.

The SrM-BT composites formed high intensive secondary phases hematite and strontium titanate oxide tetragonal structure (I4/mmm) there was presence of barium titanate but very low intensities peaks almost undetected by the XRD, the hematite phase is low in the composition of SrM 90 – 10 BT (figure 50), the others compositions SrM 80 - 20 BT and SrM 70 – 30 BT had sowed higher hematite intensities peaks.

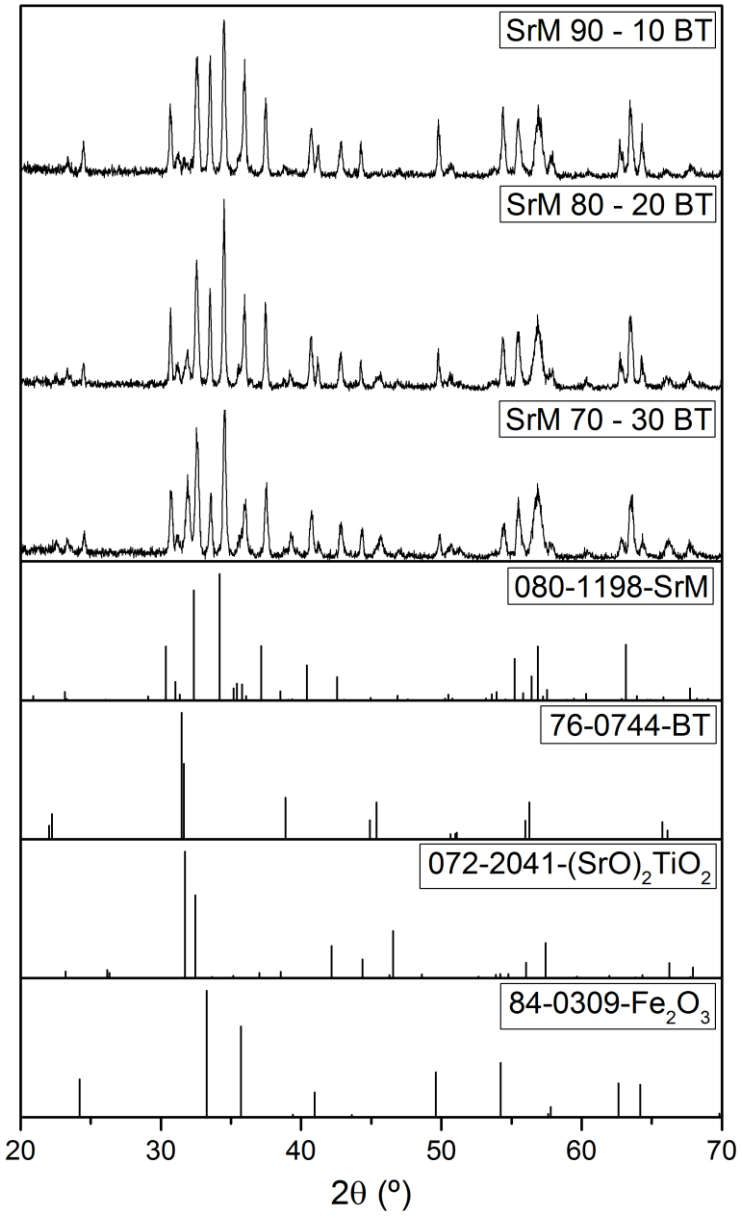

Figure 50: Sintered SrM-BT composites with different weight percentage, produced by sol-gel method.

In the cases of Z-ferrites the results were not very promising at all. The BaZ composite with BT (figure 51) showed there were secondary phases that had very strong intensity peaks, compromising the formation of BaZ ferrite. The XRD identification revealed that BaZ was present in very low quantities.

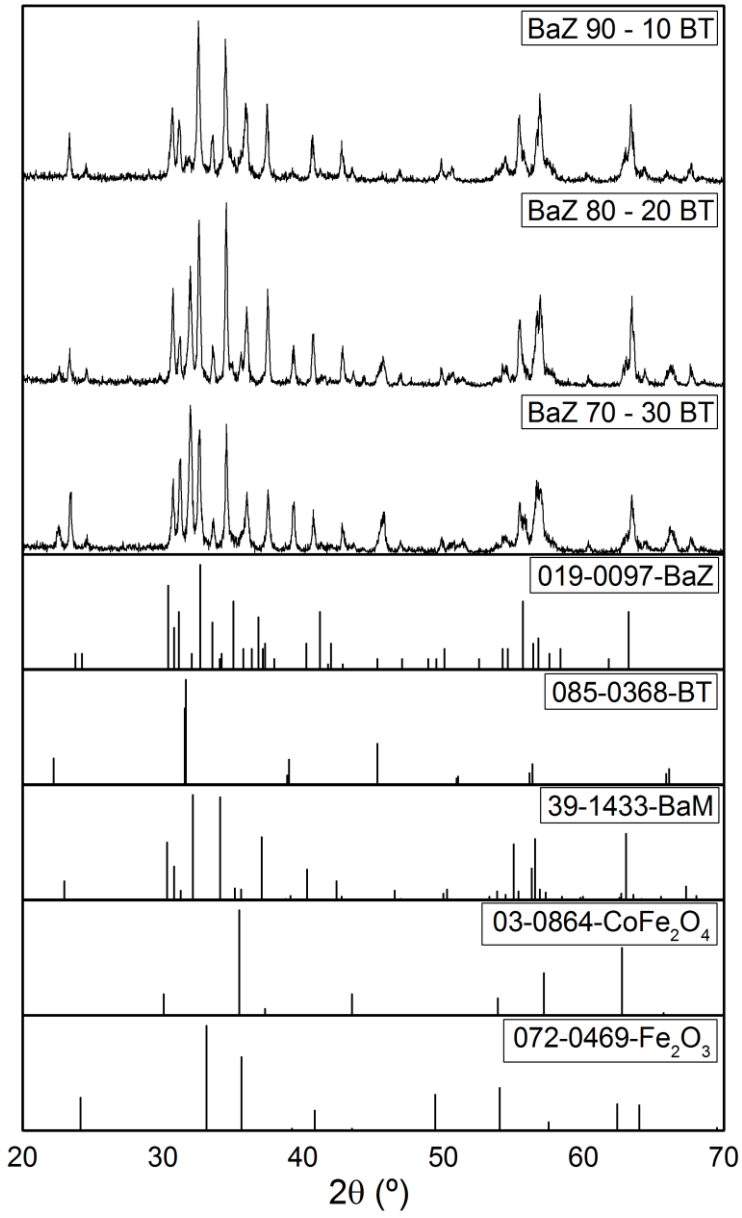

Figure 51: Sintered BaZ-BT composites with different weight percentage, produced by sol-gel method.

The SrZ composite showed that the presence of BT phase without diffusion of atoms between the phases (figure 52), and the phase corresponding to the SrZ had a very low intensity. This method reveals itself to be not appropriate to produce Z-ferrite composites, compared with the others method in this study. Perhaps some change in the procedure should make some difference, such as making a better mixture of the compounds before sintering the composite.

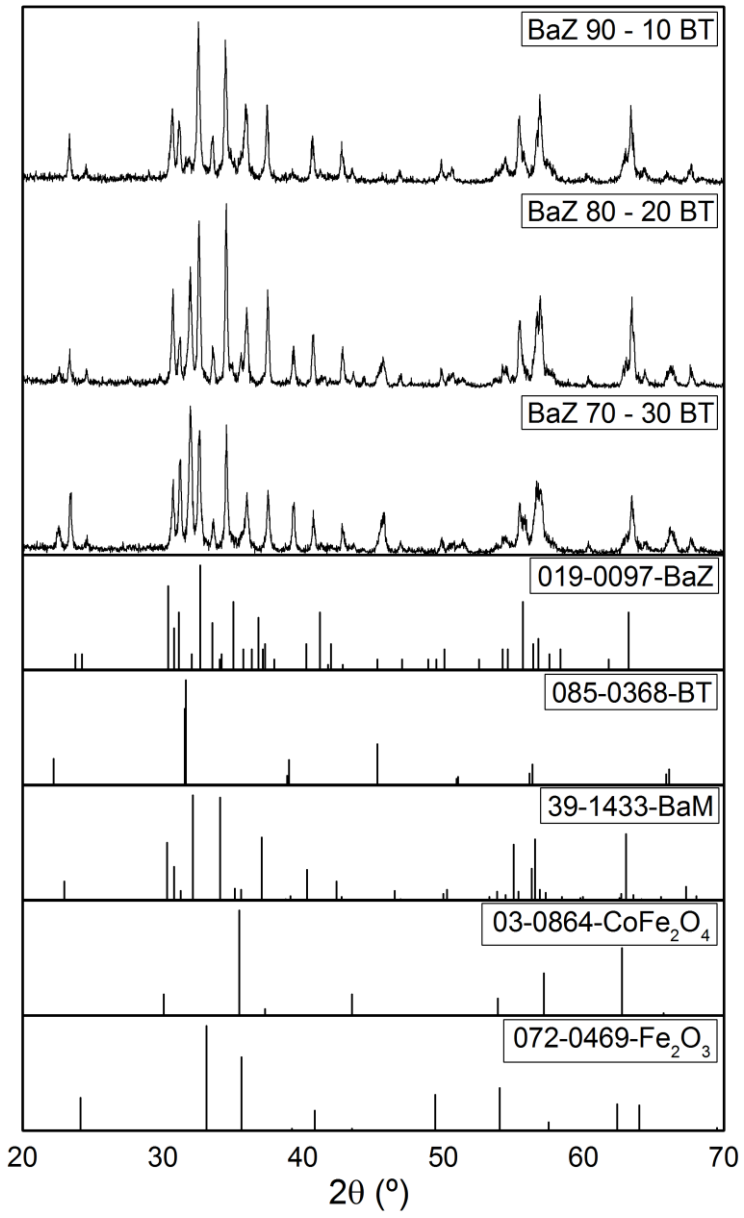

Figure 52: Sintered SrZ-BT composites with different weight percentage, produced by sol-gel method.

In the table 10 is a summary of the phases present in composites of hexaferrites with $BaTiO_3$, it is showed the principal phases in bold and the precursor phases underlined of all methods and weight percentages. Also the best method for the different compositions have the background in grey.

Table 10: Summary of the phases present in composites of hexaferrites and $BaTiO_3$

		Soli state reaction	Coprecipitation	Sol-gel	Citrates	
Pellets	BaM + BT 70 - 30 80 - 20 90 - 10	**BaM, BT**, $BaFeO_{2.9}$, $BaFeO_3$	**BaM, BT**	**BaM, BT**, Hematite	**BaM, BT**	Phases
	SrM + BT 70 - 30 80 - 20 90 - 10	SrM, $SrTiO_3$, BT	**SrM, BT**, Hematite	**SrM, BT**, Hematite	SrM, $SrTiO_3$, BT	
	BaZ + BT 70 - 30 80 - 20 90 - 10	BaZ, **BT,** BAM	BaZ, BT, Co_2Y, BaM, Hematite	BaZ, BT, BaM, $CoFe_2O_4$, Hematite	BaZ, BT, Co_2Y	
	SrZ + BT 70 - 30 80 - 20 90 - 10	SrZ, **BT,** SRM	SrZ, BT, $(Sr_{0.5}Ba_{0.5})(coO_{2.5})$, $Ba(Fe_{10.3}Co_{0.85}Ti_{0.95}O_{19})$	SrZ, BT, SrM, $CoFe_2O_4$, Hematite	SrZ, SrM, $SrTiO_3$, BT	

4.2.3. Composites of hexaferrites and KNN

4.2.3.1. Solid state reaction

The XRD of the BaM-BT composites of solid state reactions, figure 53, shows a very clear phase without any formation of secondary phase.

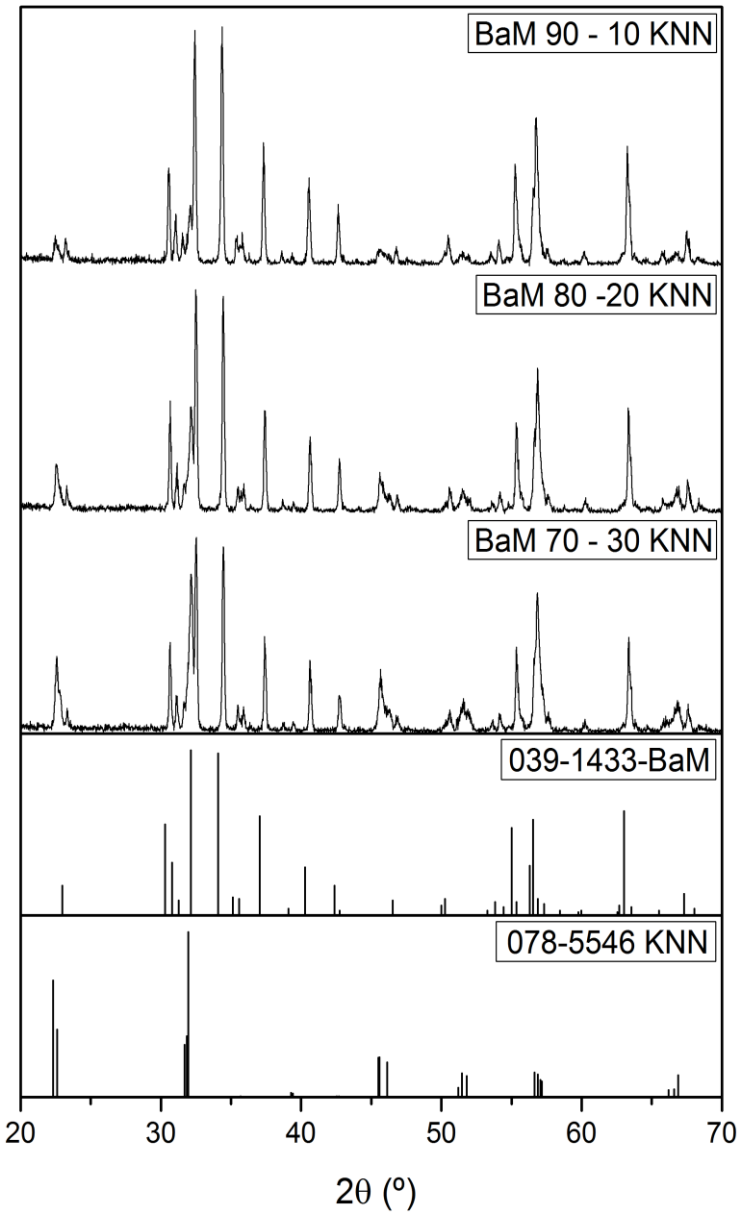

Figure 53: Sintered BaM-KNN composites with different weight percentage, produced by solid state reaction method.

The SrM-BT composites shows the hematite phase in all weight percentages (figure 54), and there was not a decrease of this phase with different weight percentages of the SrM phase.

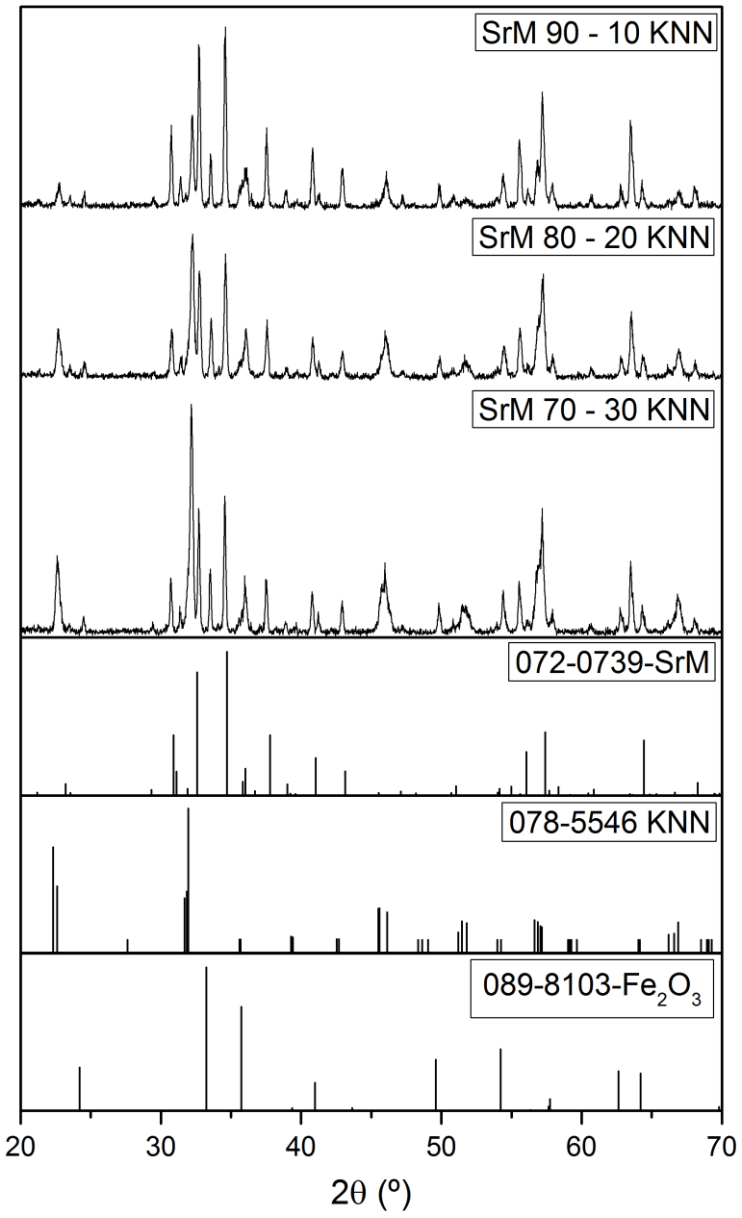

Figure 54: Sintered SrM-KNN composites with different weight percentage produced by solid state reaction method.

In the case of the Z-ferrites composites with KNN, they show secondary phases present in all the weight compositions. The BaZ composite, figure 55, has secondary phases of BaM ferrite and $CoFe_2O_4$ spinel, which decrease with the increase of KNN, and there is another secondary phase that results from the diffusion of atoms of Ba^{2+} from the Z-ferrite and NbO_3 from KNN forming a cubic structure of $Ba(NbO_3)$ (PM3-M) phase.

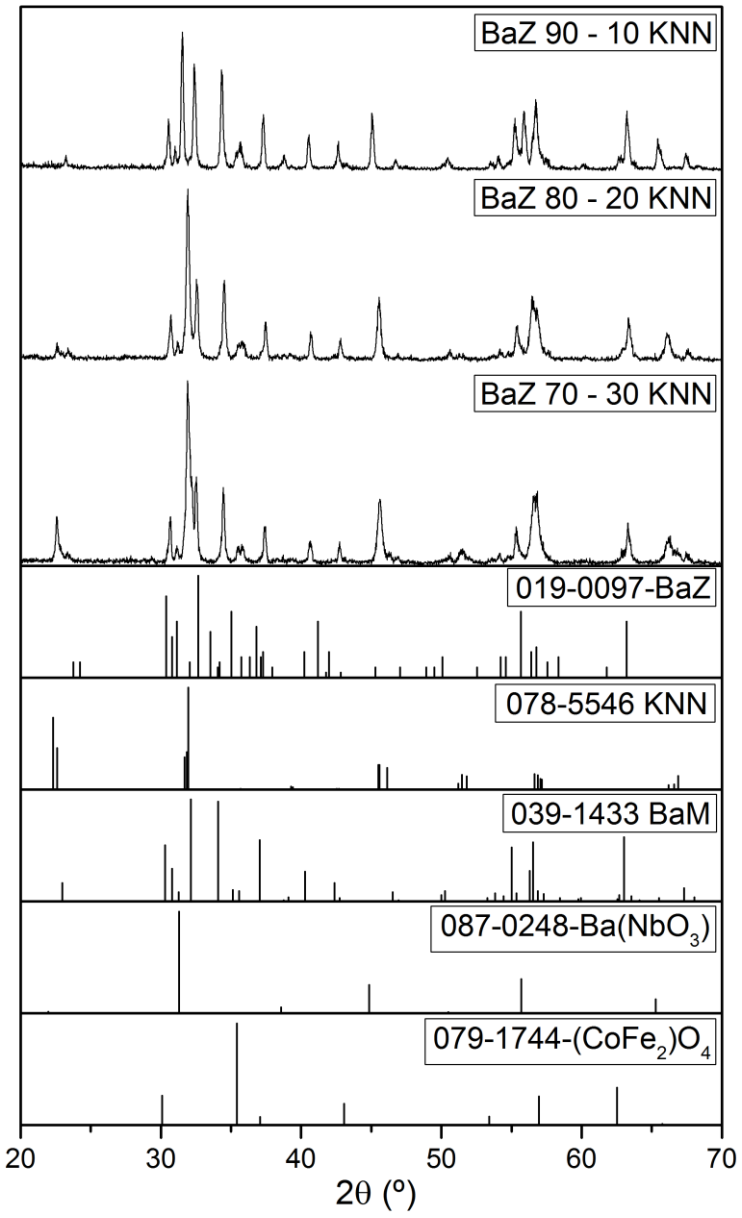

Figure 55: Sintered BaZ-KNN composites with different weight percentage, produced by solid state reaction method.

In the SrZ composite with KNN the XRD showed there was a diffusion into the KNN phase by atoms of Sr^{2+}, forming a different unexpected perovskite phase (figure 56), of sodium-strontium-niobate. It seems that the potassium present in the KNN phase was evaporated during the sintering, potassium can be very hard to maintain at these temperatures due to its volatility.

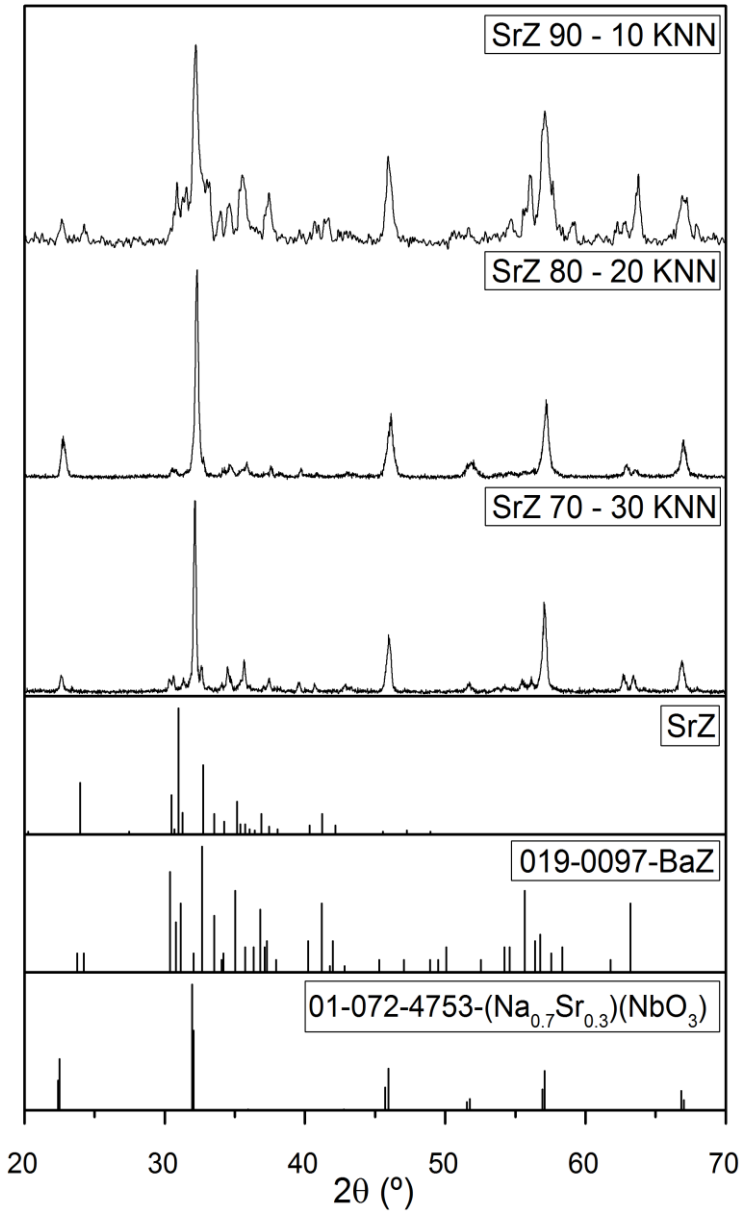

Figure 56: Sintered SrZ-KNN composites with different weight percentage produced by solid state reaction method.

The M-Ferrites composites did produce a very distinct phases with high intensity peaks, the Z-ferrites composites have secondary phases that may be interesting to research in the future for new applications.

4.2.3.2. Coprecipitation

The XRD of BaM composites with KNN showed three phases: KNN, BaM and hematite (figure 57). With the decrease of KNN phase the hematite increased, as this phase was already present in the calcination of the BaM ferrite of the same method.

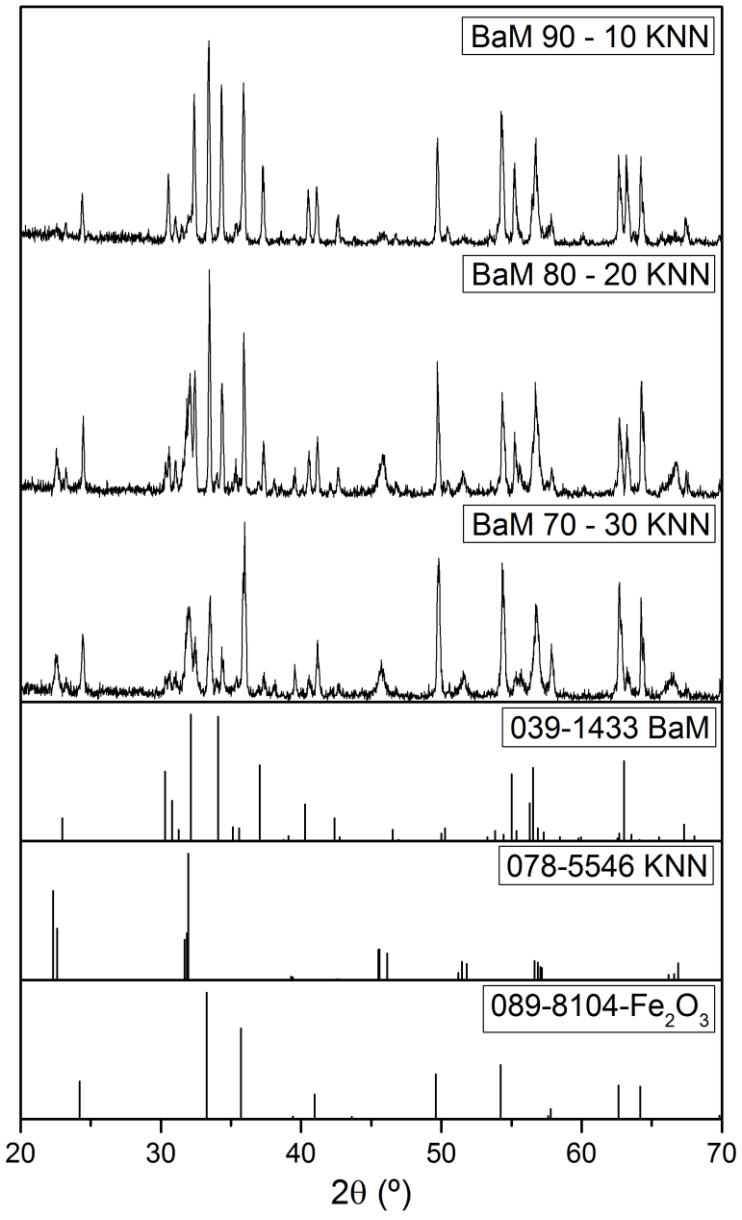

Figure 57: Sintered BaM-KNN composites with different weight percentage, produced by coprecipitation method.

In the SrM composites (figure 58) it is possible to see a formation of a new perovskite phase $(Na_{0.7}Sr_{0.3})(NbO_3)$, the same sodium-strontium-niobate seen in the SrZ composites above. There was a diffusion of atoms between the KNN phase and SrM phase. The SrM phase and hematite are present, has the same as in the BaM composites, the hematite decreases with the increase of the KNN Phase, this phase was already present in the coprecipitation powder. The hexaferrites have a very low intensity peaks.

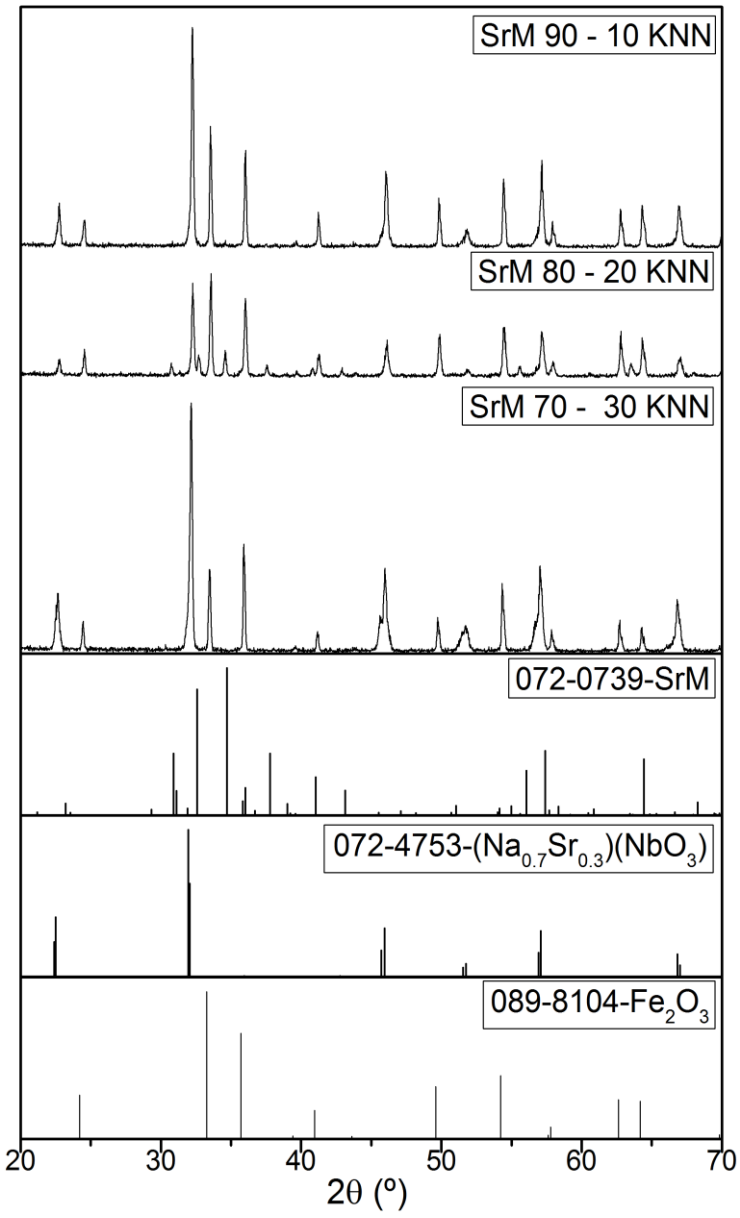

Figure 58: Sintered SrM-KNN composites with different weight percentage, produced by coprecipitation method.

In the XRD of BaZ composites (figure 59) there is the presence of M, Y phases and the spinel ($CoFe_2O_4$) phase, and these phases are more intensive in the composites with 80% of BaZ and 20% KNN. The Y phase was not seen in the calcination of the Z-ferrite, and did only appear when sintering the composite. The BaZ ferrite and KNN phases are visible in the XRD.

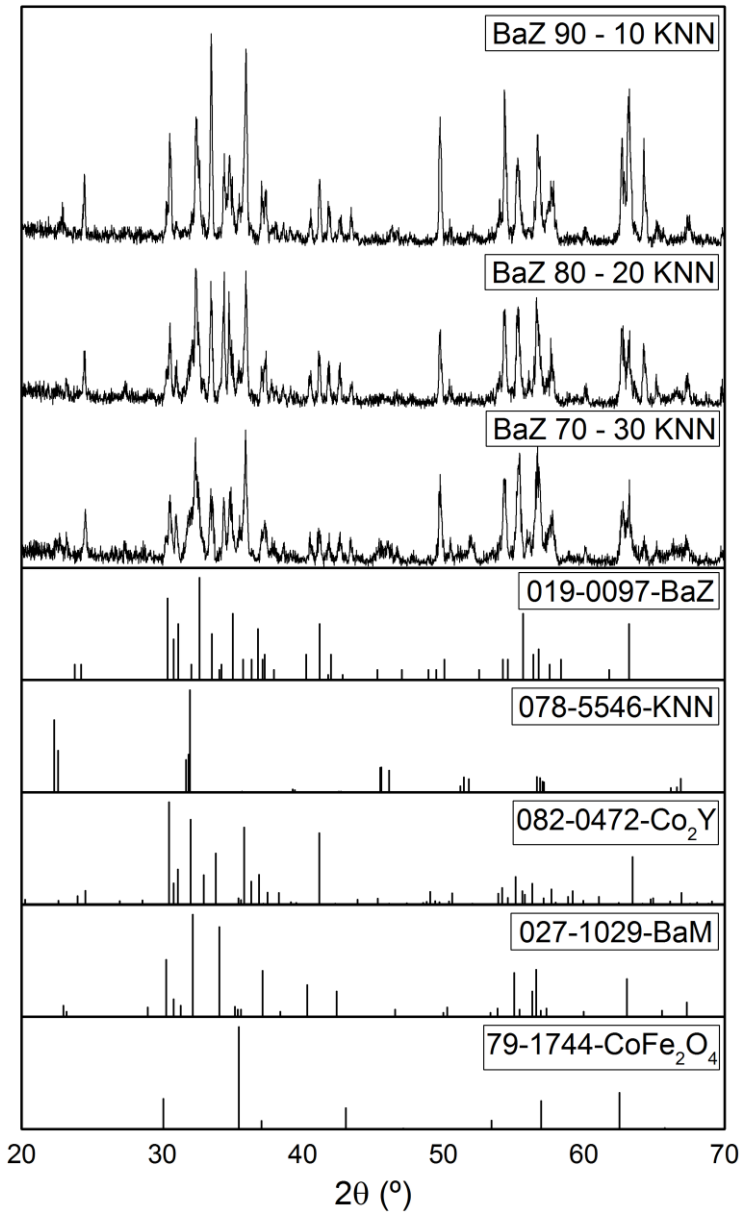

Figure 59: Sintered BaZ-KNN composites with different weight percentage produced by coprecipitation method.

The XRD of SrZ didn't shown any trace of SrZ and KNN phase (figure 60), there was a diffusion between them forming several new phases, producing some secondary phases. The new phases include cobalt iron oxide with cubic structure (Fd-3m), strontium iron niobium oxides tetragonal structure (P4mm), strontium cobalt oxide brownmillerite structure and sodium strontium niobium oxide with tetragonal structure.

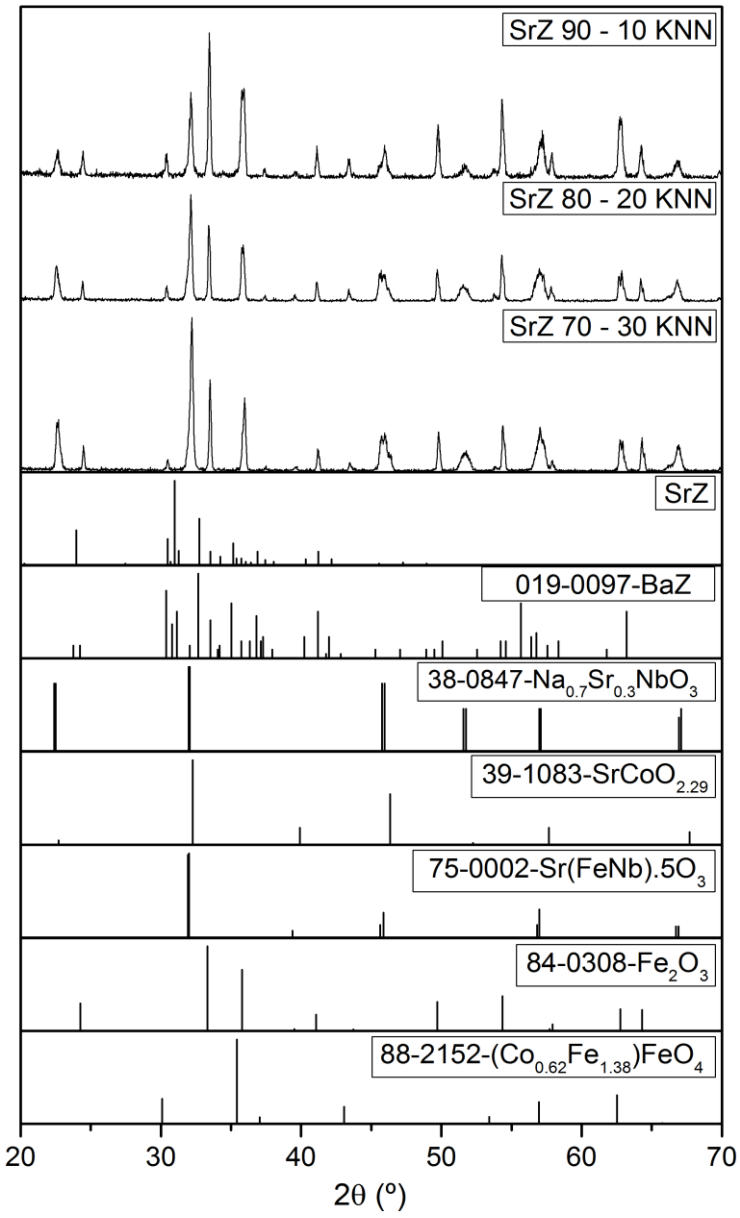

Figure 60: Sintered SrZ-KNN composites with different weight percentage, produced by coprecipitation method.

4.2.3.3. Citrates synthesis

According to the XRD of the composites of BaM with KNN, there were only two phases formed as expected. It is possible to see in figure 61 the well-formed phases of the composite.

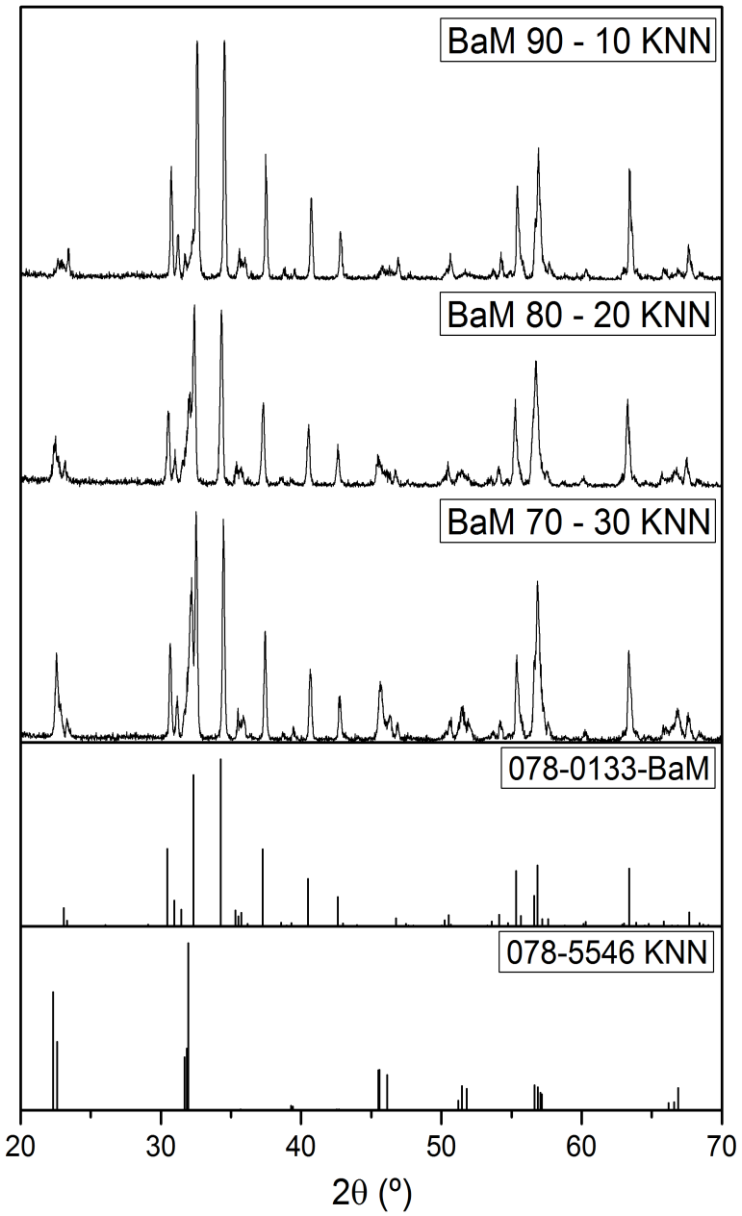

Figure 61: Sintered BaM-BT composites with different weight percentage produced, by citrates synthesis method.

The XRD from the SrM composites with KNN (figure 62) showed completed phases formation of KNN and SrM, is possible to visualise high intensive peaks of both phases and very distinct.

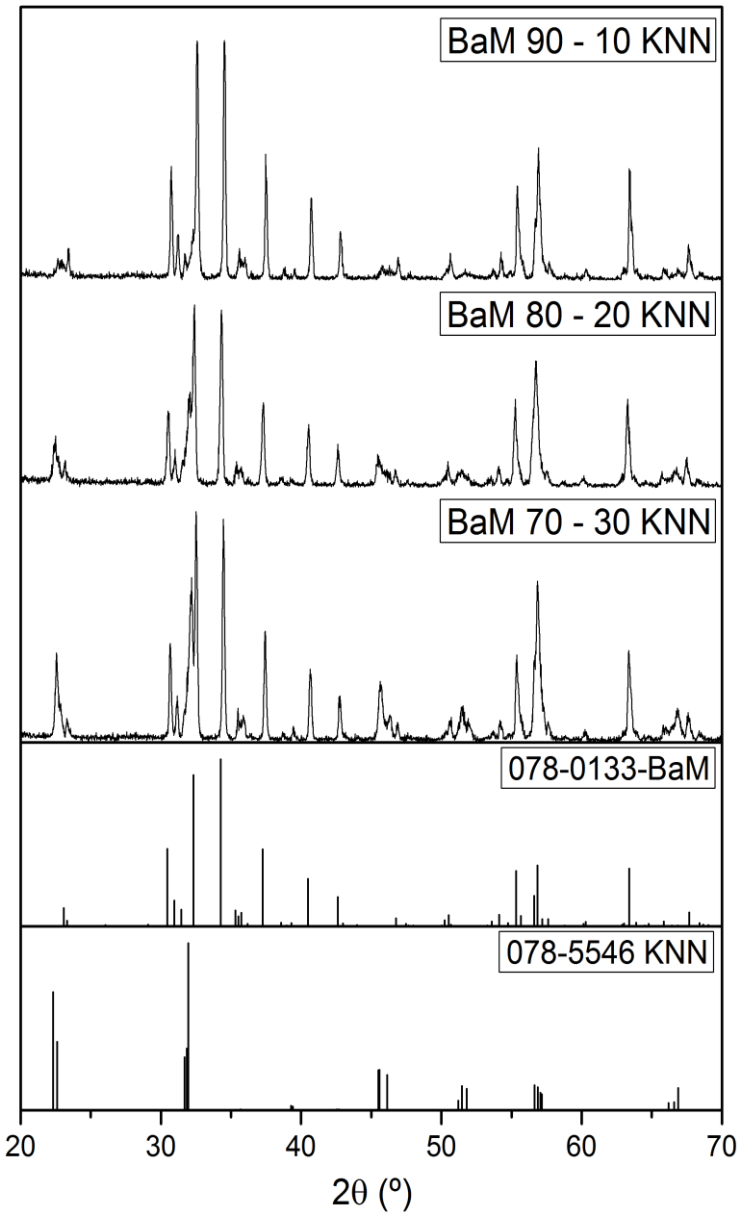

Figure 62: Sintered SrM-KNN composites with different weight percentage, produced by citrates synthesis method.

The XRD of BaZ shows high intensities peaks of both phases the KNN phase is very distinguish and is possible to visualise that has even highest peaks then the BaZ ferrite, there a possibility of secondary phases present a peak in the 35° was not possible to determinate with XRD patterns. There was not a formation of secondary phases (figure 63), the good intensity peaks of the diffraction angle facilitating the comparisons with the standard patterns files.

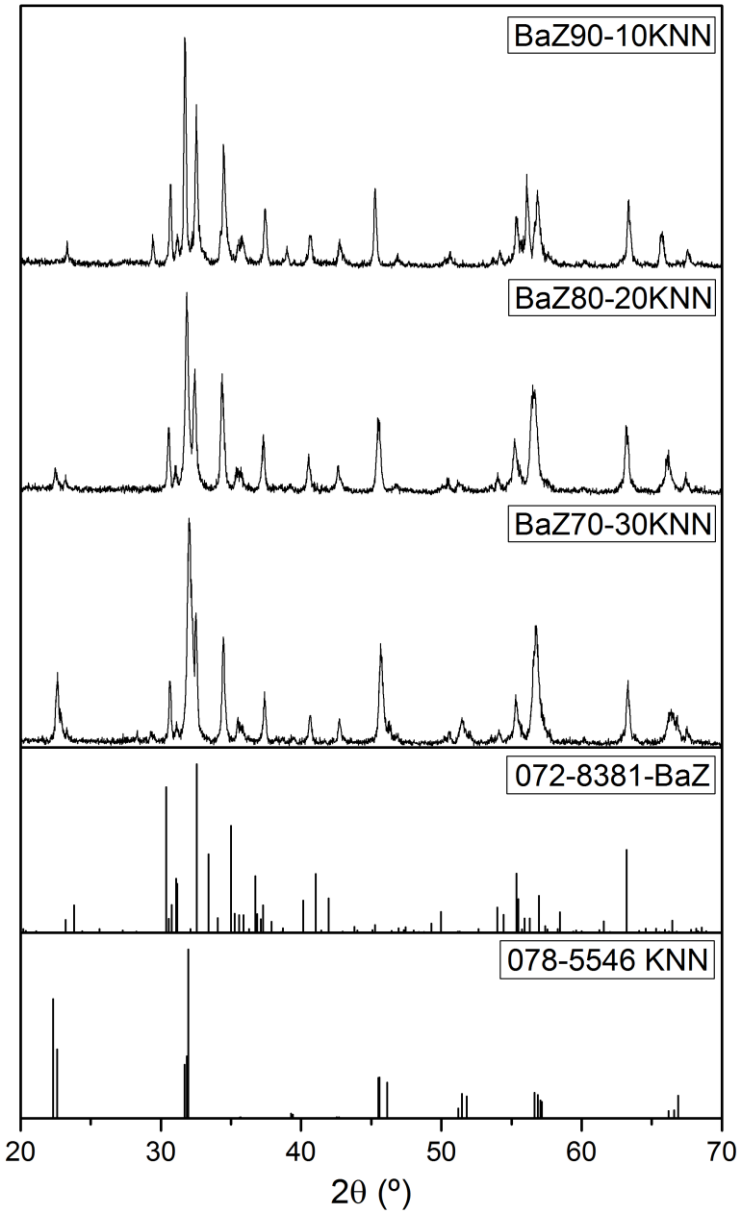

Figure 63: Sintered BaZ-KNN composites with different weight percentage, produced by citrates synthesis method.

The XRD of SrZ shows the formation of a new phase $Na_{0.7}Sr_{0.3}(NbO_3)$ (figure 64). Clearly there is a diffusion between phases, also there was not a trace of potassium, but there is also a very small amount of SrZ phase.

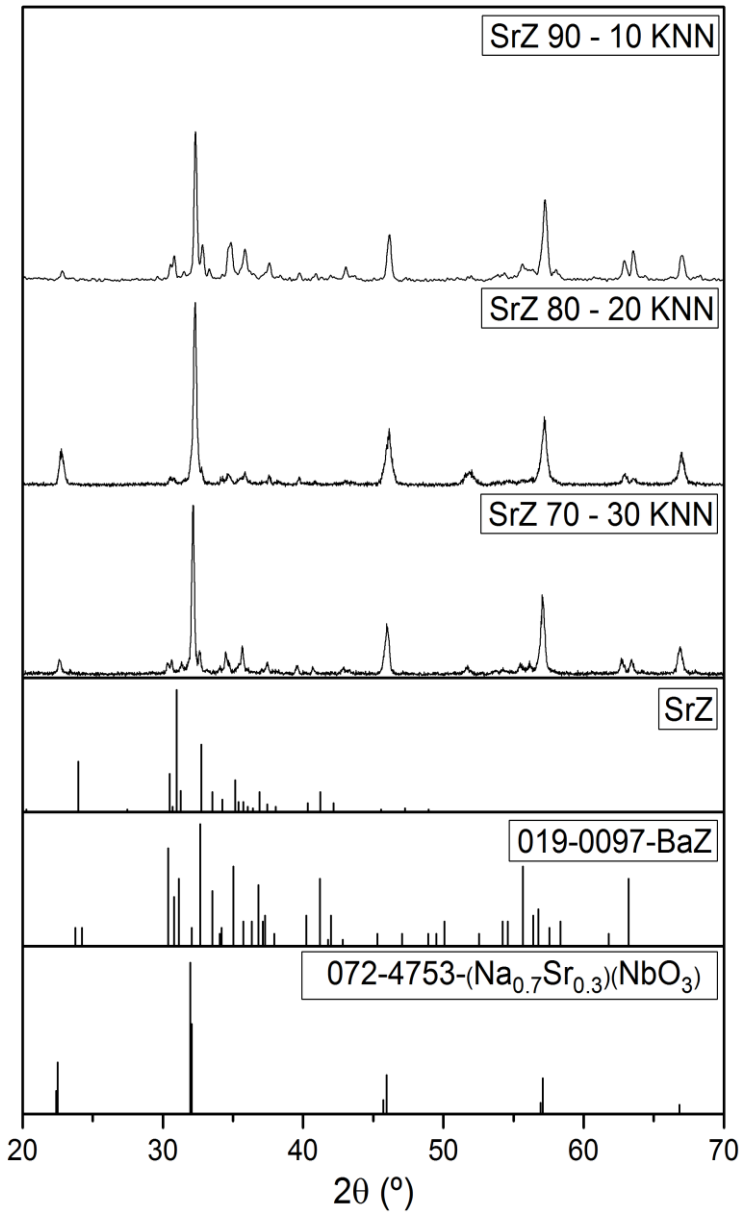

Figure 64: Sintered SrZ-KNN composites with different weight percentage, produced by citrates synthesis method.

4.2.3.4. Sol-Gel

The Composites of hexaferrites and KNN of the method sol-gel showed presence of ferrites phase and KNN phase with high intensive peaks but does contains secondary phases. In the BaM composites, figure 65, a formation of secondary phase is visible, as the atoms of barium diffuse to the KNN phase forming $Ba(NbO_3)$, cubic structure (Pm-3m) with low intensity peaks. There was still the presence of hematite with high intensity peaks, and this phase decreased with the increase of the KNN phase.

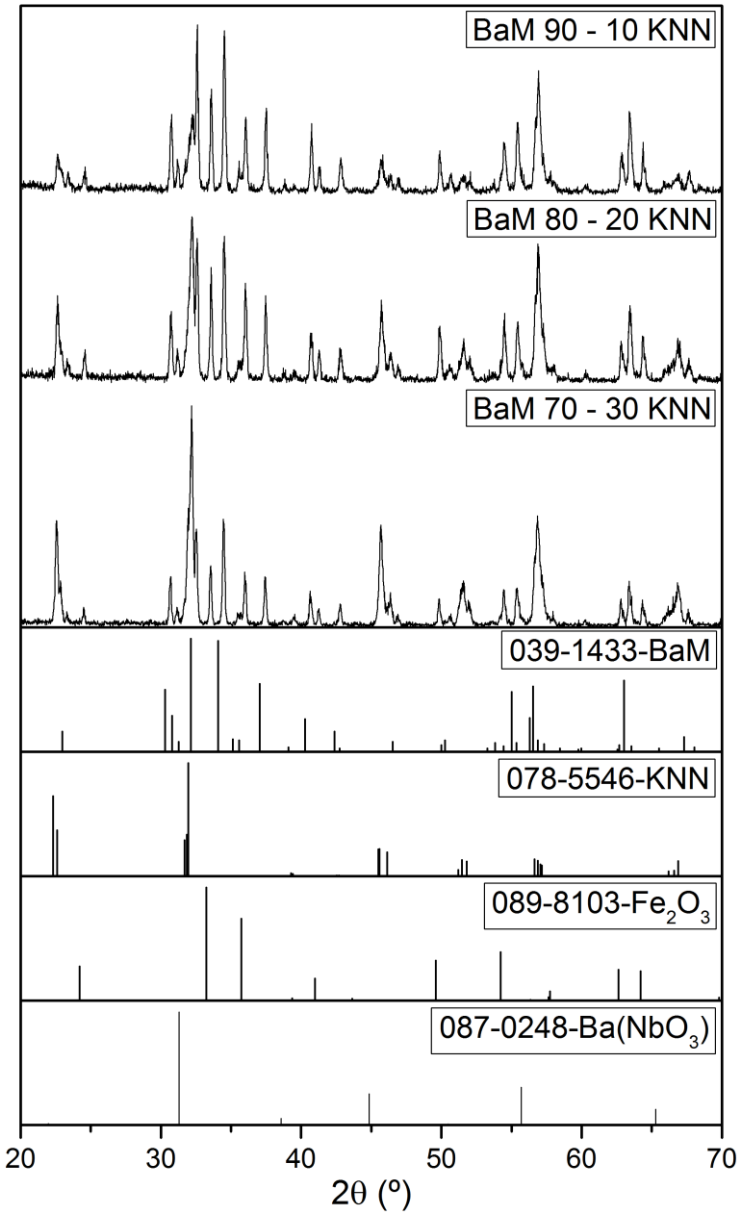

Figure 65: Sintered BaM-BT composites with different weight percentage produced, by sol-gel method.

In the strontium composites with KNN was detected high intensity peaks of hematite, figure 66, they were detected in all these composites overlap the main phase (SRM). The XRD of the composites shows some intensity peaks of SrM and KNN with lower intensity peaks compared with the hematite.

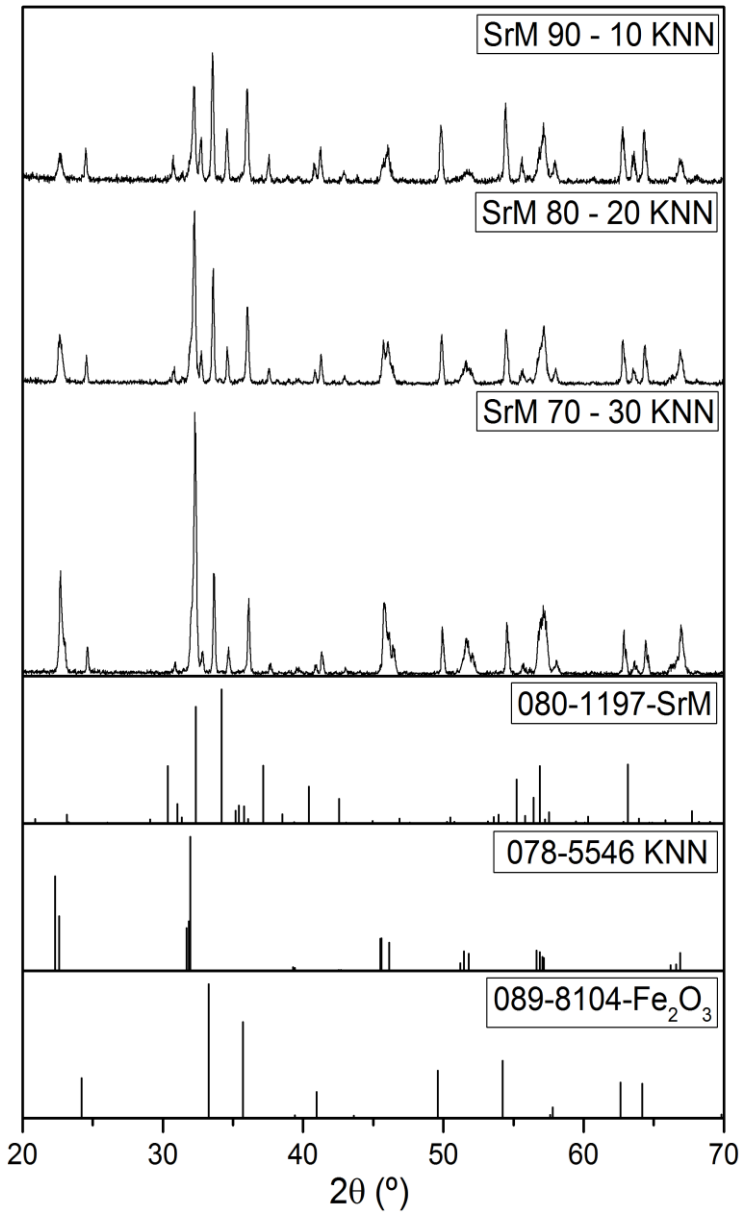

Figure 66: Sintered SrM-KNN composites with different weight percentage, produced by sol-gel method.

In the BaZ composites, the intensity of the peaks hematite was high in all compositions (figure 67), the XRD was unable to detect the BaZ phase, although the phases, BaM, KNN were detected with intensive peaks.

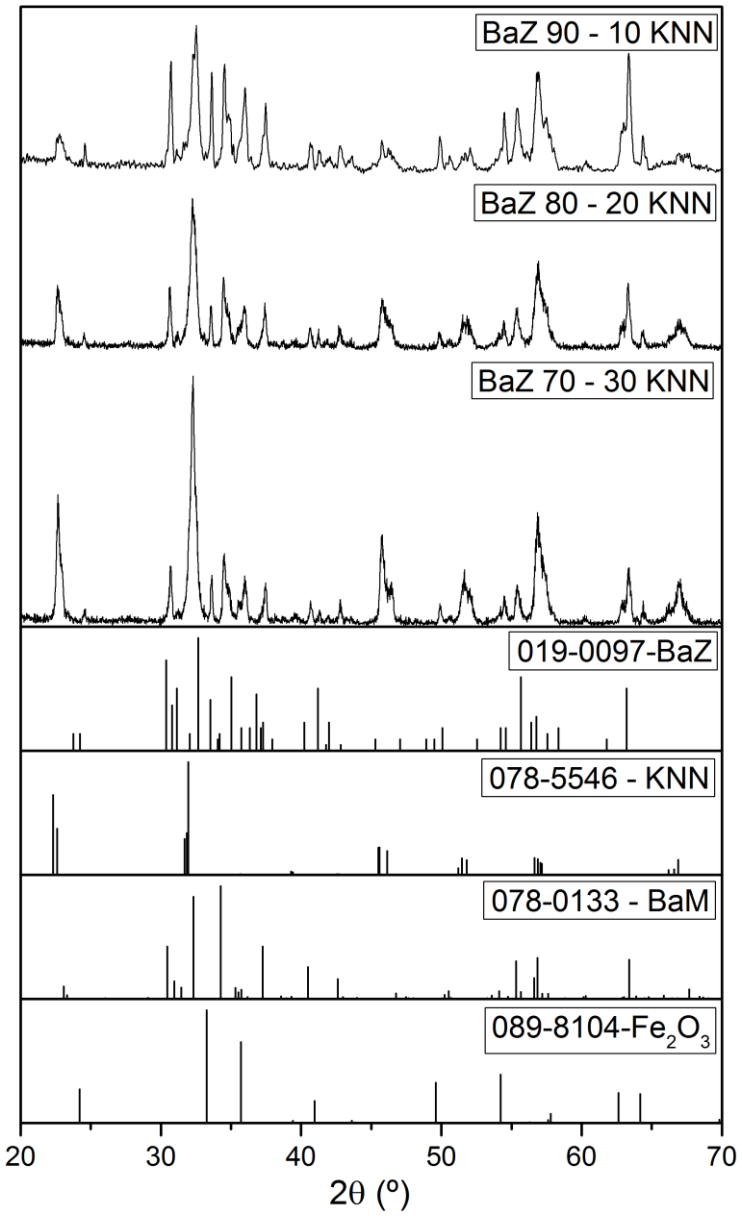

Figure 67: Sintered BaZ-KNN composites with different weight percentage, produced by sol-gel method.

The SrZ composites showed the main phase SrZ, the peaks of the diffraction angle of the pattern 019-0097 match the XRD of the composites (figure 68). Like the BaZ, this samples also did show the presence of SrM ferrite and hematite with high intensity peaks. This composites also contains the KNN phase without forming new phases.

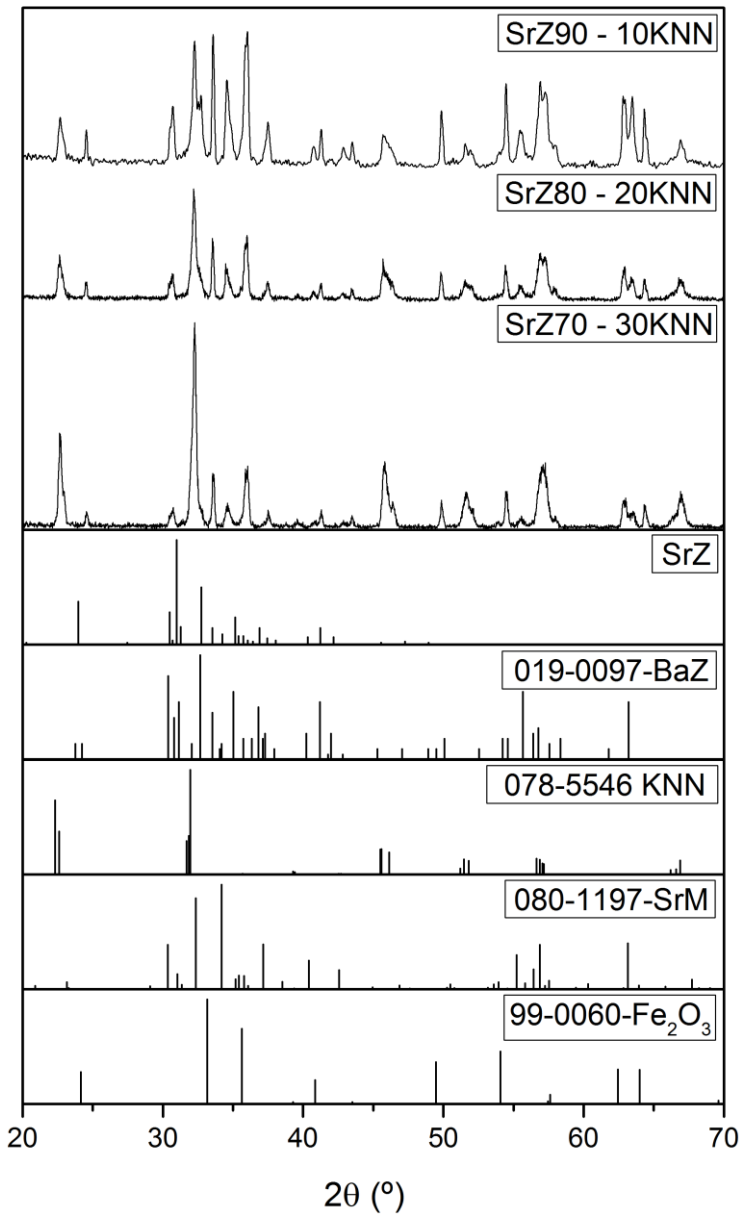

Figure 68: Sintered SrZ-KNN composites with different weight percentage, produced by sol-gel method.

Table 11: summary of the phases present in the composites with KNN.

		Soli state reaction	Coprecipitation	Sol-gel	Citrates	
Pellets	BaM + KNN 70 - 30 80 - 20 90 - 10	**BaM, KNN**	**BaM, KNN,** Hematite	BaM, KNN, Hematite, $Ba(NbO_3)$	**BaM, KNN**	Phases
	SrM + KNN 70 - 30 80 - 20 90 - 10	**SrM, KNN,** Hematite	SrM, $(Na_{0.7}Sr_{0.3})(NbO_3)$*, Hematite	**SrM, KNN**, Hematite	**SrM, KNN**	
	BaZ + KNN 70 - 30 80 - 20 90 - 10	BaZ, KNN, BaM, $Ba(NbO_3)$, $CoFe_2O_4$	BaZ, KNN, Co_2Y, BaM, $CoFe_2O_4$	BaZ, KNN, BaM, Hematite	**BaZ, KNN**	
	SrZ + KNN 70 - 30 80 - 20 90 - 10	SrZ, $(Na_{0.7}Sr_{0.3})(NbO_3)$*	SrZ, Hematide $Sr(FeNb)5.O_3$, $(Na_{0.7}Sr_{0.3}NbO_3)$, $SrCoO_{2.29}$	SrZ, KNN, SrM, Hematite	SrZ, $(Na_{0.7}Sr_{0.3})(NbO_3)$*	

4.2.4. Final conclusions on XRD of prepared composites

The BT composites with hexaferrites in general showed the two main phases in some cases with intensity peaks easy to distinct, the M-ferrites are visible in the XRD of all methods, although we detected a trace of secondary phases that can compromise some measurements such the $SrTiO_3$ phase. In the Z-ferrites there were more secondary phases present, the main phases had a very low peak intensities. The different synthesis methods had produced ferrites and composites with high intensity phases, not all were possible to obtain pure phases. The composites of BT and M-ferrite had less secondary phases in the methods of coprecipitation and citrates, in the Z-ferrites composites with BT was the solid state reaction and citrates, is not possible to conclude the very best method between them.

The KNN composites had shown phases more distinct then the BT composites and in M-ferrites less secondary phases, in the XRD it is visible that in the composites from citrates synthesis there was a presence of only M-ferrites and KNN phases also the BaZ composite, but the other methods were not so efficient, with the formation of new phases occurring in the composites. The sintering of the composites with Z-ferrites and KNN showed some secondary phases such as Y-ferrites and M-ferrites with high intensity peaks, and also in SrZ there was a diffusion between

atoms producing a new phase $Na_{0.7}Sr_{0.3}(NbO_3)$, the XRD of the SrZ composites of method of sol-gel had showed there was a phase of SrZ in contrast with the others methods.

4.3.Scanning Electron Microscope – Images

With SEM microscopy it is possible to visualize the microstructure of the composites, shape, size, and distribution of the grains, and also these images are important to observe if the composites had porosity. The following SEM images were taken from the different compositions and different weight percentage of samples pressed in the cold isotactic press (CIP) after sintering.

4.3.1. $BaTiO_3$

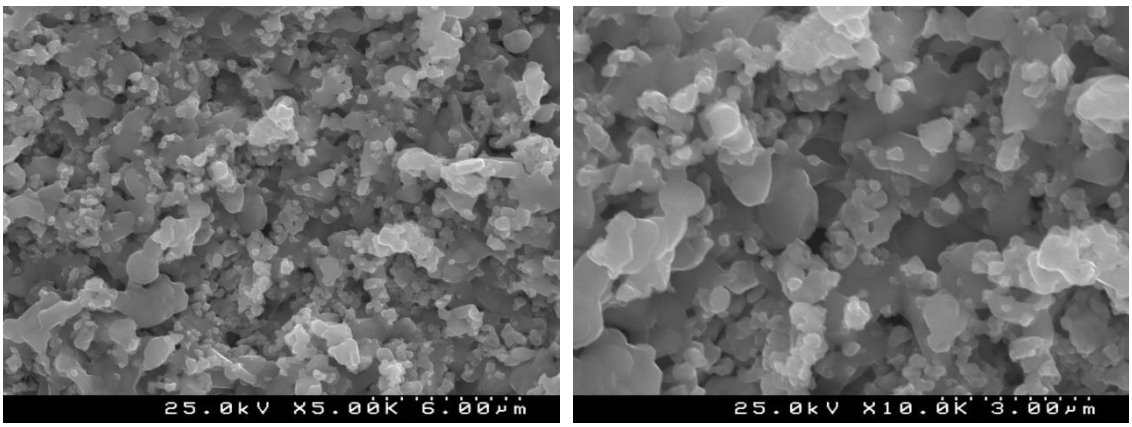

Figure 69: SEM images of BaM composites with 30% of BT of solid State reaction method, image in the left 5k magnification and the image in the right 10k magnification.

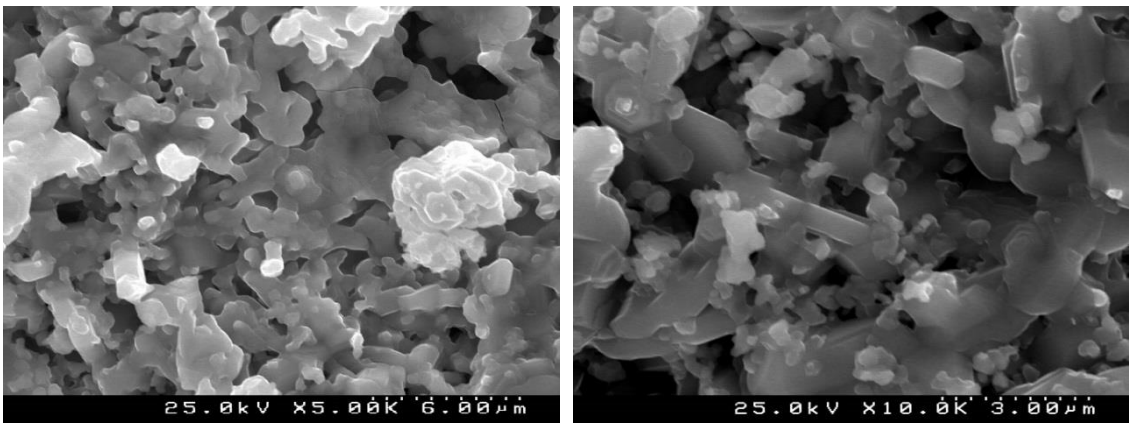

Figure 70: SEM images of SrM composites with 30% of BT of solid State reaction method, image in the left 5k magnification and the image in the right 10k magnification.

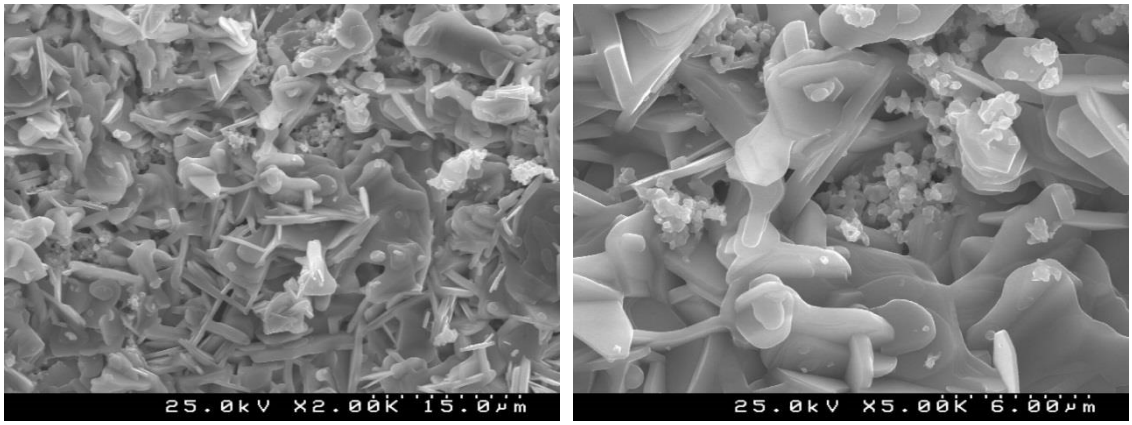

Figure 71: SEM images of BaZ composites with 30% of BT of solid State reaction method, image in the left 2k magnification and the image in the right 5k magnification.

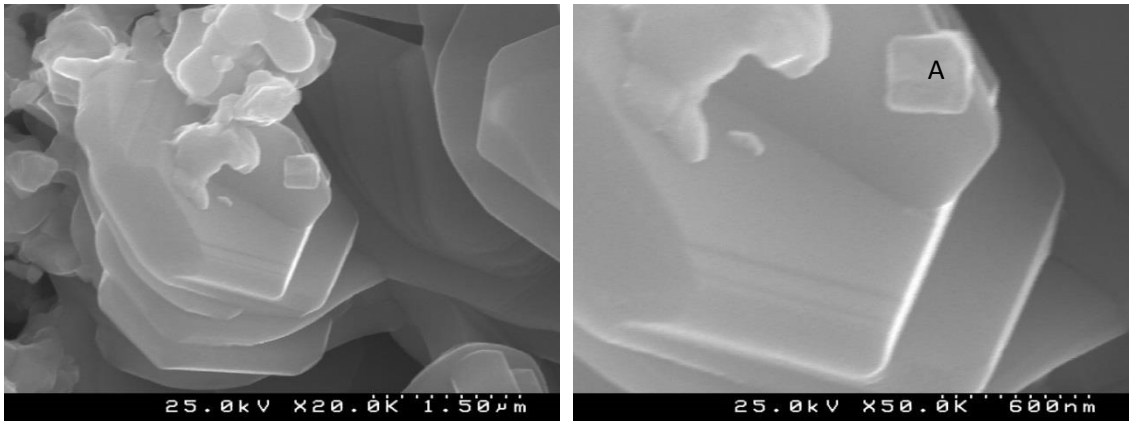

Figure 72: SEM images of BaZ composites with 30% of BT of solid State reaction method, image in the left 20k magnification and the image in the right 50k magnification with labelled grains, A – $BaTiO_3$.

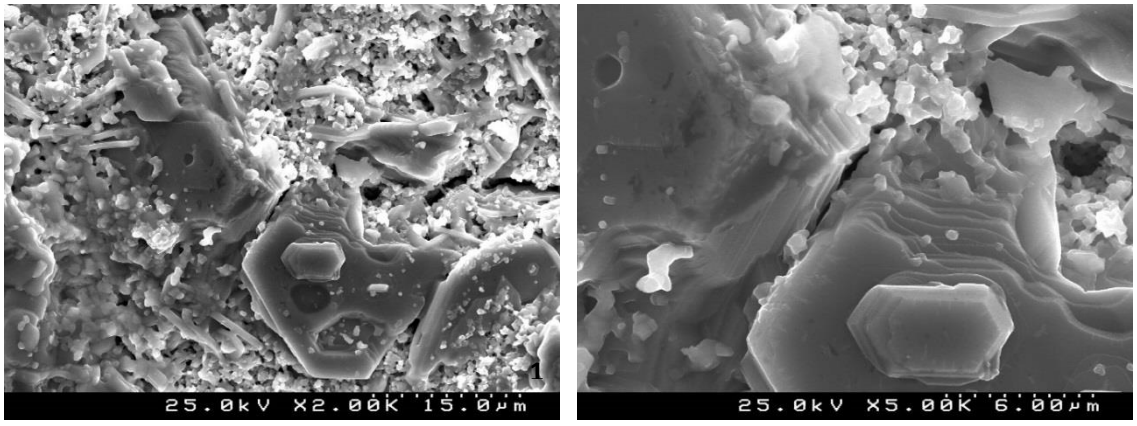

Figure 73: SEM images of SrZ composites with 30% of BT of solid State reaction method, image in the left 2k magnification and the image in the right 5k magnification.

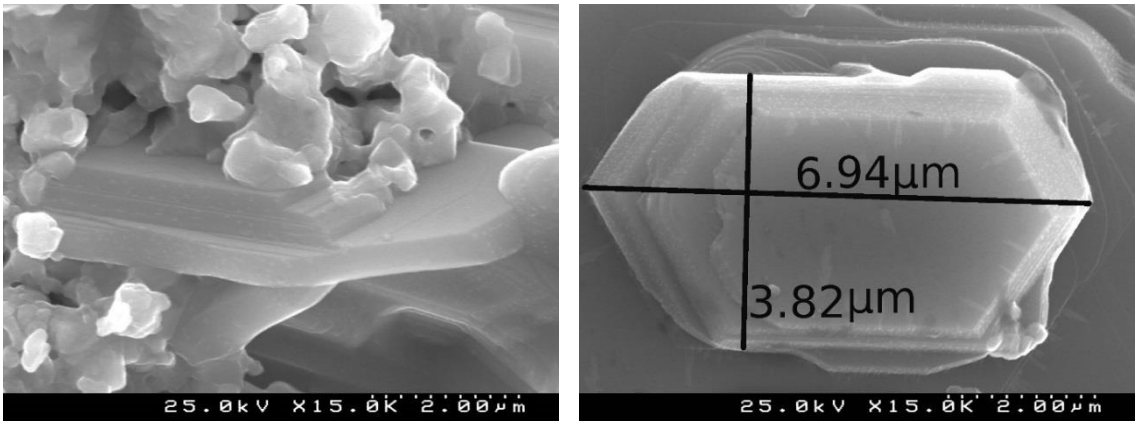

Figure 74: SEM images of SrZ composites with 30% of BT of solid State reaction method, both images with 15k magnification, the image in the right shows the size of a representative hexagonal grain of SrZ ferrite.

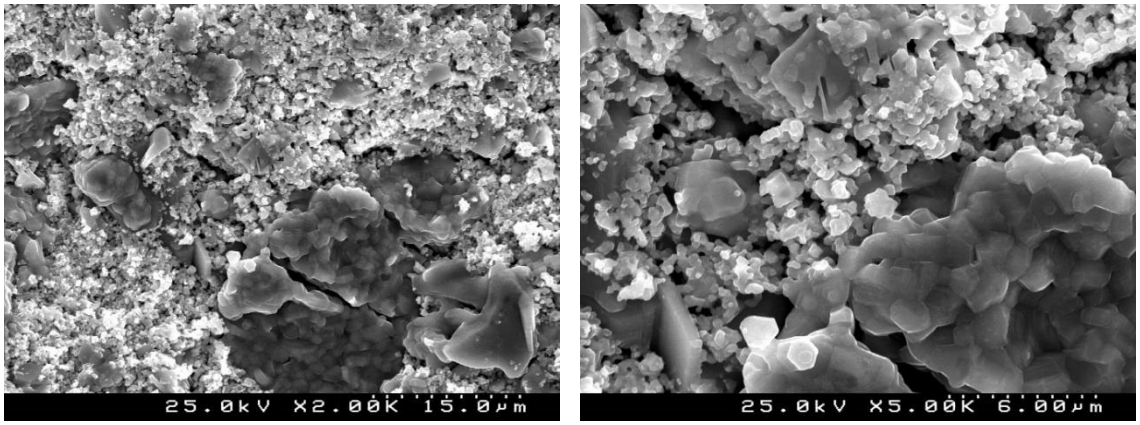

Figure 75: SEM images of BaM composites with 30% of BT of sol-gel method, image in the left 2k magnification and the image in the right 5k magnification.

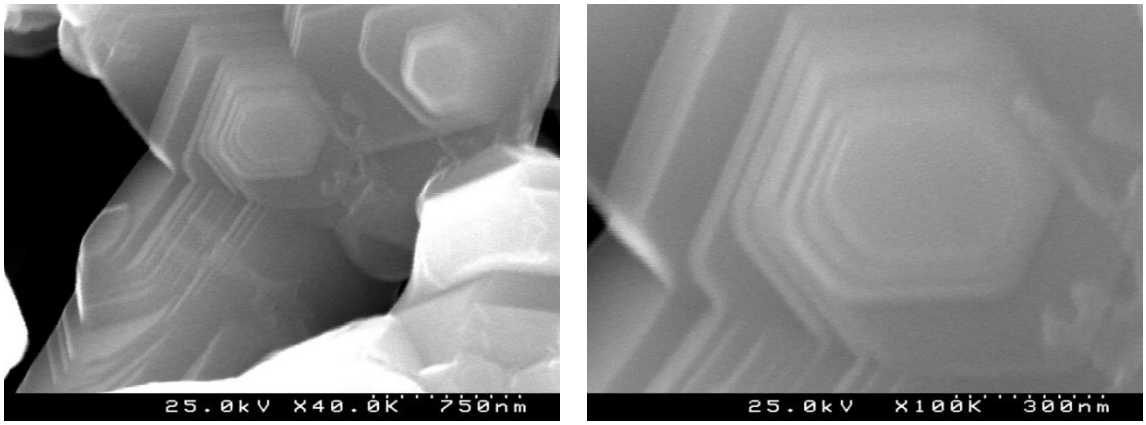

Figure 76: SEM images of BaM composites with 30% of BT of sol-gel method, with higher magnification, image in the left 40k magnification and the image in the right 100k magnification.

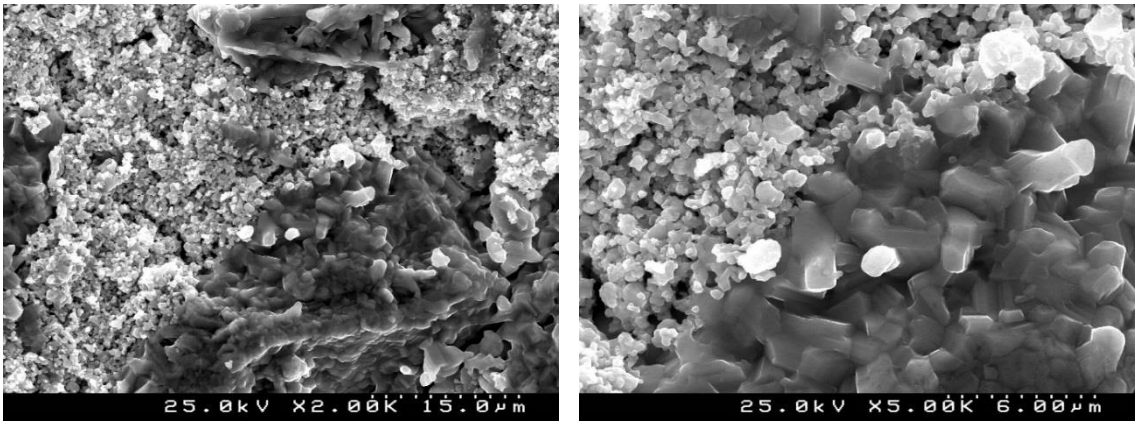

Figure 77: SEM images of SrM composites with 30% of BT of sol-gel method, image in the left 2k magnification and the image in the right 5k magnification.

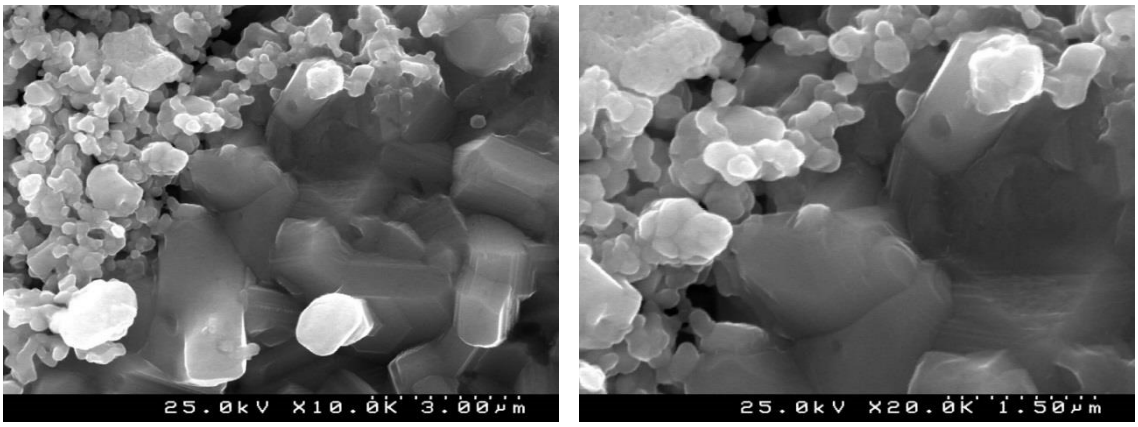

Figure 78: SEM images of SrM composites with 30% of BT of sol-gel method, image in the left 10k magnification and the image in the right 20k magnification.

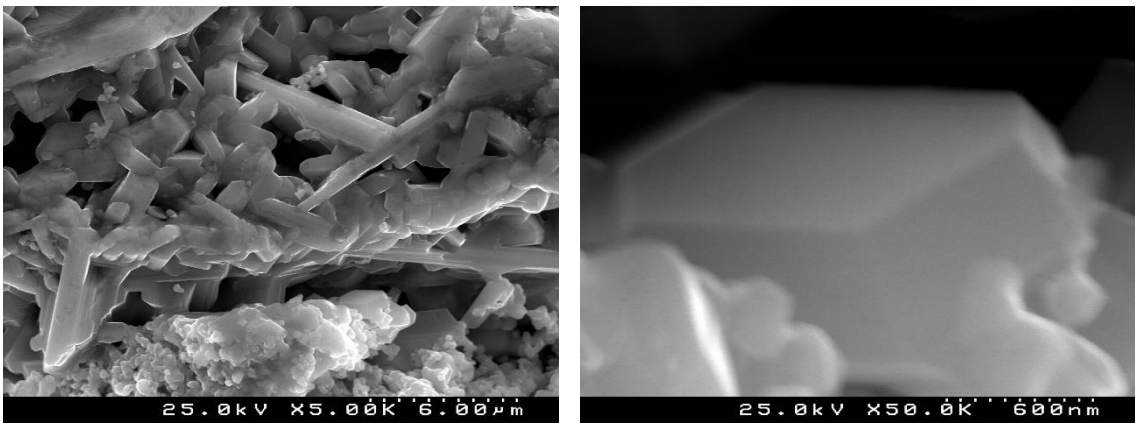

Figure 79: SEM images of SrZ composites with 30% of BT of sol-gel method, image in the left 5k magnification and the image in the right 50k magnification of a hexagonal grain of SrZ ferrite.

With SEM images of BT composites was possible to distinguish different phases by the shape of the grains. The hexaferrites have a hexagonal unit cell symmetry, corresponding to the grains with hexagonal edges, while the grains with cubic symmetry represents the ferroelectric

phase $BaTiO_3$, although this often appears a small, irregularly shaped grains. The BaM composite with 30% of BT, figure 69, had showed a phase distribution of BT and BaM grains has was measured in the XRD, and also visible are some grains with a nearly round shape - this possibly means not all grains are form hexaferrites and BT.

In the SEM images of SrM composites with BT of the solid state reaction, figure 70, it is possible to visualize elongated grains. The SrM composites had high porosity, the grains didn't appear to be orientated in all the M – ferrite samples, and all had different directions. The Z-ferrites of the solid state reaction method, figures 71 to 74, had very well formed grains. The hexagonal ferrites are easy to identify as are the cubic grains of BT. In figure 74 a SrZ grain was measured to obtain a relative dimension of the hexagonal grains, 6.94µm x 3.82µm.

The SEM images of sol-gel showed a more distinct shape of hexagonal grains, such as the BaM composites in figure 76, and hexagonal shape grains in the SrZ composites in figure 79, also visible is a small percentage of cubic grains in the sol-gel method.

Other SEM images were also taken, and also showed the same shape, grain orientation and size as these representatives images.

4.3.2. KNN

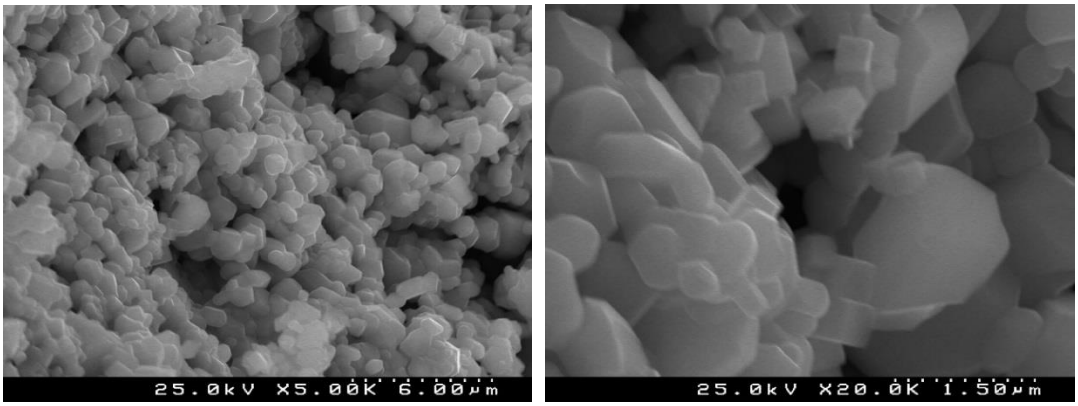

Figure 80: SEM images of BaM composites with 30% of KNN of citrates synthesis method, image in the left 5k magnification and the image in the right 20k magnification.

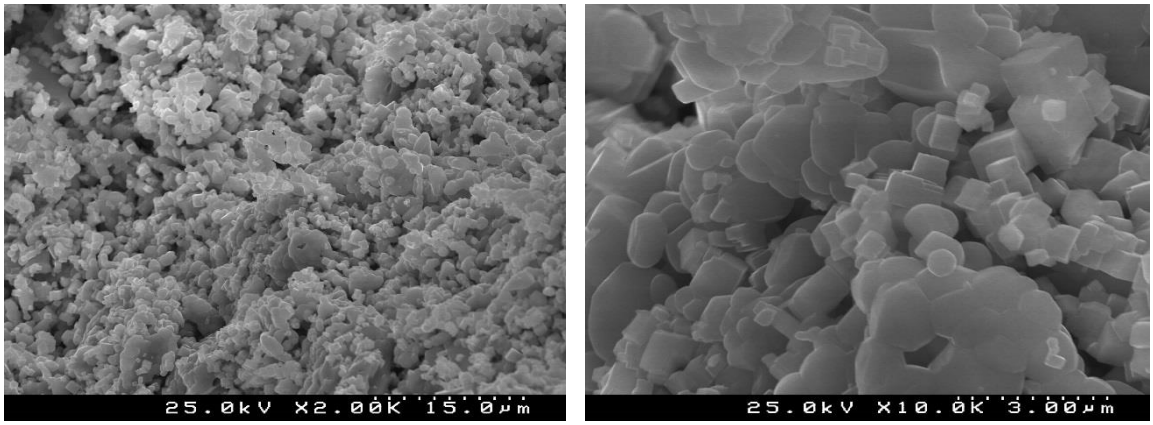

Figure 81: SEM images of SrM composites with 30% of KNN of citrates synthesis method, image in the left 2k magnification and the image in the right 10k magnification.

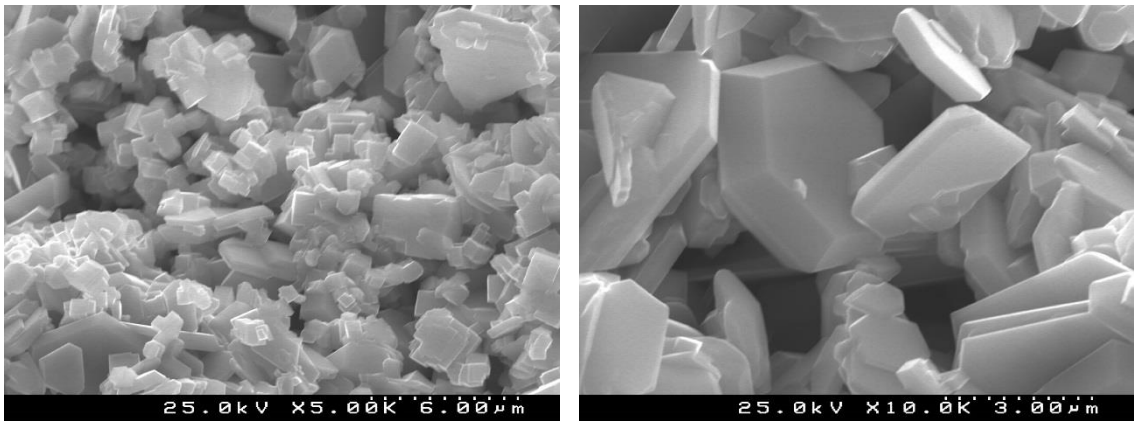

Figure 82: SEM images of BaZ composites with 30% of KNN of citrates synthesis method, image in the left 5k magnification and the image in the right 10k magnification.

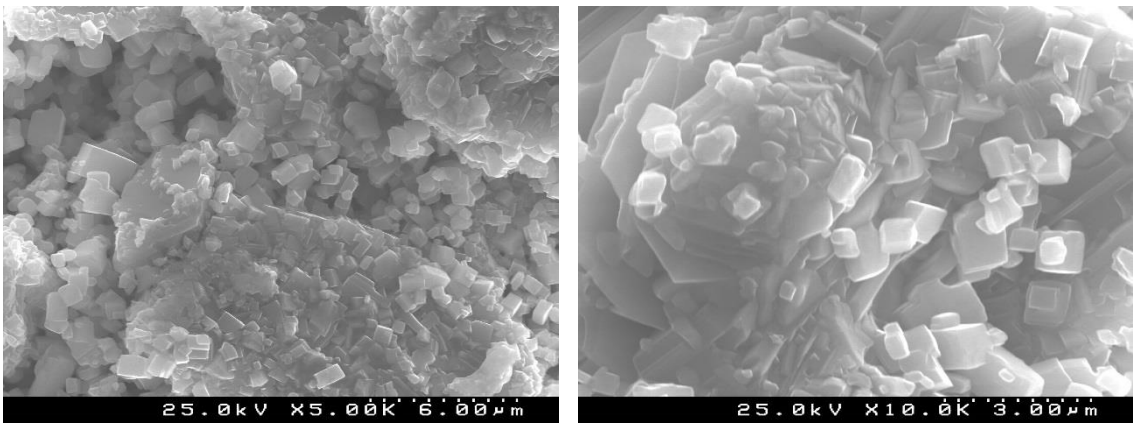

Figure 83: SEM images of SrZ composites with 30% of KNN of citrates synthesis method, image in the left 5k magnification and the image in the right 10k magnification.

The KNN composites of the citrates synthesis method provide SEM images with an easy detection of the grains shapes and their distribution.

The SEM images in the M-ferrites in figure 80 and 81, displayed a random distribution of grains, at higher magnification the shape of the grains becomes even more visible, some of the grains had cubic struture, these grains represents the ferroelectric phase of KNN, while like the BT composites the grains with hexagonal edges represent the hexagonal ferrites. The KNN grains have a more clearly cubic shape compared to the BT grains. The Z-ferrites, figure 82 and 83, display hexagonal grains with higher dimensions, and well very defined. They are also randomly distributed, there is no preferred direction in the composite. In figure 82 hexagonal grains are visible, is possible to visualise a hexagonal grain with a well-defined shape, and compared with the grains around it, it has bigger dimensions, It is also possible to see in these images the high porosity of the samples figure 81 and figure 82, mainly due to the distribution of the grains in the citrates method. In figure 83 the SrZ composite seems to be covered with the cubic grains of KNN, and this sample may promise to be a good candidate for future coupling measurements due the bond o ferroelectric phase and hexaferrites as possible to visualize in figure 83 the cubic grains covers the hexagonal grains.

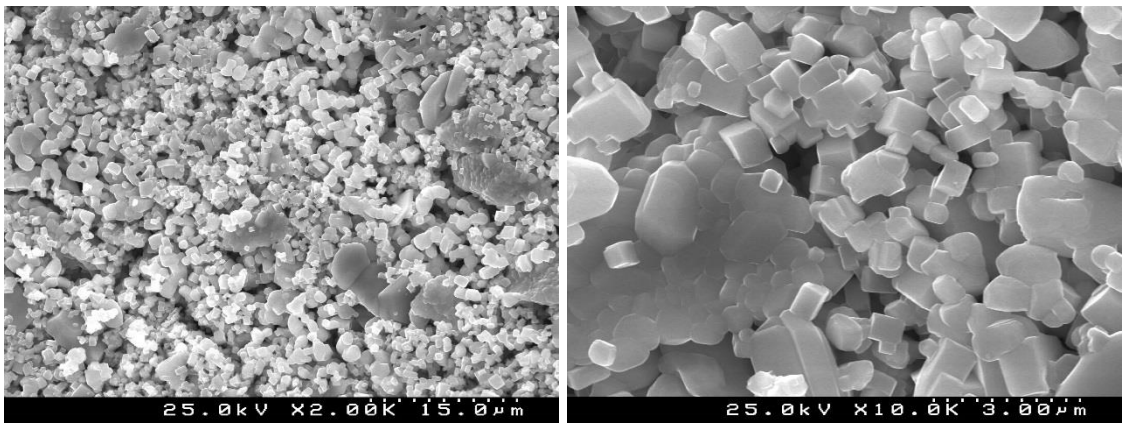

Figure 84: SEM images of BaM composites with 30% of KNN of sol-gel method, image in the left 2k magnification and the image in the right 10k magnification.

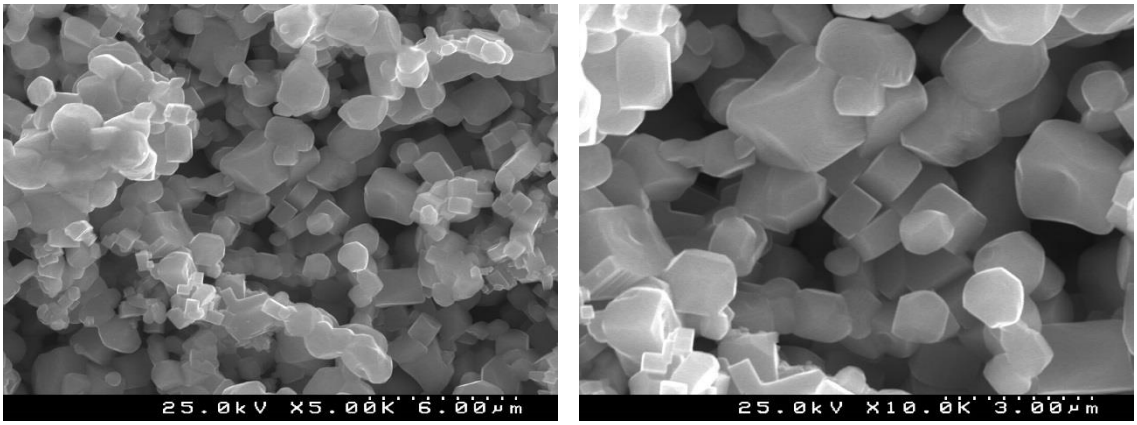

Figure 85: SEM images of SrM composites with 30% of KNN of sol-gel method, image in the left 5k magnification and the image in the right 10k magnification.

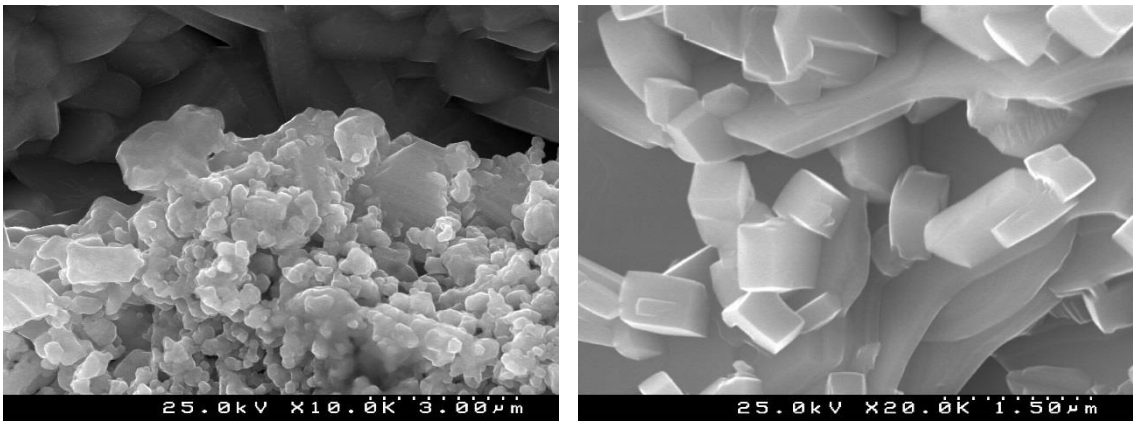

Figure 86: SEM images of BaZ composites with 30% of KNN of sol-gel method, image in the left 10k magnification and the image in the right 20k magnification.

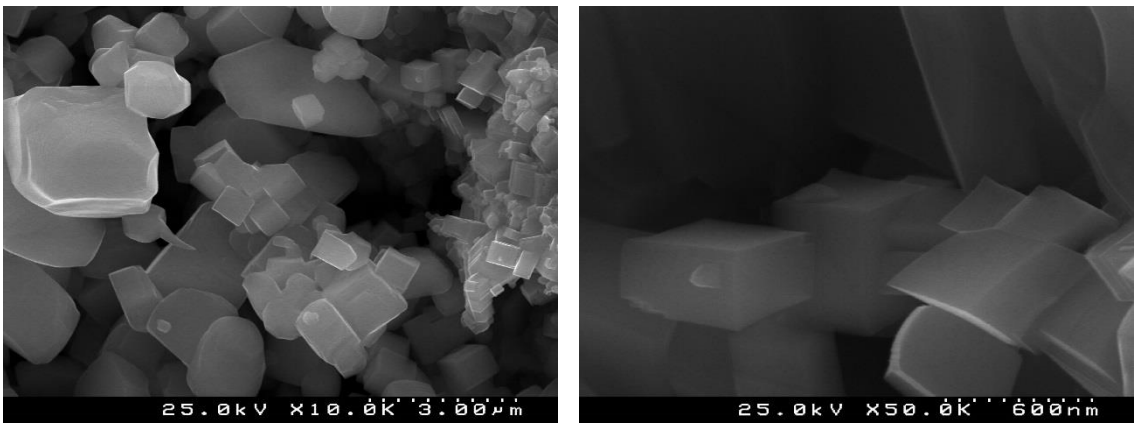

Figure 87: SEM images of SrZ composites with 30% of KNN of sol-gel method, image in the left 10k magnification and the image in the right 20k magnification.

The SEM images of KNN composites from the sol-gel method exhibit hexagonal grain shapes less visible than in citrates method due the formation of secondary phases as sowed in XRD measurements. In the SEM images of the BaM composite, figure 84, it is possible to visualize cubic

grains, and there are also some grains which resemble the hexagonal shape of M-ferrite, exhibiting hexagonal edges. In the image on the right of figure 84, some apparently different phases can be seen.

The SrM composite, in figure 85, displays a few very small hexagonal shaped grains of SrM ferrite, and some cubic grains can also be seen, although most of the grains did not have a defined shape. Because of their low size, it is not possible to determine which species of grains are present, and this composition didn't offer such good results, and in this these images are is in accordance with the XRD analysis.

The Z-ferrites exhibited better grain shapes in the SEM images, figures 86 and 87, and it is possible to visualize with great detail the cubic grains shapes of the KNN phase. Also there are some grains with hexagonal shape, and in figure 86 hexagon edges in profile are visible. The XRD analysis for this composition displayed a very low amount of hexaferrites phase, and this is generally confirmed by the SEM images. The method of sol-gel revealed a large amount of large scale porosity.

It was not possible to make SEM images of the other synthesis method, as it would require more time to prepare and analyse good samples. The methods of solid state reaction and sol-gel were chosen based on the XRD analysis and the density of the composites. The chosen methods provided different information about the composites porosity and phase formation, and the compositions with highest percentage of BT phase were chosen, to easily obtain the images of a ferroelectric phase. The methods of synthesis of KNN composites was chosen with the same presupposition.

4.4.PFM measurements

The PFM imaging and hysteresis loop acquisition were performed using a NT-MTD equipment with cantilevers of type NHCR, at aresonance frequency of 320 kHz, made of Si 42Nm^{-1}. The shape of the tip was a polygon-based pyramid with a radius of 12nm. We applied ac voltage of 10V at 50 kHz to obtain PFM response, and the piezoelectric loops were measured by the application of a dc voltage of ± 30V. For some composites it was not possible to make measurements due to the large roughness of the surface despite an intensive polishing, and to get a better result we used the samples that were pressed via CIP. Using AFM microscopy allows us to

make topography measurements on the samples with surface roughness less than 3 µm. In this case, the semi-contact mode has been used to make the measurements. During PFM measurements the voltage was applied to the bottom electrode of sample (made by silver paste), and the cantilever was grounded. Not all of the performed measurements will be discussed in this work, we chose only a few samples to illustrate the difference between the different methods of synthesis and different phase ratios.

The objective of the PFM measurements is to estimate piezoelectric and ferroelectric properties of the samples through the converse piezoelectric effect.

4.4.1. $BaTiO_3$

PFM measurements were performed on the BT composites. The samples prepared by solid state reaction and citrate synthesis methods have showed the largest piezoresponse, although some of the samples have showed large roughness which in some cases has been above the limit of the AFM scanner. The PFM response of the composites had showed a homogeneous distribution of the piezoelectric active phase throughout the materials. According to analysis made by XRD and SEM images the piezoresponse is more distinct in the composites with a larger amount of the ferroelectric phase, and the magnitude of the piezoelectric signal was estimated by application of ac voltage of 10V, which causes a displacement of the surface due to converse piezoelectric effect, and d_{33} component of the piezoelectric tensor can be calculated, (figures – B). The ferroelectric domains show a distinct evidence of both positive and negative PFM contrast. In the figure 88, a piezoelectric active response was estimated from a cross section line of the composites made by solid state reaction and citrates methods, and the highest piezoelectric response obtained was 12 pm/V. The other composites did shown the same response, and 3 samples were chosen to represent the PFM signal.

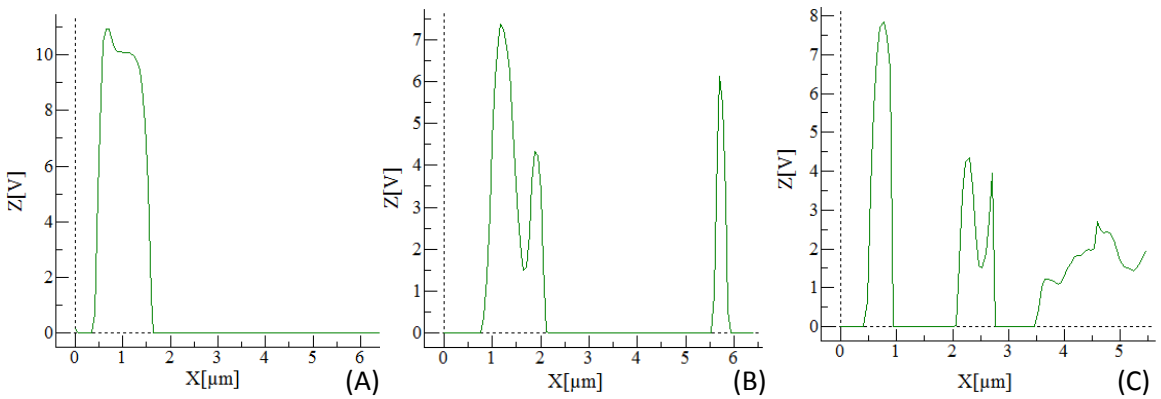

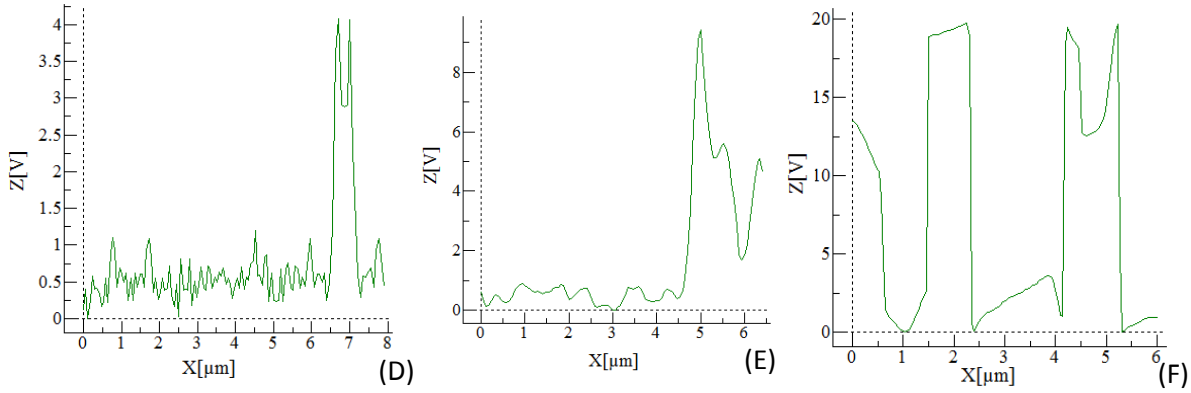

Figure 88: Piezoelectric response of cross section: A – BaM with 30% of BT, B - BaZ with 20% of BT, C - BaZ with 30% of BT and D - BaZ with 10% of BT all from solid state reaction, E – BaZ with 30% of BT and F – SrM with 30% of BT from citrates synthesis method.

The composition BaM with 30% of BT prepared by solid state reaction, figure 89-B, showed a better distribution of the piezoelectric phase than the composite BaZ of the same method and same quantity of ferroelectric phase figure 90-B. Also visible in figure 90-C is a some magnetic phase, possibly due the size of the grains of BaZ ferrite, and this composite shows a PFM magnitude lower than the BaM composite. With a decrease of the ferroelectric phase in the composites, in figure 91-B and 92-B the piezoelectric response should decrease, but in the case of the BaZ composite in the figure 91-B this does not happen due the presence of a small area of ferroelectric phase in the composite. The BaZ composite with 10% of BT, figure 92-B, showed a very low MFM amplitude and very little changes of phase. All the composites prepared by solid state reaction method had shown a considerable roughness.

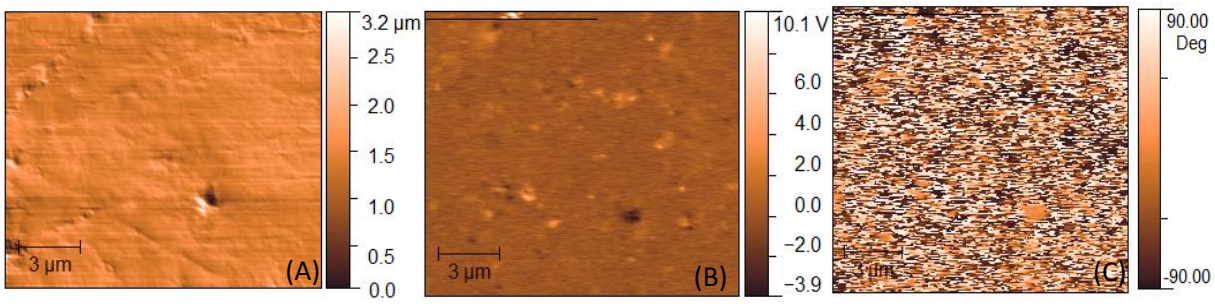

Figure 89: PFM images from composites of BaM with 30% of BT, made by solid state reaction, A – PFM topography, B – PFM magnitude, C – PFM phase.

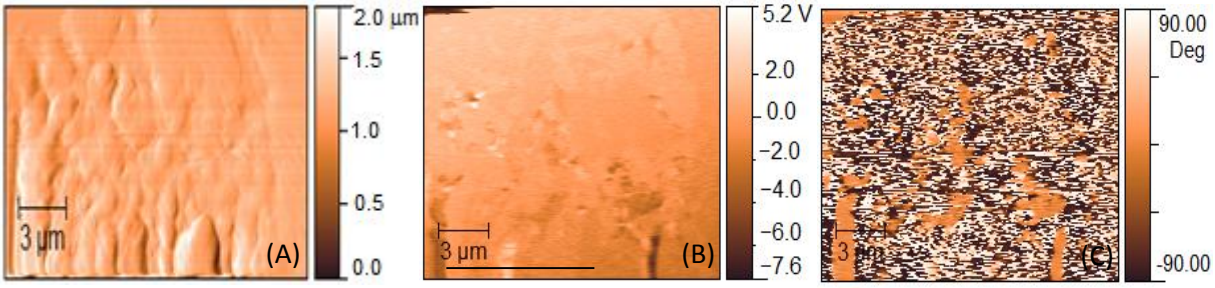

Figure 90: PFM images from composites of BaZ with 30% of BT, made by solid state reaction, A – PFM topography, B – PFM magnitude, C – PFM phase.

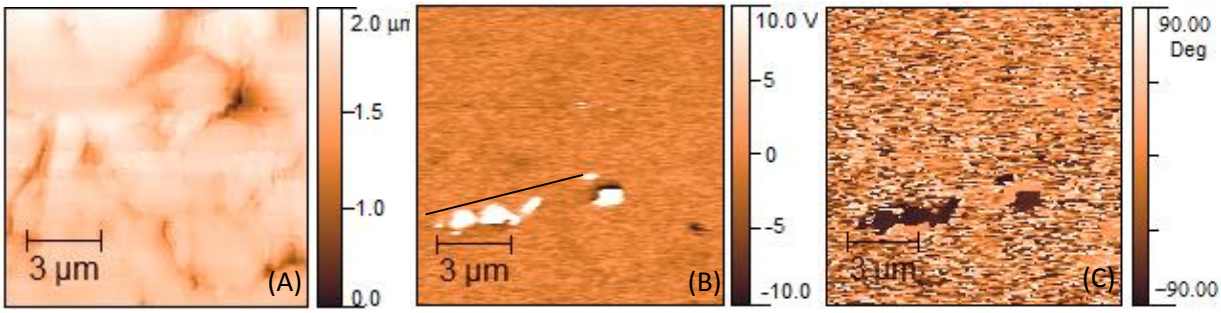

Figure 91: PFM images from composites of BaZ with 20% of BT, made by solid state reaction, A – PFM topography, B – PFM magnitude, C – PFM phase

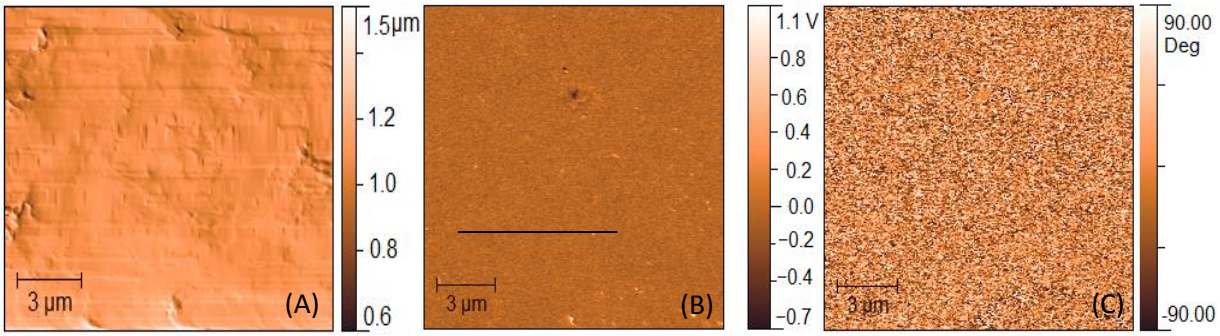

Figure 92: PFM from composites of BaZ with 10% of BT, made by solid state reaction, A – PFM topography, B – PFM magnitude, C – PFM phase.

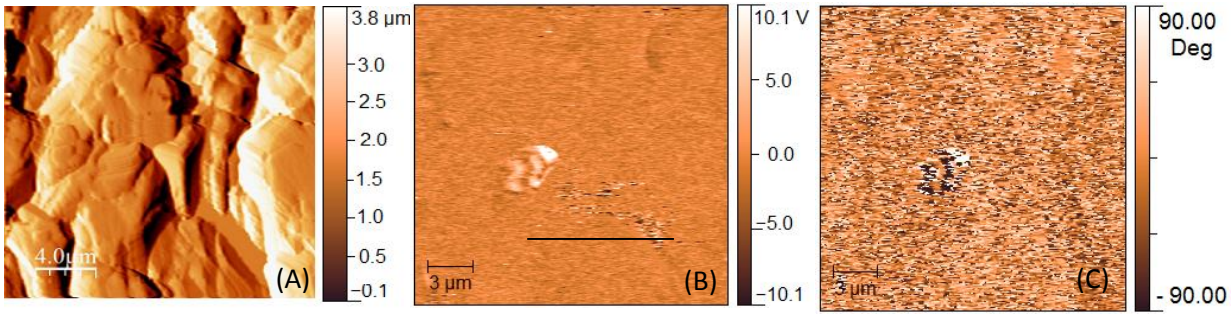

Figure 93: PFM from composites of BaZ with 30% of BT, made by citrates synthesis method, A – PFM topography, B – PFM magnitude, C – PFM phase.

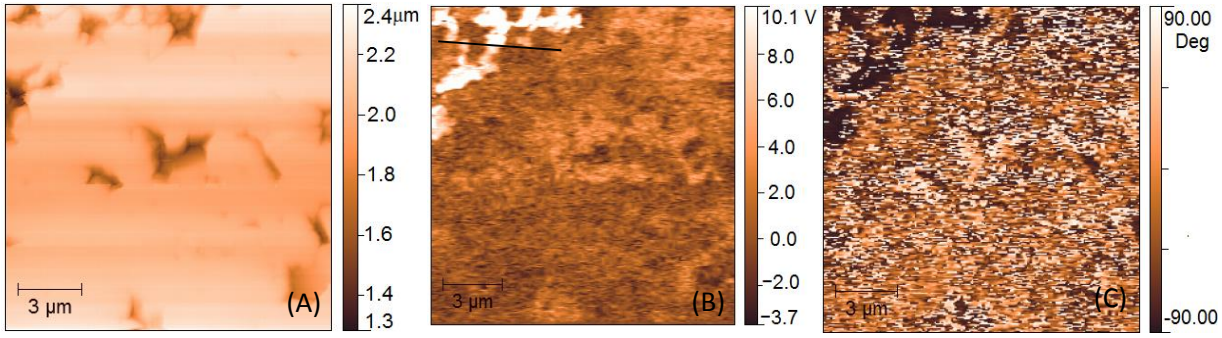

Figure 94: PFM from composites of SrM with 30% of BT, made by citrates synthesis method, A – PFM topography, B – PFM magnitude, C – PFM phase

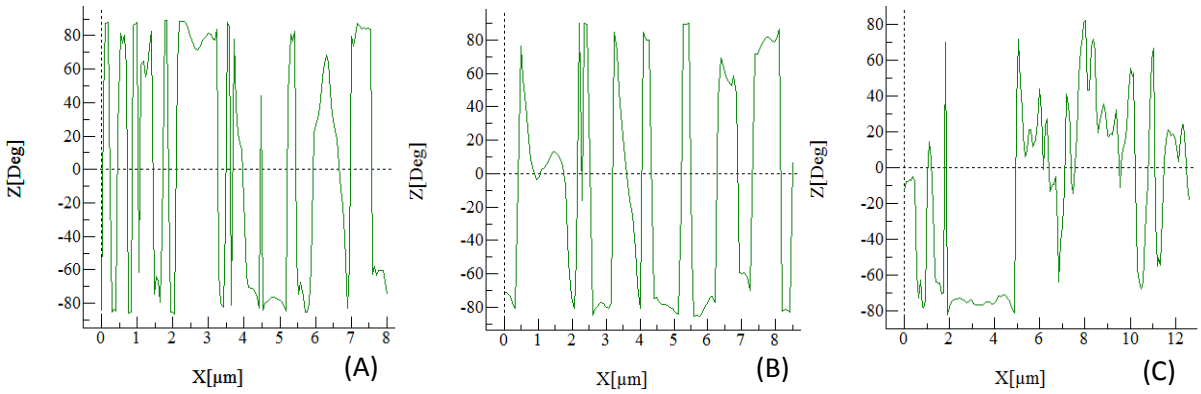

Figure 95: PFM phase of cross section: A – BaM with 30% of BT, B - BaZ with 20% of BT and C - BaZ with 30% of BT of the made by solid state reaction method.

Comparing the methods of citrates and solid state reaction, the BaZ composites with 30% of BT had a very distinct response. With the citrates method a higher MFM amplitude was obtained, and also visible is agglomeration of the ferroelectric phase, which is not homogenously distributed, as shown in figure 93-B, also happens in the SrM composite, figure 94.

The graphics in figure 95 showed that the composites had very active piezoresponse, the electrical field applied produced a response in the composites. Also in figure 95 we obtained the response from the ferroelectrics phases of some of the composites. These graphics are merely representative of what can be obtained when the applied field and the piezoelectric response has the same direction (in-phase) and the sample expanded. When the electrical field and the piezoelectric response have different directions (out-phase) the sample contracted.

4.4.2. KNN

The KNN composites showed a higher piezoelectric response compared whit the BT composites, and in this work the methods of citrates and sol-gel were analysed, as both methods had shown better samples for analysis. The operations conditions of PFM measurements were the same as described in BT composites.

The citrates synthesis method with KNN phase was shown to have a PFM magnitude lower than the composites of BT, although, by the analysis of the cross section in figure 102, it showed a high piezoelectric response to the applied field. The BaM composites, figure 95-B and figure 97-B have a more distinct ferroelectric phase than the composites of BaZ, figure 98-B and figure 99-B, and they also show a more homogenous distribution of ferroelectric phase. The PFM measurements of these composites confirm the distribution of the phases present in the composites, as do the cross sections of PFM phases. Comparing the BaZ composites with 30% of BT and KNN ferroelectric phase, they show some similarities, and both of them show some agglomeration of the ferroelectric phase.

The sol-gel method, in figure 100 and 101, was shown to have very low piezoelectric response in this measurements. Due to the small area scanned, 5 X 5 µm, it is possible to visualize some large grains and small grains, but it is not possible to determine if they are grains of hexaferrites and KNN, as the piezoelectric response was not distinct enough to make such observations. The PFM phase observed in these composites showed that a magnetic phase constituted the bulk of the sample, and this was confirmed by the analysis of the cross sections, figure 102.

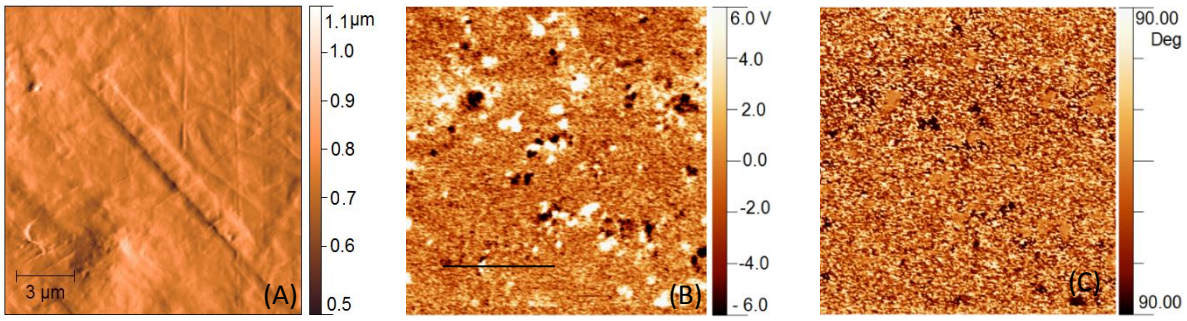

Figure 96: PFM images from composites of BaM with 30% of KNN, made by citrates synthesis method, A – PFM topography, B – PFM magnitude, C – PFM phase.

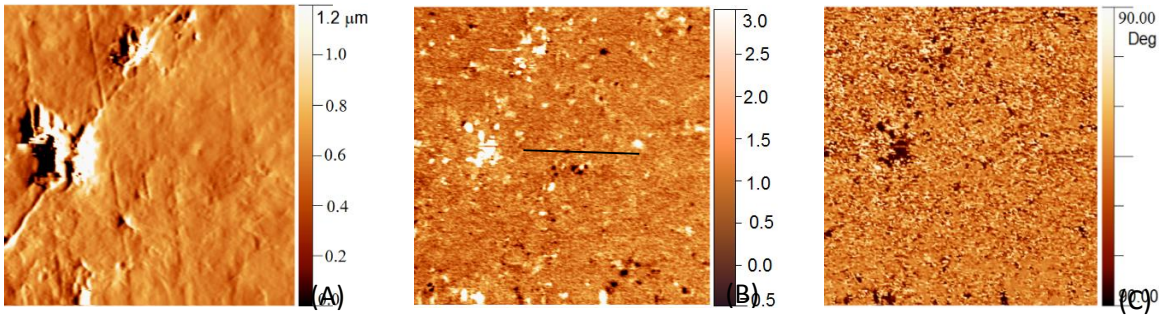

Figure 97: PFM images from composites of BaM with 20% of KNN, made by citrates synthesis method, A – PFM topography, B – PFM magnitude, C – PFM phase.

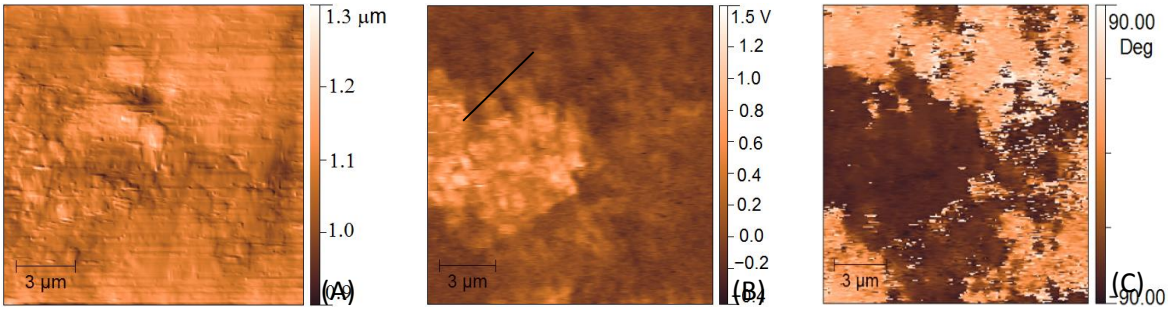

Figure 98: PFM images from composites of BaZ with 30% of KNN, made by citrates synthesis method A – PFM topography, B – PFM magnitude, C – PFM phase.

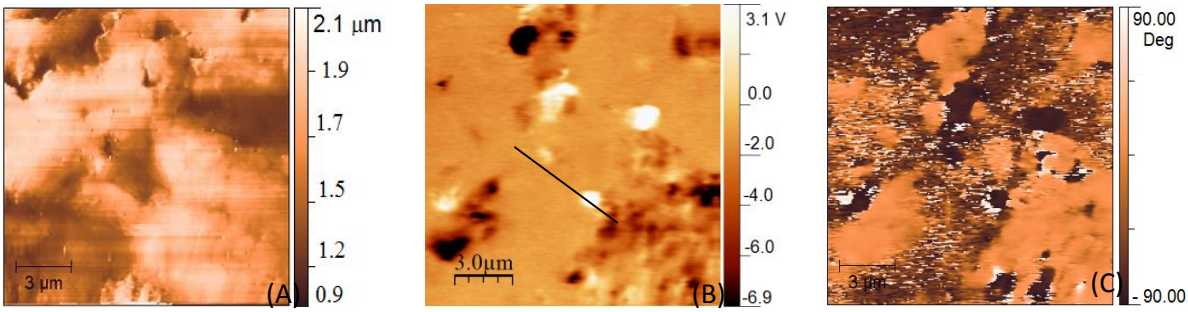

Figure 99: PFM images from composites of BaZ with 20% of KNN, made by citrates synthesis method A – PFM topography, B – PFM magnitude, C – PFM phase.

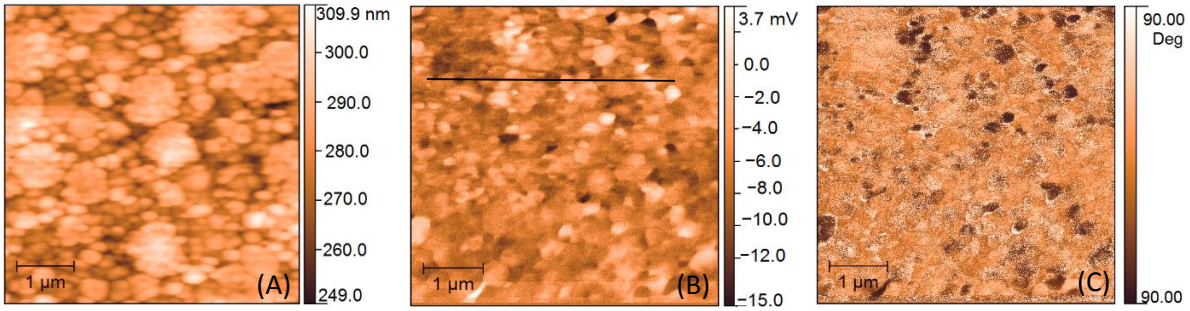

Figure 100: PFM images from composites of BaM with 30% of KNN, made by sol-gel method A – PFM topography, B – PFM magnitude, C – PFM phase.

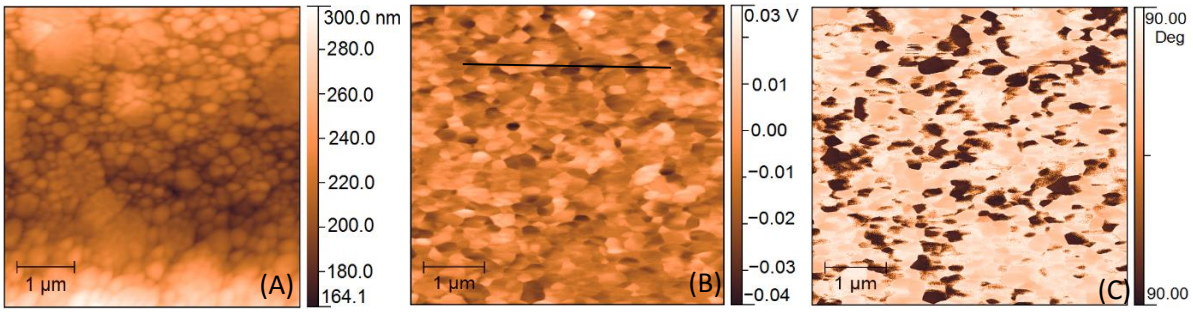

Figure 101: PFM images from composites of BaZ with 30% of KNN, made by sol-gel method A – PFM topography, B – PFM magnitude, C – PFM phase.

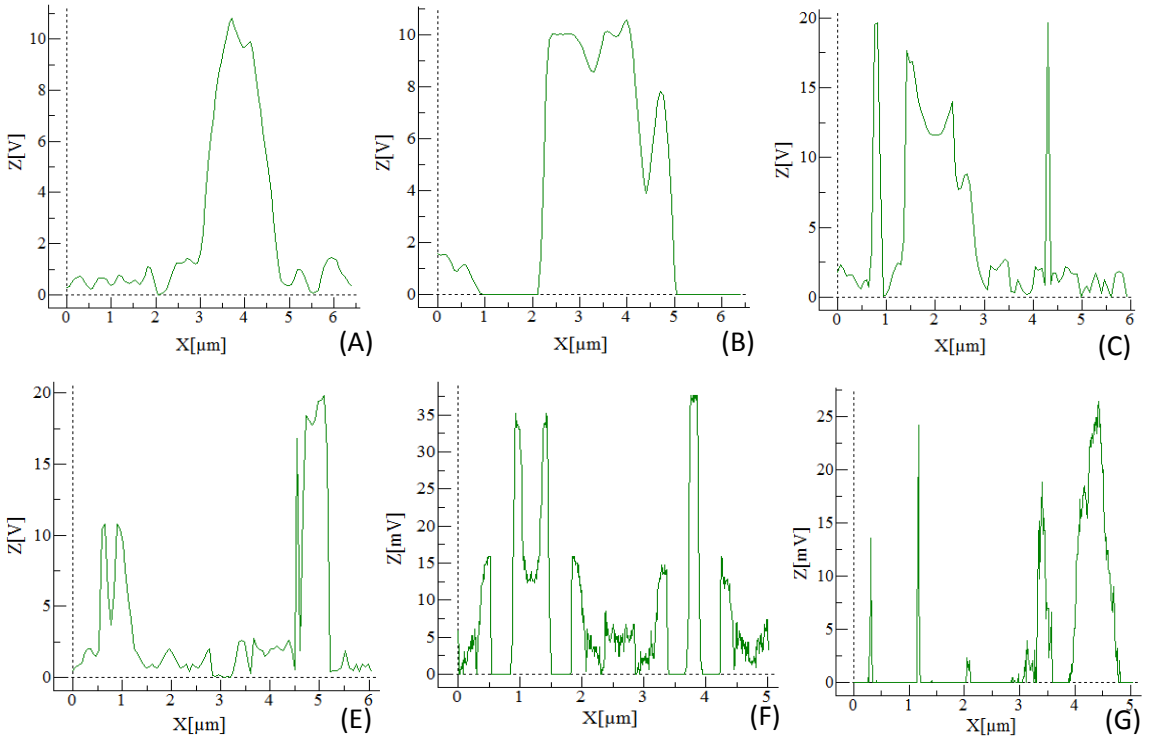

Figure 102: Piezoelectric response of cross section: A – BaM with 30% of KNN, B - BaM with 30% of BT, C - BaZ with 30% of BT and D - BaZ with 20% of KNN all from citrates synthesis method, E – BaM with 30% of KNN and F – BaZ with 30% of KNN from sol-gel method.

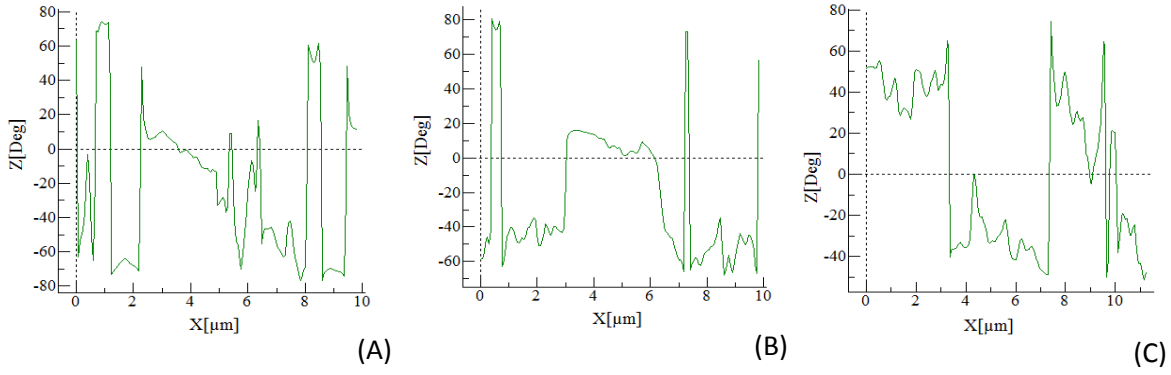

Figure 103: PFM phase of cross section: A – BaM with 20% of KNN, B - BaZ with 30% of KNN and C - BaZ with 20% of KNN of the made by citrates synthesis method.

4.5.Piezoelectric hysteresis loops

The hysteresis loops measurements were made in some of the composites, from those that had higher piezoelectric response, the PFM measurements above, served as filter to dedicate more time to the composites that will show better hysteresis loop due the lower conductivities of some of the composites.

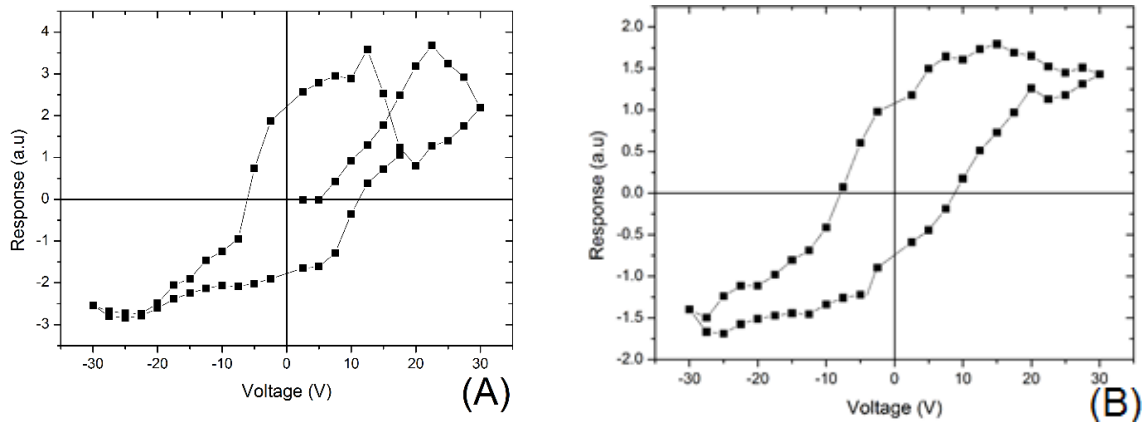

Figure 104: Hysteresis loops of BaM 70 - 30 BT - A and BaZ 80 - 20 BT - B, from solid state reaction method, with amplitude of 10V and frequency of 50 kHz.

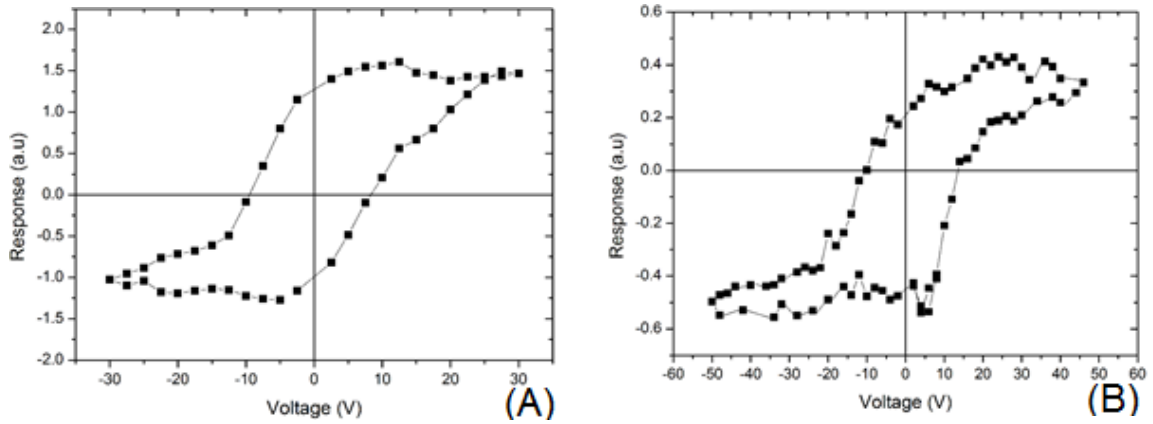

Figure 105: Hysteresis loops of composite of BaZ 70 - 30 KNN from citrates – A and SrM 70 – 30 BT from citrates synthesis method, with 10V amplitude at a frequency of 50 kHz.

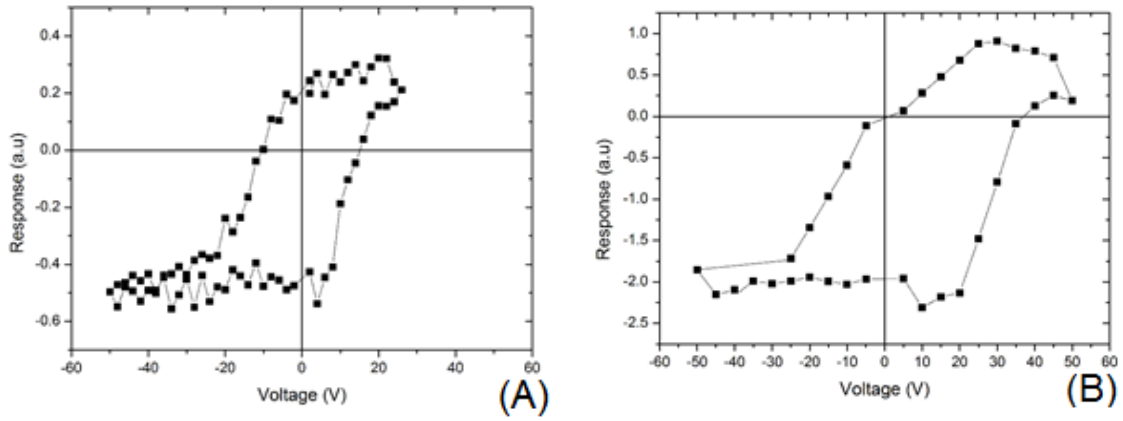

Figure 106: Hysteresis loops of composite of BaZ 70 - 20 KNN from the method of citrates – A and BaM 80 – 20 KNN from citrates synthesis method, with 10V amplitude at a frequency of 50 kHz.

The local piezoelectric hysteresis loops were achieved in different composites of different synthesis methods. The existence of ferroelectric P-E hysteresis loop real proves the ferroelectricity, since the piezoelectric tensor is related to the polarization. It was obtained information about the switching behaviour of the polarization, it was made by sweeping DC voltage from zero to positive and then to negative coercive voltage, measuring each point of piezoelectric response, therefore there will be a change in coefficient d_{33}.

The BaZ-BT composites of solid state reaction method (figure 104), had showed an hysteresis loops are almost in the centre of the axis, this means that there was not in presence of a conductive phase in the measurement although the piezoelectric response was low comparing with the literature existing for composites [111], these results show that there were domains capable of switching polarization. Also BaZ composite with 30% of KNN of citrates synthesis methods in figure 105-A, shown there a piezoelectric response when applied a sweep electrical field, there was a polarization with switchable domains, also was seen preferred domain orientation due the ferromagnetic phase the loop is dislocated in positive xx-axis. The loops in the figure 105-B, and figure 106 had a higher response in amplitude with negative DC voltage showing some permanent polarization in ferroelectric material.

Others composites were tested but most of them did shown an hysteresis loop due the low response of piezoelectric phase in some cases were absent, as previews mentioned not all composites result was good to make this kind of measurements.

4.6.MFM measurements

4.6.1. $BaTiO_3$

The MFM experiments performed during the study allowed to visualize magnetic domains structure of the compounds. The MFM measurements were carried out for the composites previously measured by PFM experiments.

The analysis of the MFM data allowed estimating the peculiarities of the domain magnetic structure in composites visualized to perform comparative analysis of the magnetic response in the composites prepared by different methods and with different ratio of the magnetic phase. The MFM data graphically show magnetically active phase of the composites and allow estimating a phase ratio of the composites.

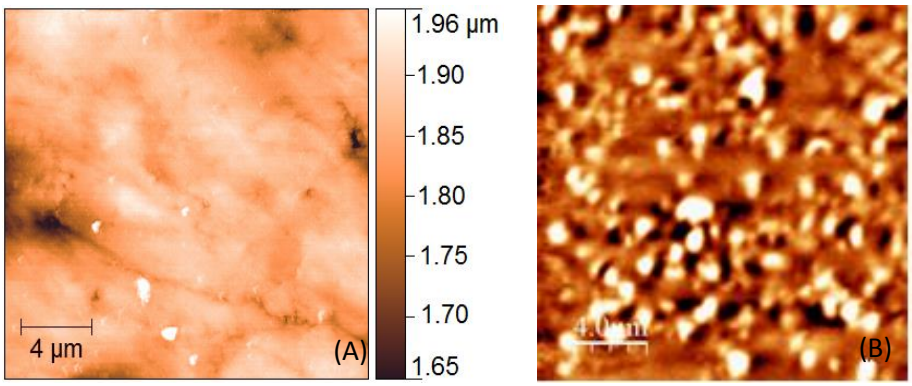

Figure 107: MFM measurement: A - Topography, B - magnetic response from BaM composite with 30% of BT, solid state reaction method.

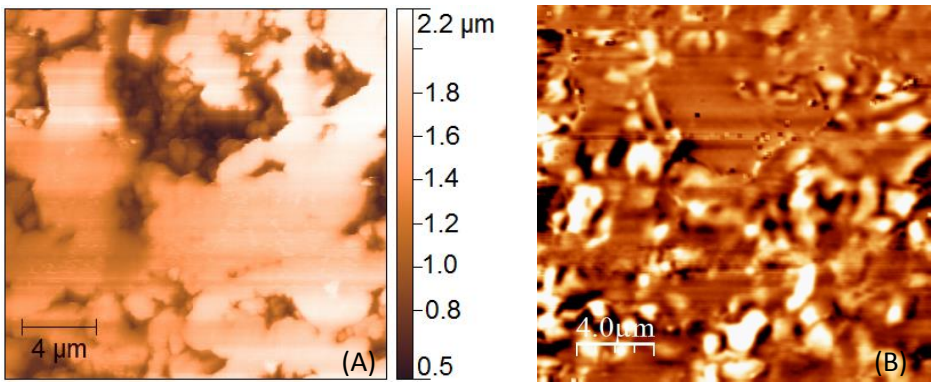

Figure 108: MFM measurement: A - Topography, B - magnetic response from BaZ composite with 30% of BT, solid state reaction method.

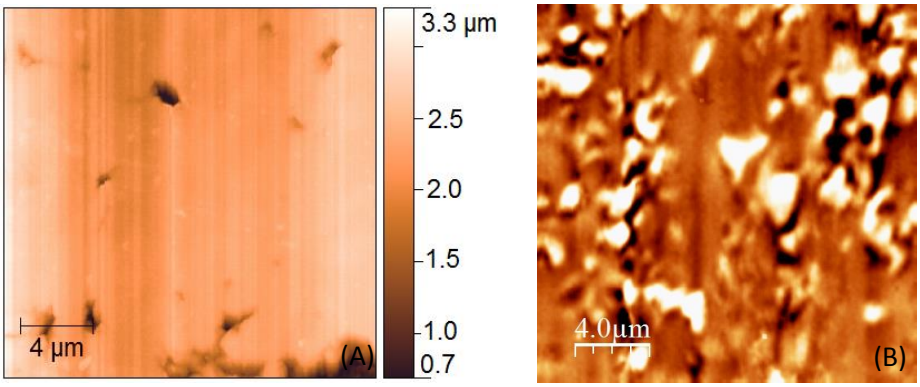

Figure 109: MFM measurements of: A - Topography, B - Magnetic response of BaZ composites with 20% of BT, C- Topography and D – Magnetic response of BaM composites with 20% of BT, solid state reaction method.

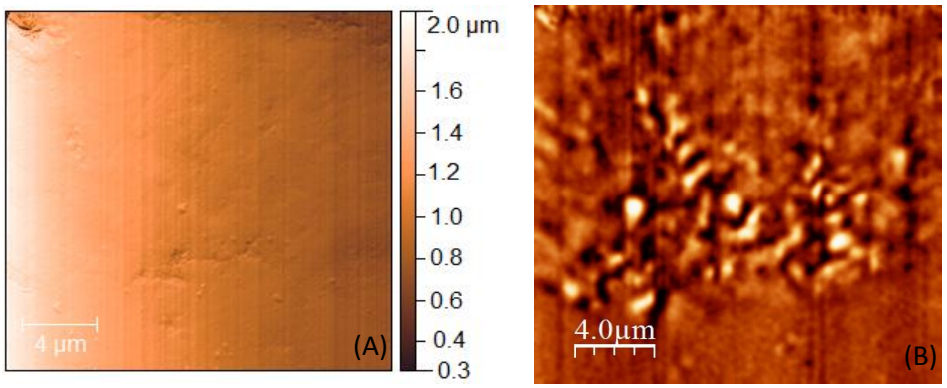

Figure 110: MFM measurement: A - Topography, B - magnetic response from BaZ composite with 30% of BT, citrates synthesis method.

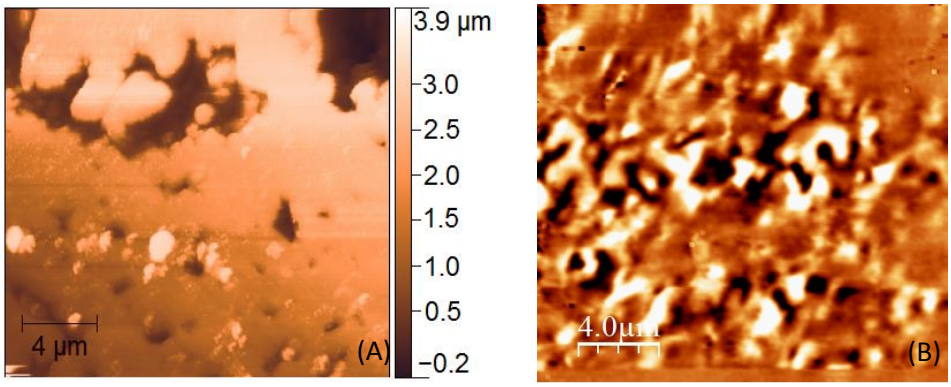

Figure 111: MFM measurement: A - Topography, B - magnetic response from SrM composite with 30% of BT, citrates synthesis method.

The MFM data of BT composites prepared by both methods - solid state reaction and citrate synthesis show the magnetic domains of the composites, the domains have randomly oriented distribution which is typical for magnetic materials without magnetic history.

MFM data of BaM from solid state reaction with BT (figure 107-B) testify that the domains have a round shape with average size lower than 4 μm, the domain wall has a reduced thickness due to the proximity of the domains, also it can be visualized in the image B a presence of areas without any contrast the areas may be caused by magnetic phase with low magnetic response or by the piezoelectric phase, the majority phase is magnetic.

The MFM data of BaZ composite with 30% of BT, figure 108-B displayed large size domains with about 4μm length, asymmetrically distributed, compared with the BaM composite (figure 107-B). The irregular topography of the sample could explain the absence of domains (bright spots) in some areas. With decrease of the piezoelectric phase (20% of BT) and the increase of the magnetic phase, is displayed less contrast in the analysed area, figure 109-B, therefor less domains are visible as the consequence the domains walls have larger thickness, the distribution of the domains is not random throughout the obtained image. The domains in this composites had different geometry shape some of the domains exhibited sizeable dimensions of 4μm length. In the figures 110 and 111 it showed the composites of BaZ of the method of citrate synthesis, these composites exhibited areas with magnetic phase displaying a small amount of the domains across the analysed area. The domains are preferred located in some areas, with reduce distance between them, this makes the domain wall thicker, also the domains showed to have a smaller size approximately 1μm in length, the shape of the domains with higher intensity are circular, comparing with the BaZ composite in figure 108, this composite had shown low MFM measurements, low density contrast across the surface. The SrM composite with 30% of BT from citrates method, figure 111, shows domains randomly orientated, with a homogenous distribution in the analysed area, the domains have irregular geometry. It was visible a domain with the shape of “S”, also the domains have different length it was estimated 4 μm in some of the domains.

The composites with larger amount of the BT phase show more distinct domain structure what confirms the magnetic response for the composition.

4.6.2. KNN

The KNN composites had showed a better response to the MFM analysis, the domains in the KNN composites had an ample density distribution across the surface of the samples, was also possible to visualize a regular geometry.

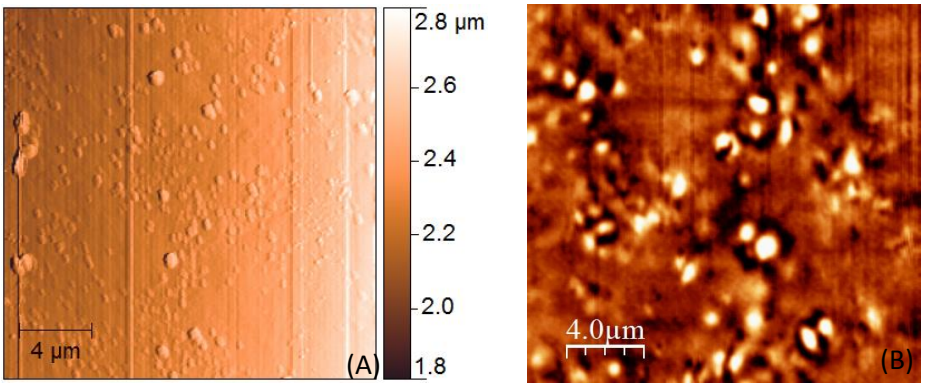

Figure 112: MFM measurement: A - Topography, B - magnetic response from BaM composite with 30% of KNN, citrates synthesis method.

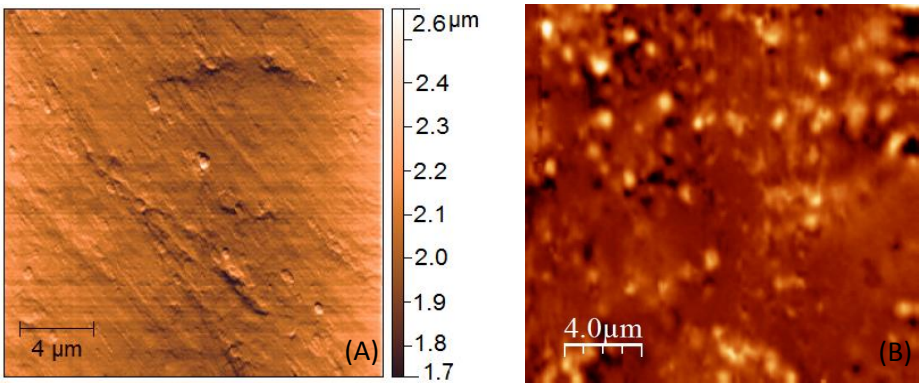

Figure 113: MFM measurement: A - Topography, B - magnetic response from BaM composite with 20% of KNN, citrates synthesis method.

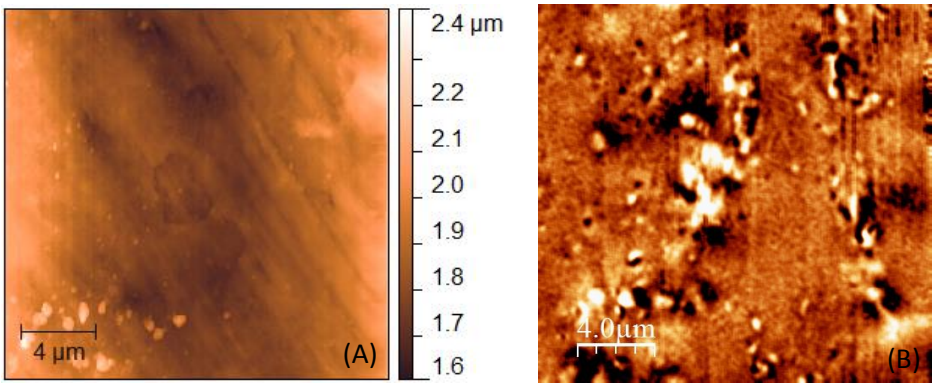

Figure 114: MFM measurement: A - Topography, B - magnetic response from BaZ composite with 30% of KNN, citrates synthesis method

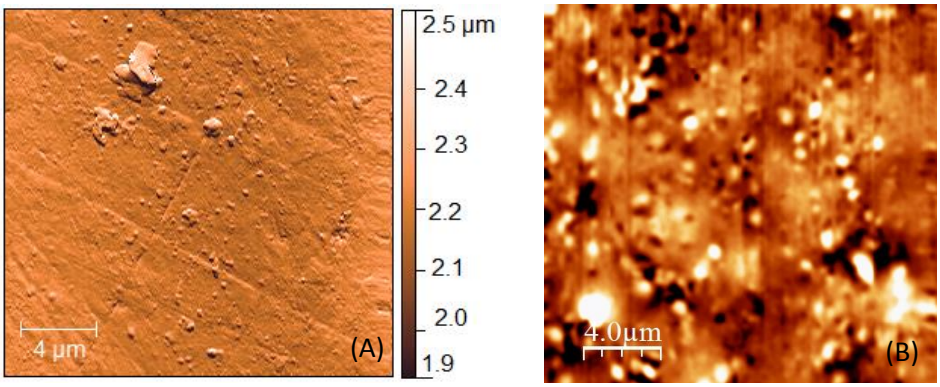

Figure 115: MFM measurement: A - Topography, B - magnetic response from BaZ composite with 20% of KNN, citrates synthesis method

The MFM image of the composite BAM with 30% of KNN, figure 112 had showed a random distribution of domains, the domains have a circular geometry, with the diameter inferior of 2 µm, with a lower percentage of KNN the BaM composite (figure 113-B) had shown less domains across the surface, is possible to visualise some areas without bright spots, the domains had a round shape with a diameter smaller than that of the BaM composite with 30% of KNN.

The BaZ composites, figure 114 and 115 exhibited a distinct contrast in the MFM measurements, higher than of the BT composites, both of the composites also show a homogenous distribution, the domains walls are a very thick compared with those of the BT composites of the same composition, the geometry of the domains in are circular with an estimated diameter of 2 µm in the composite with 20% of KNN, in the composite of the figure 116-B is difficult estimated due the variations of size of the domains, the highest also is 2 µm the estimation was made through the scale of the images.

The MFM mapping allows visualization of the shape of the magnetic domains and magnetic domain distribution. The magnetic domains were mainly randomly distributed across the surface of the samples making isotropic resulting magnetization as shown in the figures above, whereas piezoelectric phase homogeneously distributed throughout the composites the thickness of the magnetic domain walls estimated based on the MFM data is in accordance with the previous data [103].

4.7.VSM measurements

The VSM measurements provides information about the magnetic response of the composites, with this measurements was possible to determinate the magnetic saturation, magnetic remanent and coercive field. It was made analysis of the composites with 90% of ferromagnetic phase from all methods of KNN and sol-gel and solid state reaction from BT composites, all hysteresis loops in figures below by applying a magnetising force of 3 tesla.

4.7.1. $BaTiO_3$

The analysis of VSM did permit a study of the magnetic properties of the composites, in the BT composites was only possible to obtain results from solid state reaction and sol-gel due the malfunction of VSM. The composites of Z-ferrites with BT from sol-gel shown a higher response in the magnetic measurements, the hysteresis loop of the composites BaZ ferrite shown in figure 117 had a higher saturation magnetisation (60.6 emu/g), but did shown a lower coercive force and remanent magnetisation compared with the SrZ composite of the method of sol-gel (table 9). The M-ferrites shown different results of magnetic measurements in the two methods of synthesis, the BaM had a higher saturation response in the method of sol-gel, but a lower response in coercive force and remanent magnetisation compared with the solid state reaction synthesis method. The higher results obtained in the composites of hexaferrites with 10% of BT was achieved with the SrM hexaferrites of the solid state reaction synthesis method had a saturation magnetisation of 65.2 emu/g, all of composites had a similar M_s response only the M_r and H_c was lower in the Z-ferrites, because they are soft materials very easily demagnetised

The SrZ composite of solid state reaction synthesis method had the lowest M_r and the lowest H_c. According with the existing literature. The composites of BT with hexaferrites had a similar response to the pure hexaferrites but with lower response value.

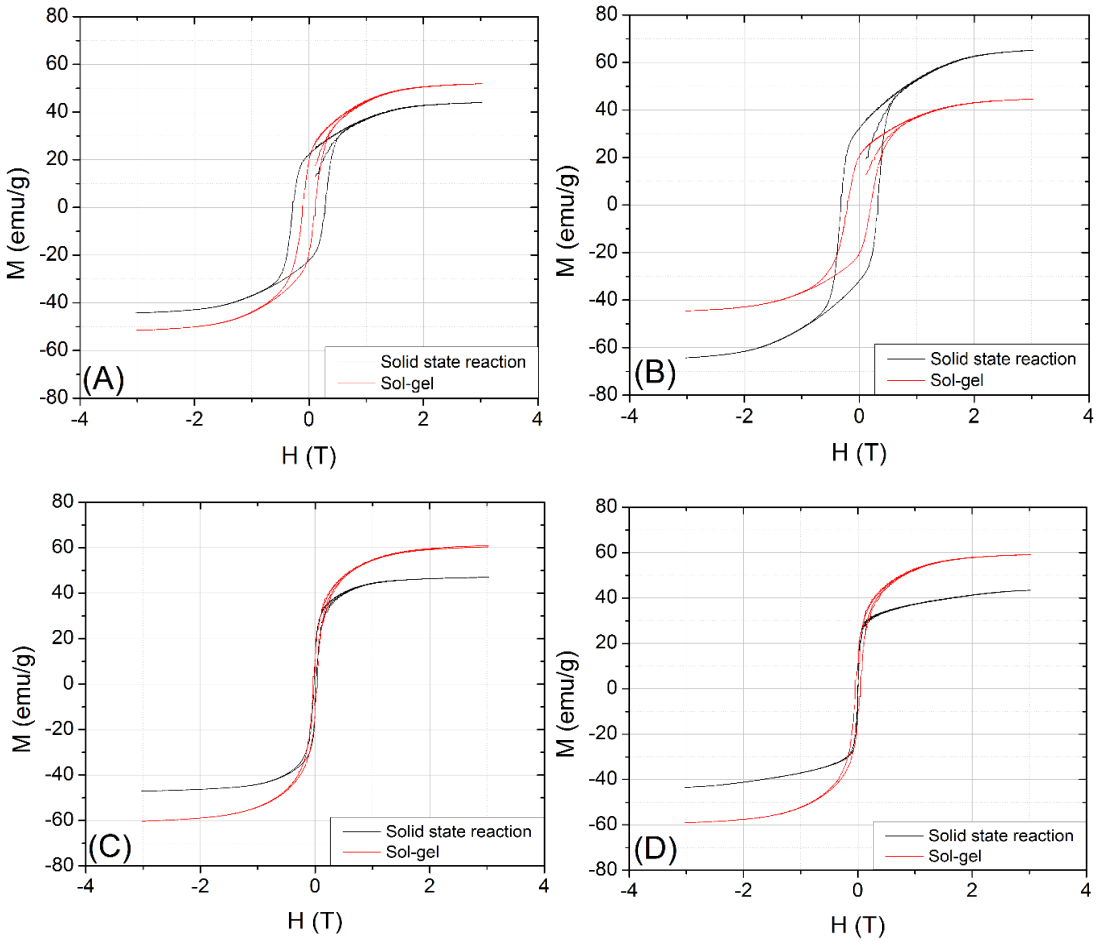

Figure 116: hysteresis loop of: BaM composites - A, SrM composites - B, BaZ composites – C, SrZ composites - D of the methods solid state reaction - black line, and sol-gel red line.

Table 12: Measurements of: saturated magnetisation (Ms), coercive force (Hc) and remanence magnetisation (Mr) of BT composites from the methods of solid state reaction and sol-gel, pressed via cold isotactic pressure.

Solid state reaction				Sol-gel			
Compositions %	M_s (emu/g)	H_c (mT)	M_r (emu/g)	Compositions %	M_s (emu/g)	H_c (mT)	M_r (emu/g)
BaM 90 - 10 BT	44	283	22	BaM 90 - 10 BT	51.8	115	18.7
SrM 90 -10 BT	65.2	329	32	SrM 90 -10 BT	44.6	210	20.3
BaZ 90 -10 BT	47	22	7.5	BaZ 90 -10 BT	60.6	36	10.7
SrZ 90 - 10 BT	43.4	5	1.7	SrZ 90 - 10 BT	59.14	44	11.3

4.7.2. KNN

The KNN composites had shown some higher M_s in some composites but in general a low M_r compared with BT composites, by the analysis of the hysteresis loop in the figure 117 and the table 10 was possible to determinate also the magnetic response. The method of solid state reaction and

citrates synthesis shown the better results for M_s figure 117, it was achieved a highest response, 65.1 emu/g, in SrM composite of solid state reaction synthesis method, also in this method the BaM composite achieved the better M_s 63.3 emu/g. In the coprecipitation and sol-gel methods the SrM-ferrite had a weak response 3.02 and 9.5 emu/g respectively, one explanation for this to happen is related to the presence of secondary phases in the composite, in the XRD was possible to view there was present of secondary phases with high intensities peaks, this can affect the magnetisation of the samples. The Z-ferrites had an M_s response lower then M-ferrites, the magnetic soft materials have M_sT lower than the magnetic hard material, In case of SrZ it had a lowest M_s in coprecipitation method 17.2 emu/g.

The residual *B* field M_r is higher in M-ferrite also the highest response was 31.5 emu/g, in the BaM composite of the citrate methods, is half of the saturated magnetisation, half of the dipoles are still orientated, a possible explanation is that there is an strong resistance of the domain walls in response to the increase of the magnetic field in opposite direction. Comparing the results of M_r the M-ferrites showed to have higher residual field compared with the Z-ferrites in all methods and between the methods the citrates synthesis methods had more residual field in the composites then the others composites from other methods with the exception of SrZ that had a highes t value 8.14 emu/g in sol-gel method.

Table 13: Measurements of: saturated magnetisation (Ms), coercive force (Hc) and remanence magnetisation (Mr) of KNN composites from the methods of solid state reaction and sol-gel, pressed via cold isotactic pressure.

Sol-gel			
Compositions %	M_s (emu/g)	H_c (mT)	M_r (emu/g)
BaM 90 - 10 KNN	32.8	221	13.8
SrM 90 -10 KNN	9.5	173	4.5
BaZ 90 -10 KNN	41.4	29	5.58
SrZ 90 - 10 KNN	36.8	50	8.14

Solid state reaction			
Compositions %	M_s (emu/g)	H_c (mT)	M_r (emu/g)
BaM 90 - 10 KNN	63.3	338	31.3
SrM 90 -10 KNN	65.1	322	25.8
BaZ 90 -10 KNN	53.1	41	6.8
SrZ 90 - 10 KNN	43.4	41	2.3

Citrates			
Compositions %	M_s (emu/g)	H_c (mT)	M_r (emu/g)
BaM 90 - 10 KNN	63.3	353	31.5
SrM 90 -10 KNN	62.9	333	31.3
BaZ 90 -10 KNN	53.3	36	7.9
SrZ 90 - 10 KNN	49.8	24	6

Coprecipitation			
Compositions %	M_s (emu/g)	H_c (mT)	M_r (emu/g)
BaM 90 - 10 KNN	28.9	336	14.1
SrM 90 -10 KNN	3.02	273	0.4
BaZ 90 -10 KNN	39.7	15	4.8
SrZ 90 - 10 KNN	17.2	74	3

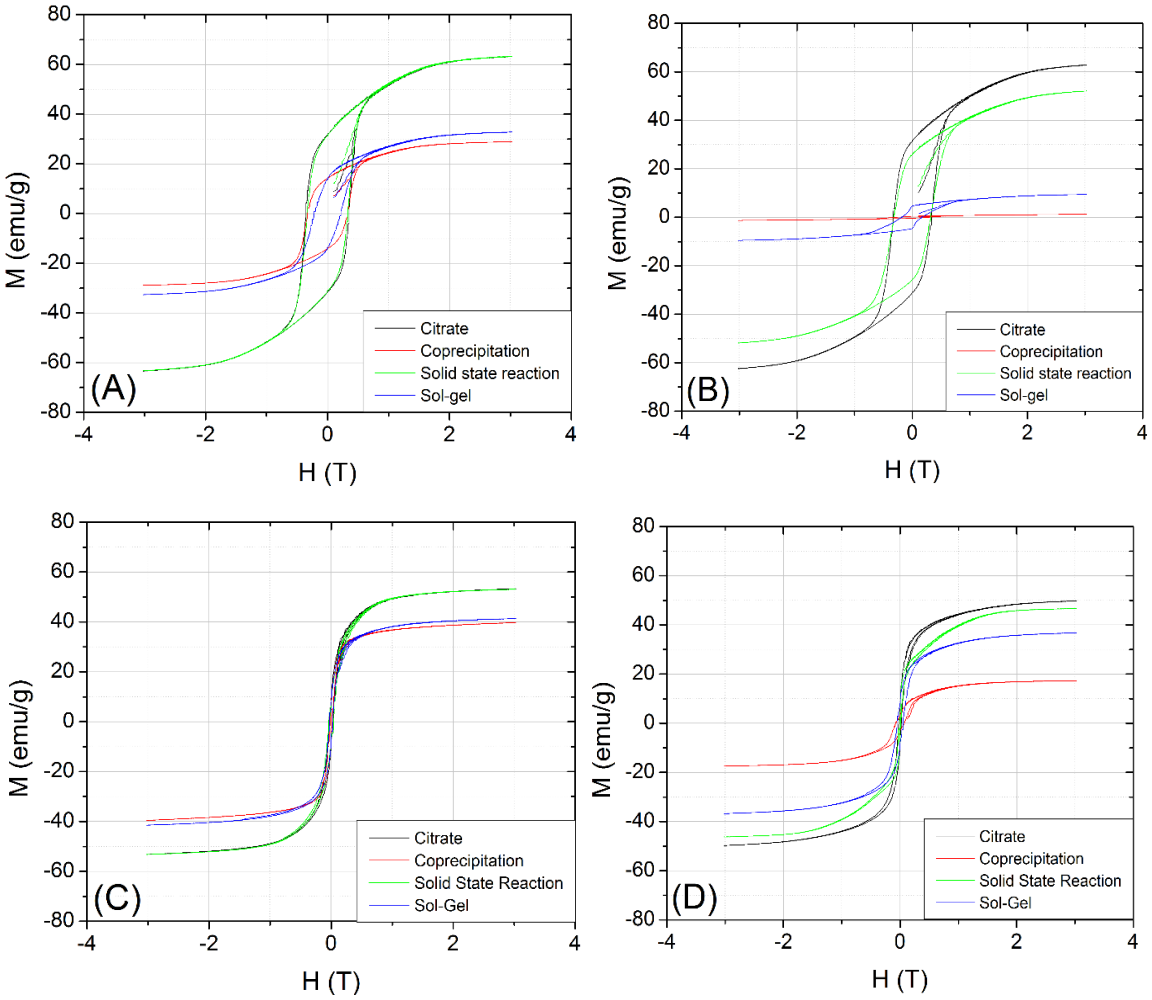

Figure 117: hysteresis loop of: KNN composites, BaM composites - A, SrM composites - B, BaZ composites – C, SrZ composites - D of the methods: citrates - black line, and coprecipitation - red line, solid state reaction – green line and sol-gel – purple line.

The composites of BT and KNN showed that they have a magnetic response in the presence of an external magnetic field, the magnetisation response occurred in the easy axis direction, c-axis, it is showed that the composites are magnetically anisotropic. Also the composites with M-ferrites showed high coercivity this mean that this composites are hard to demagnetize, they have high magnetic anisotropy, for this reason they are called hard ferromagnetic materials, the Z-ferrites have showed a very low coercive force.

The result obtained in the VSM was to characterize the magnetic response in the composites, the piezoelectric phase had a small contribution in this composites, only the presence of the secondary phases result in the difference of magnetic response. This results are related to the synthesis process of the hexaferrites and the sintering of the composites it can be confirmed with the XRD measurements of composites.

5. Conclusion and further work

In this work we studied the structure, microstructure, density, piezoelectric and magnetic responses of composite materials, based on hexagonal ferrites of M-type ($BaFe_{12}O_{19}$, $SrFe_{12}O_{19}$) and Z type ($Ba_3Co_2Fe_{24}O_{41}$, $Sr_3Co_2Fe_{24}O_{41}$), and perovskite piezoelectric materials ($BaTiO_3$, KNN).

The composites had a large range of densities, the cold isotactic pressure had shown to be more efficient, as these composites had a better density then in the uniaxial pressure. The method of citrates shown better results for the composites of BT, for the KNN composites in general the method of coprecipitation had the higher densities, also the BaM composites showed better densities compared with the other ferrites.

SEM images gave information about the structure of the grains, and it was possible to visualize the hexagonal ferrites and the cubic structure of BT and particularly KNN.

The Z-hexaferrites where shown to have a bigger grain structure then the M-ferrites, and the grains of the composites had a random orientation. The shape of the M-ferrites was different - the grains were more elongated in the Z-ferrites.

With the XRD was possible to identify the phases of the composites, in the hexaferrites calcinations was obtained the expected phases for most of the composites, but the sol-gel method did shown more secondary phases, and some of the ferrites contained large amount of hematite. In the XRD of BT composites the method of solid state reaction and citrates showed less secondary phases in the M-ferrites, but there is a formation of new phases such as $SrTiO_3$. In the Z-ferrites pure phases were not obtained, and with some methods diffusion of atoms occurred between the phases. In the KNN composites better results were achieved in M-ferrites, especially in citrates synthesis methods, as there were no secondary phases. In the Z-ferrites there was some diffusion in the SrZ composites, forming new phases sodium-strontium-niobate, strontium cobalt oxide and strontium-iron-niobate. From the calculated density, XRD and SEM images, some samples were chosen for other measurements.

The PFM and MFM showed the coupling topography of the samples. They had high roughness, and in the composites with BT it was only possible to acquire results from the composites with 20% and 30% BT. Some of them had a very low piezoelectric response in the order of 30 µV. With KNN the results were much better, there was high piezoelectric response of 120 µV. Not all composites had a detectable piezoelectric response, and the MFM images showed the magnetic domains and magnetic anisotropy.

In the VSM measurements was obtained the saturation magnetisation, the remanent magnetisation and the coercivity of the composites of BT and of KNN. The M-ferrites showed to had a high response to the applied field, and the SrM ferrite of the method of solid state reaction had a higher M_s response in the both composites (BT and KNN) of around 65 emu/g. The M_r was also higher in the M-ferrites - in the BT composites the highest value obtained was from SrM ferrite with 32 emu/g, and from the KNN composites was BaM ferrite of citrate combustion method 31.5 emu/g. Also it was the M-ferrites that had a higher coervicity, 329 mT in SrM ferrite of solid state reaction for the BT composites and the 353 mT for the BaM ferrite of citrate combustion method. The Z-ferrites showed lower response in the saturation magnetisation and coactivity then M-ferrites, the best results for M_s was in the BT composites was BaZ ferrite of sol-gel method with a response of 60.6 emu/g and for the KNN composites was also the BaZ ferrite but from citrates combustion method 53.3 emu/g. The composite SrZ ferrites with BT of the method sol-gel had a higher coercive force and remanent magnetisation. In the KNN composites it was also the SrZ ferrite that had a higher coercive force in the method of coprecipitation and the same composition had a higher remanent magnetisation but in sol-gel method.

The composites had different response to the different measurements made, the solid state reaction and the citrates are very promising methods to fabricate composites of hexaferrites and piezoelectric materials (BT and KNN), also in this work was seen that the better results of coupling was seen with higher amounts of piezoelectric phases (30%).

5.1. Future work

The study of the hexaferrites and composites with piezoelectric materials is not concluded, there is a need to make some more studies such as in strontium Z-ferrite, to better understand the single phase formation by trying different stages of temperature and different steps of heating. In the barium Z-ferrite it is also needed to make more studies in order to obtain a more pure phase.

In the composites is possible to achieve better densities. It is very important to decrease the porosity of the pellets, this will influence the piezoelectric and ferroelectric response of the material, the increase of the density could be achieve by a higher uniaxial pressure or/and making hot isotactic pressure (HIP).

The ME coupling in this work was studied, but there is much more scope to make further studies such as obtaining dielectric response, and to make PFM/MFM measurements in same place

of the samples. There is also a need to control the diffusion of atoms in the composites to obtain more distinct phases, by mixing the compounds even better to for the hexaferrites.

In this work some good results were achieved, which led to some answers and many new questions. In general the magnetoelectric/multiferroic composites are a complex of study, and much more research will be needed to comprehend the connectivity between them and how to achieve better results.

Bibliography

1. Karpinsky, D., et al., Development of Novel Multiferroic Composites Based on $BaTiO_3$ and Hexagonal Ferrites. Proceedings of the Materials Research Society, 2009. 1161: p. 7-12.
2. Karpinsky, D., et al., Local probing of magnetoelectric coupling in multiferroic composites of $BaFe_{12}O_{19}$–$BaTiO_3$. Journal of Applied Physics, 2010. 108(4): p. 042012-042012-5.
3. Pullar, R.C. and A.K. Bhattacharya, The synthesis and characterization of the hexagonal Z ferrite, $Sr_3Co_2Fe_{24}O_{41}$, from a sol-gel precursor. Materials Research Bulletin, 2001. 36(7–8): p. 1531-1538.
4. Röntgen, W.C., Ueber die durch Bewegung eines im homogenen electrischen Felde befindlichen Dielectricums hervorgerufene electrodynamische Kraft. Annalen der Physik, 1888. 271(10): p. 264-270.
5. Curie, P., Symétrie d'un champ électrique d'un champ magnétique. J. PPhys 1894. 3: p. 393-415.
6. Debye, P., Bemerkung zu einigen neuen Versuchen über einen magneto-elektrischen Richteffekt. Zeitschrift für Physik A Hadrons and Nuclei, 1926. 36(4): p. 300-301.
7. Perrier, A. and A.J. Staring, Arch. Sci. Phys., 1922. Nat 4: p. 373-382.
8. Kamenetskii, E.O., M. Sigalov, and R. Shavit, Tellegen particles and magnetoelectric metamaterials. Journal of Applied Physics, 2009. 105(1): p. 013537-15.
9. Folen, V.J., G.T. Rado, and E.W. Stalder, Anisotropy of the Magnetoelectric Effect in Cr2O3. Physical Review Letters, 1961. 6(11): p. 607-608.
10. Dzyaloshinskii, I.E., ON THE MAGNETO-ELECTRICAL EFFECT IN ANTIFERROMAGNETS. Soviet Physics Jetp-Ussr, 1960. 10(3): p. 628-629.
11. Astrov, D.N., THE MAGNETOELECTRIC EFFECT IN ANTIFERROMAGNETICS. Soviet Physics Jetp-Ussr, 1960. 11(3): p. 708-709.
12. Smolenskii, G.A. and I.E. Chupis, Segnetomagnetics. Uspekhi Fizicheskikh Nauk, 1982. 137(3): p. 415-448.
13. Venevtsev, Y.N. and V.V. Gagulin, Search, design and investigation of seignettomagnetic oxides. Ferroelectrics, 1994. 162(1): p. 23-31.
14. Schmid, H., Multi-ferroic magnetoelectrics. Ferroelectrics, 1994. 162(1): p. 317-338.
15. Suchetelene, J.v., Product properties: a new application of composite materials,, 1972: Eindhoven. p. 28-37.
16. Boomgaard, J. and R.A.J. Born, A sintered magnetoelectric composite material BaTiO3-Ni(Co, Mn) Fe_2O_4. Journal of Materials Science, 1978. 13(7): p. 1538-1548.
17. Nan, C.-W., et al., Multiferroic magnetoelectric composites: Historical perspective, status, and future directions. Journal of Applied Physics, 2008. 103(3): p. 031101.
18. Qin, Q.H., Green's function and boundary elements of multifield materials 2007: Elsevier Science Limited. 266.
19. Newnham, R.E., D.P. Skinner, and L.E. Cross, Connectivity and piezoelectric-pyroelectric composites. Materials Research Bulletin, 1978. 13(5): p. 525-536.
20. Nalwa, H.S., Ferroelectric Polymers: Chemistry, Physics, and Applications, ed. 4th 1995: Marcel Dekker. 912.
21. Mayergoyz, I.D. and G. Engdahl, Handbook of giant magnetostrictive materials 1999: Academic press. 386.
22. Dong, S., J.-F. Li, and D. Viehland, Ultrahigh magnetic field sensitivity in laminates of TERFENOL-D and $Pb(Mg_{1/3}Nb_{2/3})O_3$-$PbTiO_3$ crystals. Applied Physics Letters, 2003. 83(11): p. 2265-2267.

23. Dong, S., J.-F. Li, and D. Viehland, Characterization of magnetoelectric laminate composites operated in longitudinal-transverse and transverse--transverse modes. Journal of Applied Physics, 2004. 95(5): p. 2625-2630.
24. Dong, S., J.F. Li, and D. Viehland, Voltage gain effect in a ring-type magnetoelectric laminate. Applied Physics Letters, 2004. 84(21): p. 4188-4190.
25. Zheng, H., et al., Three-dimensional heteroepitaxy in self-assembled $BaTiO_3$-$CoFe_2O_4$ nanostructures. Applied Physics Letters, 2004. 85(11): p. 2035-2037.
26. Aguesse, F., et al., Enhanced magnetic performance of $CoFe_2O_4$/$BaTiO_3$ multilayer nanostructures with a SrTiO3 ultra-thin barrier layer. Scripta Materialia, 2012. 67(3): p. 249-252.
27. Jian, G., et al., Microstructure and multiferroic properties of $BaTiO_3$/$CoFe_2O_4$ films on Al_2O_3/Pt substrates fabricated by electrophoretic deposition. Journal of the European Ceramic Society, 2013. 33(6): p. 1155-1163.
28. Gupta, A. and R. Chatterjee, Dielectric and magnetoelectric properties of $BaTiO_3$–$Co_{0.6}Zn_{0.4}Fe_{1.7}Mn_{0.3}O_4$ composite. Journal of the European Ceramic Society, 2013. 33(5): p. 1017-1022.
29. Hill, N.A., Why Are There so Few Magnetic Ferroelectrics? The Journal of Physical Chemistry B, 2000. 104(29): p. 6694-6709.
30. Pullar, R.C., Hexagonal ferrites: A review of the synthesis, properties and applications of hexaferrite ceramics. Progress in Materials Science, 2012. 57(7): p. 1191-1334.
31. Eerenstein, W., N.D. Mathur, and J.F. Scott, Multiferroic and magnetoelectric materials. Nature, 2006. 442(7104): p. 759-65.
32. Pullar, R.C., I.K. Bdikin, and A.K. Bhattacharya, Magnetic properties of randomly oriented BaM, SrM, Co_2Y, Co_2Z and Co_2W hexagonal ferrite fibres. Journal of the European Ceramic Society, 2012. 32(4): p. 905-913.
33. Nan, C.-W., Magnetoelectric effect in composites of piezoelectric and piezomagnetic phases. Physical Review B, 1994. 50(9): p. 6082-6088.
34. Ryu, J., et al., Magnetoelectric Properties in Piezoelectric and Magnetostrictive Laminate Composites. Japanese Journal of Applied Physics. 40(Copyright (C) 2001 The Japan Society of Applied Physics): p. 4948.
35. Boomgaard, J., et al., A sintered magnetoelectric composite material BaTiO3-Ni(Co, Mn)Fe2O4. Journal of Materials Science. 13(7): p. 1538-1548.
36. Boomgaard, J., et al., An in situ grown eutectic magnetoelectric composite material. Journal of Materials Science. 9(10): p. 1705-1709.
37. Newnham, R.E., Properties of Materials: Anisotropy, Symmetry, Structure 2005: Oxford University Press, USA.
38. van der Zaag, P.J., Ferrites, in Encyclopedia of Materials: Science and Technology (Second Edition), K.H.J.B. Editors-in-Chief: , et al., Editors. 2001, Elsevier: Oxford. p. 3033-3037.
39. Foster, L.S., Ferrites (Smit, J.; Wijn, H. P. J.). Journal of Chemical Education, 1960. 37(7): p. 380.
40. Pardavi-Horvath, M., Microwave applications of soft ferrites. Journal of Magnetism and Magnetic Materials 2000. 215: p. 171-183.
41. Panchal, N.R., Study and characterization of some Hexa-Ferrite systems, in Department of Physics 2012, Gujarat University: Indian ETD Repository. p. 154.
42. Goldman, A., Modern Ferrite Technology. Vol. 2. 2006, Boston, MA: Springer US: Boston, MA. 438.
43. Intrater, J., A review of: "Ferromagnetic Materials – Structure and Properties" by R. A. McCurrie. Materials and Manufacturing Processes, 1995. 10(6): p. 1300-1301.
44. Costa, A.C.F.M., et al., Synthesis, microstructure and magnetic properties of Ni–Zn ferrites. Journal of Magnetism and Magnetic Materials, 2003. 256(1–3): p. 174-182.

45. Qiu, J., M. Gu, and H. Shen, Microwave absorption properties of Al- and Cr-substituted M-type barium hexaferrite. Journal of Magnetism and Magnetic Materials, 2005. 295(3): p. 263-268.
46. Gerber, R., Z. Šimša, and L. Jenšovský, A note on the magnetoplumbite crystal structure. Czechoslovak Journal of Physics, 1994. 44(10): p. 937-940.
47. V. Adelskold and A. Kemi, Min Geol., 1938. 12(A): p. 1.
48. Went, J.J., et al., Hexagonal Iron-Oxide Compounds as Permanent-Magnet Materials. Physical Review, 1952. 86(3): p. 424-425.
49. Özgür, Ü., Y. Alivov, and H. Morkoç, Microwave ferrites, part 1: fundamental properties. Journal of Materials Science: Materials in Electronics, 2009. 20(9): p. 789-834.
50. Braun, P.B., Crystal Structure of $BaFe_{18}O_{27}$. Nature, 1952. 170(4330): p. 708-708.
51. Wijn, H.P.J., A New Method of Melting Ferromagnetic Semiconductors. $BaFe_{18}O_{27}$, a New Kind of Ferromagnetic Crystal with High Crystal Anisotropy. Nature, 1952. 170(4330): p. 707-708.
52. McCurrie, R.A., Ferromagnetic materials: structure and properties 1994, Universidade de Michigan: Academic. 297.
53. van Arkel, A.E., E.J.W. Verwey, and M.G. van Bruggen, Ferrites I. Recueil des Travaux Chimiques des Pays-Bas, 1936. 55(4): p. 331-339.
54. Smit. J and Wijn. H.P.J, Ferrites 1959 Eindhoven: Philips Technical Library. 387.
55. International Centre for Diffraction Data, USA PDF No. 84-1531 ($SrFe_{12}O_{19}$), 84-757 ($BaFe_{12}O_{19}$), 84-2046 ($PbFe_{12}O_{19}$), Newton Square, PA.
56. Matsumoto, M., A. Morisako, and S. Takei, Characteristics of Ba–ferrite thin films for magnetic disk media application. Journal of Alloys and Compounds, 2001. 326(1–2): p. 215-220.
57. Von Aulock, W.H. and A.S. Boxer, Handbook of Microwave Ferrite Materials 1965: Academic Press. 518.
58. Fang, C.M., et al., Magnetic and electronic properties of strontium hexaferrite $SrFe_{12}O_{19}$ from first-principles calculations. Journal of Physics: Condensed Matter, 2003. 15(36): p. 6229.
59. Singhal, S., et al., A comparative study on the magnetic properties of $MFe_{12}O_{19}$ and $MAlFe_{11}O_{19}$ (M = Sr, Ba and Pb) hexaferrites with different morphologies. Ceramics International, 2011. 37(6): p. 1833-1837.
60. Wohlfarth, E.P. and K.H.J. Buschow, Ferromagnetic materials: a handbook on the properties of magnetically ordered substances 1982: North-Holland Pub. Co.
61. Robert, P., Electrical and magnetic properties of materials 1988: Artech House. 458.
62. Spaldin, N.A., Magnetic Materials: Fundamentals and Applications 2010: Cambridge University Press.
63. Pillai, S.O., Solid State Physics. Vol. 6. 2005: New Age International. 819.
64. Cullity, B.D. and C.D. Graham, Introduction to Magnetic Materials. Vol. 2. 2011: John Wiley & Sons, 2011. 568.
65. Tsymbal, E., Physics-927: Introduction to Solid State Physics, 2007, University of Nebraska Lincoln.
66. Askeland, D.R., P.P. Fulay, and W.J. Wright, The Science and Engineering of Materials. Vol. 6. 2010: Cengage Learning. 921.
67. Spaldin, N.A., Magnetic Materials: Fundamentals and Device Applications2003: Cambridge University Press.
68. Spaldin, N.A. Magnetic materials fundamentals and applications. 2011.
69. Martins, J.d.s., Caracterização magnética de filmes de ZnO dopados com Fe, in Departamento de Física 2008, Universidade de Aveiro: Sinbad. p. 58.

70. Nave, C.R. Hyperphysics. 2012 [cited 2012 06-11]; Available from: http://hyperphysics.phy-astr.gsu.edu/hbase/hph.html.
71. Bhattarai, K. and T.U.o.W.-. Milwaukee, Fiber Optics Based Fault Detection in Power Systems. ProQuest ed2008: The University of Wisconsin - Milwaukee. 91.
72. Savage, H.T. and M.L. Spano, Theory and application of highly magnetoelastic Metglas 2605SC (invited). Journal of Applied Physics, 1982. 53(11): p. 8092-8097.
73. Shu, Y.C., M.P. Lin, and K.C. Wu, Micromagnetic modeling of magnetostrictive materials under intrinsic stress. Mechanics of Materials, 2004. 36(10): p. 975-997.
74. Center, N.E.R. The Hysteresis Loop and Magnetic Properties. 2001 [cited 2012 11 of November]; Available from: http://www.ndt-ed.org/ EducationResources /CommunityCollege /MagParticle/ Physics/HysteresisLoop.htm.
75. Valenzuela, R., Magnetic Ceramics. Vol. 4. 2005: Cambridge University Press. 336.
76. Johnson, M.T., et al., Magnetic anisotropy in metallic multilayers. Reports on Progress in Physics, 1996. 59(11): p. 1409.
77. Moskowitz, B.M. HITCHHIKER'S GUIDE TO MAGNETISM. 1991 [cited 2012 06-11-2012]; Available from: http://www.irm.umn.edu/hg2m/hg2m_index.html.
78. Puli, V.S., PTCR effect in La_2O_3 doped $BaTiO_3$ ceramic sensors, in Physics 2006, Auckland University of Technology: New Zealand p. 108.
79. Lozano-Gorrín, A.D., Structural Characterization of New Perovskites, Polycrystalline Materials - Theoretical and Practical Aspects. InTech2012. 164.
80. Vijatovic, M.M., J.D. Bobic, and B.D. Stojanovic, History and challenges of barium titanate: Part I. Science of Sintering, 2008. 40(2): p. 155-165.
81. Tadayuki Imai, M.S., Koichiro Nakamura, Kazuo Fujiura, Crystal Growth and Electro-optic Properties of KTa1−xNbxO3. NTT Technical Review, 2007. 5(9): p. 8.
82. Liliam Viana, L., Síntese e caracterização de compósitos titanato de bário-ferrita de cobalto preparados a partir de método sol-gel, 2010, Universidade Federal de Minas Gerais.
83. Aygun, S.M., Processing Science of Barium Titanate2009, North Carolina North Carolina State University. 216.
84. Birol, H., D. Damjanovic, and N. Setter, Preparation and characterization of (K0.5Na0.5)NbO3 ceramics. Journal of the European Ceramic Society, 2006. 26(6): p. 861-866.
85. Priya, S., Lead-Free Piezoelectrics 2012: Springer.
86. BANSAL, V., Synthesis and Characterization of Sodium Potassium Niobate ($Na_{0.5}K_{0.5}NbO_3$)–Nickel-Zinc Ferrite ($Ni_{0.6}Zn_{0.4}Fe_2O_4$)Composite, in Department of Ceramic Engineering2010, National Institute of technology Rourkela: Rourkela. p. 37.
87. Lin, D., K.W. Kwok, and H.W.L. Chan, Dielectric and piezoelectric properties of ($K_{0.5}Na_{0.5}NbO_3$–$Ba(Zr_{0.05}Ti_{0.95})O_3$ lead-free ceramics. Applied Physics Letters, 2007. 91(14): p. 143513.
88. Li, H., Sodium potassium niobate-based lead-free piezoelectric ceramics: bulk and freestanding thick films, 2008, Drexel University.
89. Yao, N. and Z.L. Wang, Handbook of microscopy for nanotechnology 2005: Kluwer Academic Pub.
90. Suryanarayana, C. and G. Norton, X-Ray Diffraction: A Practical Approach 1998: Plenum Press.
91. Jenkins, R. and R. Snyder, Introduction to X-Ray Powder Diffractometry 2012: Wiley.
92. Lifshin, E., X-ray Characterization of Materials 2008: Wiley.
93. Krumeich, F. Bragg's Law of Diffraction. 2012 8 November [cited 2013 3 of March].
94. Kalinin, S.V. and A. Gruverman, Scanning Probe Microscopy of Functional Materials 2010: Springer New York.

95. Research, A. Piezoresponse Force Microscopy with Asylum Research AFMs. 2013 [cited 2013 9 of March]; Available from: http://www.asylumresearch.com/ Applications/ PFMAppNote/ PFMAppNote.shtml.
96. Safari, A. and E.K. Akdoğan, Piezoelectric and Acoustic Materials for Transducer Applications2008: Springer London, Limited.
97. Waser, R. Probing the nanoworld - scanning probe techniques and more. 2012 [cited 2013 06 of March].
98. Stanford Research Systems, I. About Lock-In Amplifiers. 2013 [cited 2013 9 of March]; Available from:http://www.thinksrs.com/downloads/PDFs/ApplicationNotes/AboutLIAs.pdf.
99. AG, J.I., Piezoresponse force microscopy, 2013. p. 4.
100. Corp, P.S. Advanced SPM Modes - Piezoelectric Force Microscopy (PFM). 2008 [cited 2013 9 of March]; Available from: http://www.parkafm.com/AFM_guide/ spm_modes_3.php?id= 1188& Piezoelectric 20Force%20Microscopy%20(PFM).
101. System, P. Advanced SPM Modes - Magnetic Properties. 2013 [cited 2013 16-03-2013]; Available from: http://www.parkafm.com/AFM_guide/spm_modes_7.php?id=1211& Mag -netic Force Microscopy (MFM)#.
102. Instruments, D. Magnetic Force Microscopy (MFM) Support Note No. 229, Rev. B. 1996 [cited 2013 17 of March]; Available from: http://www.ccmr.cornell.edu/facilities/ downloads/229B-Mag Force Microscopy.pdf.
103. Schonenberger, C., et al., Separation of magnetic and topographic effects in force microscopy. Journal of Applied Physics, 1990. 67(12): p. 7278-7280.
104. Lindemuth, J., J. Krause, and B. Dodrill, Finite sample size effects on the calibration of vibrating sample magnetometer. Magnetics, IEEE Transactions on, 2001. 37(4): p. 2752-2754.
105. Interlaboratory Comparison of Magnetic Thin Film Measurements: DIANE Publishing.
106. Nalwa, H.S., Handbook of Thin Films, Five-Volume Set 2001: Academic Press.
107. Mahalakshmi, S., Structure, electrical and magnetic properties of rare earth doped nanophase ferrites, in School of physical, chemical and applied sciences 2010, Pondicherry University: Indian ETD Repository. p. 172.
108. Vibrating sample magnetometer. 22 of March [cited 2013 22 of March]; Available from: http://en.wikipedia.org/wiki/Vibrating_sample_magnetometer.
109. Sakka, S., Handbook of sol-gel science and technology. 2. Characterization and properties of sol-gel materials and products2005: Kluwer Academic Publishers.
110. Kikuchi, T., et al., Synthesis of single-phase $Sr_3Co_2Fe_{24}O_{41}$ Z-type ferrite by polymerizable complex method. Materials Research Bulletin, 2011. 46(7): p. 1085-1087.
111. Selezneva, E., Magnetoelectric composites based on hexagonal ferrites, in Departamento de Engenharia Cerâmica e do Vidro2008, Universidade de Aveiro. p. 79.

Appendix

Uniaxial pressure and maximum theoretical density BT (%)					
	BaZ	SrZ	BaM	SrM	
BT - 10	68	55	64	59	RES
BT - 20	67	58	65	64	
BT - 30	68	61	64	64	
BT - 10	66	67	68	73	Sol gel
BT - 20	62	64	72	68	
BT - 30	63	62	73	72	
BT - 10	66	55	75	77	COP
BT - 20	63	58	74	77	
BT - 30	63	59	75	75	
BT - 10	64	63	72	67	Citrates
BT - 20	65	67	72	69	
BT - 30	68	72	71	68	

Cold isotactic pressure and maximum theoretical density BT (%)					
	BaZ	SrZ	BaM	SrM	
BT - 10	64	76	72	77	RES
BT - 20	63	71	72	68	
BT - 30	68	77	71	70	
BT - 10	64	67	66	73	Sol gel
BT - 20	67	67	74	75	
BT - 30	68	68	73	74	
BT - 10	66	63	77	80	COP
BT - 20	67	64	78	81	
BT - 30	66	62	77	79	
BT - 10	68	63	77	73	Citrates
BT - 20	69	69	78	75	
BT - 30	70	72	77	74	

Appendix B

Summary of the basic functions of the measurement systems utilized

Technique	Main information	depth probed	min. area probed	Accuracy resolution	Operational range	Operational requirements	Typical sample requirements
SEM	surface imaging	< 1 μm	5 nm^2	> 1 mm	Room Temperature	High Vacuum	Conductive surface or coating
XRD	Structure phases	∼ 1 μm	> mm^2	> mm^2	77-600K or room temperature	Vacuum, room atmosphere	> 20 mm^2
PFM	Dielectric phase mapping	< 1 μm	10 nm^2	< 20nm	Room Temperature	Mechanical stability	smooth surfaces
MFM	Magnetic phase mapping	< 1 μm	10 nm^2	< 20nm	Room Temperature	Mechanical stability	smooth surfaces
VSM	Magnetic moment	> cm	> mm^2	0,001 T > 10^{-5} emu	4-310K	Vacuum, He	< 1cm long > 0,05g